

5.7.2 Time-of-flight reconstructions of real treatment simulations

During heavy ion treatments, a considerable amount of activity is transported to locations outside the FOV of the in-beam positron tomograph. In these situations, the use of TOF information may decrease the number of background events registered. But the most important advantages of an eventual in-beam TOF-PET arise if the time difference between the arrival of the photons is used to directly compute, on an event-by-event basis, the location where the positron annihilation occurred. Not only the computing time is immensely reduced, as shown in Table 5.8, but also the limitations arising from limited-angle tomography vanish if the coincidence time resolution is better than 200 ps FWHM, as shown in Figs. 5.23 and 5.24, obtained with a simulated dual head tomograph with wide gaps ($\phi = 100^\circ$, cf. Fig. 2.1). The

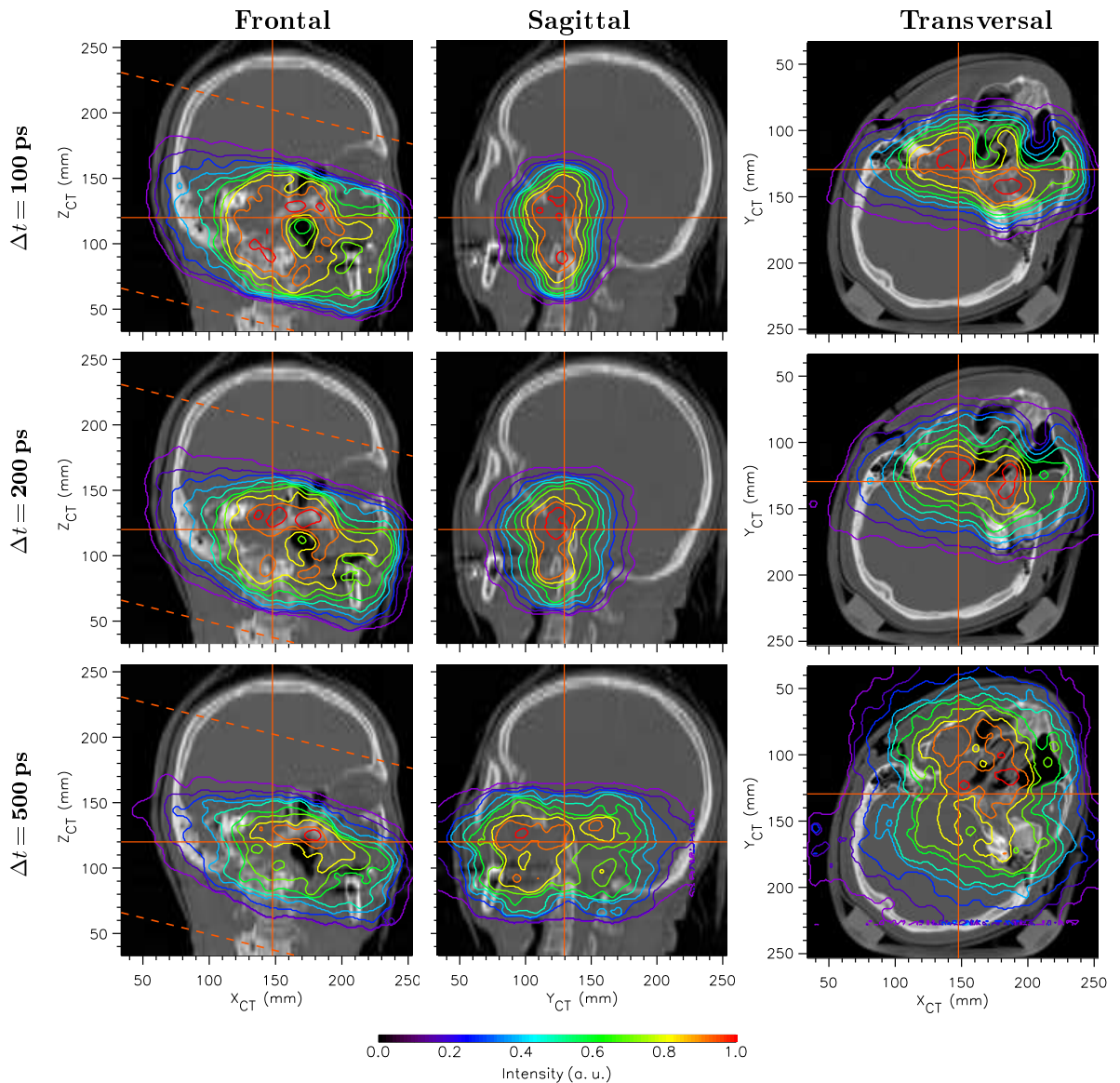


Figure 5.23: Head and neck irradiation: direct TOF reconstruction for different coincidence time resolutions Δt given in ps FWHM. All images correspond to a dual head tomograph with wide gaps ($\phi = 100^\circ$, cf. Fig. 2.1). The dashed lines in the frontal views show the limits (top view) of the dual-head tomograph considered.

minimum coincidence time resolution mentioned, 200 ps FWHM, although not far from being achieved [Var05, Ver05, Mos04], is still a technological challenge for commercial PET systems.

The analysis of Figs. 5.23 and 5.24 allows a minimum, useful coincidence time resolution to be estimated at 200 ps FWHM, as mentioned. This corresponds to a spatial resolution of 3 cm FWHM in the Y_{PET} axis, along which the gap with missing detectors lies (cf. Fig. 2.1). This spatial resolution is enough, as observed in the middle row in Figs. 5.23 and 5.24, to refrain the image elongation observed in Figs. 2.10 and 2.13, respectively, yielding therefore in-beam PET images that can be directly compared with the β^+ -activity distribution produced in the target volume (Figs. 2.9 and 2.12 for head-and-neck and pelvis irradiation, respectively).

The most impressive results expected if TOF-PET detectors with very high coincidence time resolution, below 200 ps FWHM, would be commercially available, are the speed with which the image becomes available to the radiotherapist after the irradiation of each portal: below 2 minutes as demonstrated in Table 5.8. This increase in image processing speed arises from the possibility to calculate at once the point of positron annihilation as soon as the coordinates of the hit detectors and the TOF information are known. Such algorithm needs to process one single iteration through the collected data only, in opposition to the 50 iterations necessary with the MLEM algorithm which, in addition, needs to cross the full image space for every pair of detectors that was triggered. Due to this last detail the processing speed of the direct

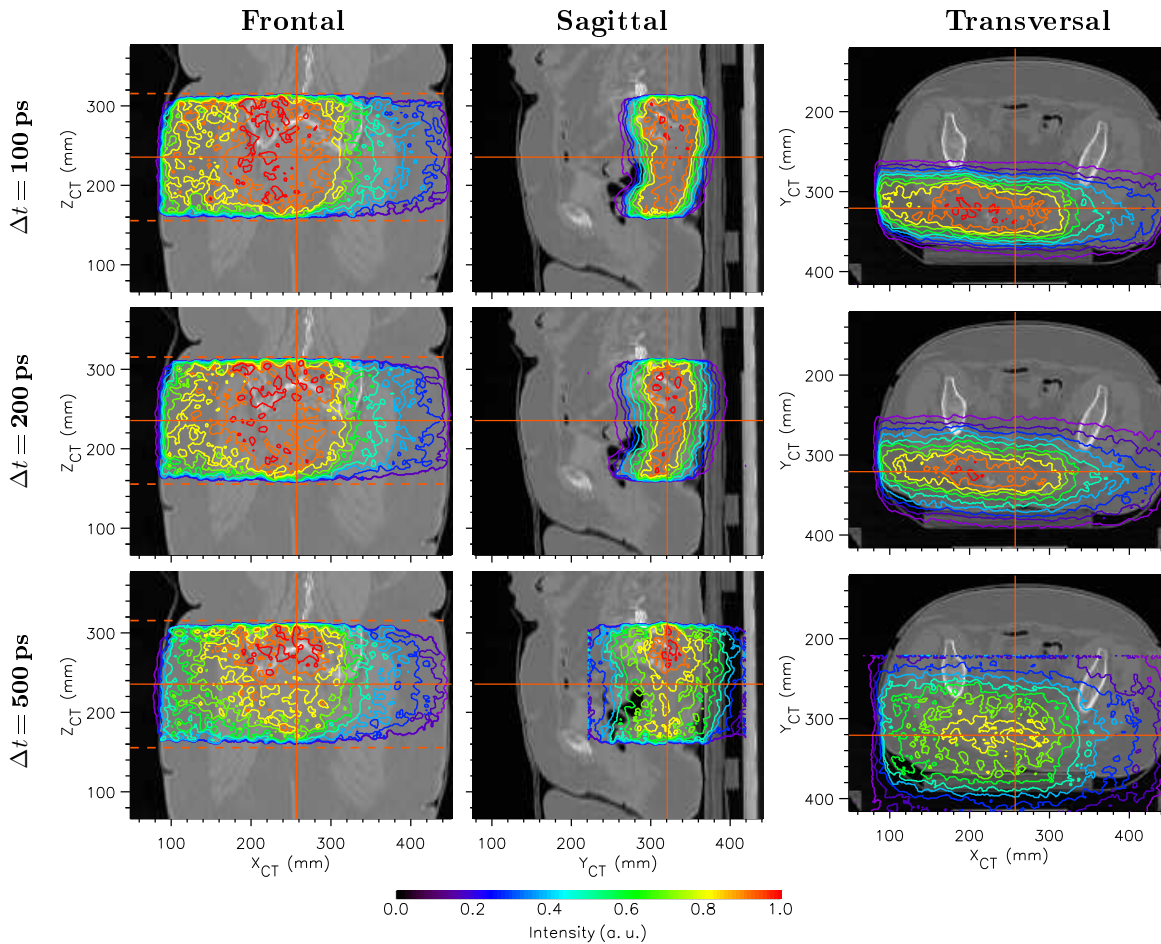


Figure 5.24: Pelvis irradiation: direct TOF reconstruction with different coincidence time resolutions Δt given in ps FWHM. All images correspond to a dual head tomograph with wide gaps ($\phi = 100^\circ$, cf. Fig. 2.1). The dashed lines in the frontal views show the limits (top view) of the dual-head tomograph considered.

Table 5.8: Comparison of times required for image availability: direct-TOF versus MLEM-based PET imaging. Computations executed on an Intel(R) Xeon(TM) CPU 3.20 GHz dual-processor. All reconstructions regard a dual head tomograph with wide gaps ($\phi = 100^\circ$, Fig. 2.1).

Treatment	Image size (cm ³)	Number of events	Run time	
			TOF ^a	MLEM (50 iterations)
Head and neck	22 × 20 × 20	1.3 × 10 ⁶	45 s	5 h 40 m
Pelvis	40 × 25 × 25	5.3 × 10 ⁶	103 s	> 5 days

^a The image is ready after a single iteration through the data

TOF algorithm is expected to stay below that of fast, expectation maximization algorithms like OSEM.

Since the time to obtain an image is smaller than the typical irradiation time, TOF-PET would allow the image to be processed and shown to the oncologist during the course of the irradiation, i.e. in-beam PET could be called for the first time *on-line*, in-beam PET. Moreover, a coincidence time resolution of 50 ps FWHM, i.e. 7.5 mm FWHM, would allow an image of each single pencil-like beam being delivered with the rasterscan technique [Hab93] to be obtained at once.

5.8 Summary and Outlook

The performance and in-beam imaging capabilities of two position sensitive γ -ray detectors consisting of Hamamatsu avalanche photodiode arrays (S8550) individually coupled to crystals of cerium-doped lutetium oxyorthosilicate (LSO) were presented. In a first set of experiments the imaging performance of the detectors was tested before, during and after the irradiation of phantoms of polymethylmethacrylate with carbon ion beams with fluences equivalent to 1000 typical daily therapeutic fractions. Only minor energy, time and spatial resolution deterioration was observed, with the initial values being recovered after stopping the irradiation. The line source, placed in the FOV of the detectors, was imaged as the detectors were positioned in the backward or forward cone of phantoms bombarded with the high energy ¹²C ion beam with the mentioned characteristics. The line source images obtained revealed that it is possible, from the point of view of detector hardness, implementing a dual-head, in-beam positron camera with these detectors forming two small gaps for (1) the entrance of the therapeutic beam and (2) the escape of the light nuclear fragments produced in the patient. Thus, a double-head positron camera of large solid angle covered becomes feasible, allowing limited angle artifacts in in-beam PET images to be minimized (chapter 2). However, it must be noted that, from the point of view of in-beam PET imaging with low statistics, a more realistic experiment with decreased activity within the FOV of the detectors could also provide useful information since the activity of the line source was orders of magnitude higher than that of typical in-beam PET measurements.

In the second set of experiments, an image of the β^+ -activity depth distribution created in a phantom stopping the high energy carbon ion beam was successfully performed. This was an important achievement since it demonstrated (1) the in-beam imaging capability of this detector type and (2) the sufficient radiation hardness of such detectors to be operated at a radiotherapy treatment site.

In another experiment the activation of the scintillator material LSO under therapeutical irradiation was investigated. An LSO crystal matrix was submitted to the flux of light particles leaving two, single-portal patients treated with carbon ions. The absence of either new γ -ray

lines or an enhancement of existing lines in the high-resolution spectroscopic measurements performed before and after irradiating the LSO crystal matrix reveals that scintillator activation does not take place in realistic therapeutic conditions.

Due to the small amount of ^{176}Lu , a natural radioactive isotope, in LSO, the influence of the natural background activity of LSO onto the random and true coincidences expected for an LSO-based tomograph was addressed. It was seen that the random coincidences count rates arising from this background can compromise the use of LSO for in-beam PET scanners due to the low-intensity in-beam PET signal. Conventional random suppression techniques applied in nuclear medicine PET imaging fail for in-beam PET measurements during particle extraction, which is a mandatory requisite for next-generation in-beam positron tomographs due to the optimized usage of ion accelerators (chapter 6). This means that, in order not to compromise the quality of the low-statistics in-beam PET images, a modern readout with digital signal processing, providing a coincidence time resolution of 500 ps, is mandatory.

Finally, the impact of recent developments in ultra-fast timing detectors, potentially allowing the implementation of the time-of-flight technique onto commercial PET scanners, was extrapolated to in-beam PET. It was seen that TOF techniques gain much importance for dual-head, in-beam PET scanners due to the capability of the TOF information to reduce the image elongation that characterizes limited-angle tomography. Equally important, both for closed-ring as well as for dual-head, in-beam positron tomographs, is the immense decrease in data processing time if the TOF information is used, making in-beam PET images available even during the irradiation for tomographs with a coincidence time resolution below 200 ps FWHM.

In summary, the obtained results indicate that LSO, a fast, high light-yield scintillator material, is best suitable for in-beam PET when its time output is read with digital signal processing techniques achieving 500 ps coincidence time resolution. With this constraint satisfied, its combination with APDA forms a feasible concept for the compact, magnetic field resistant detectors required for in-beam PET applications. There may be an increased interest in such dedicated PET systems in the future since several clinical heavy ion facilities are planned [Hea98, Sie04] and, furthermore, the in-beam PET method has also the potential to monitor the precision of ion therapy with lighter species [Par04, Par05a, Fie05].

Chapter 6

Suppression of Random Coincidences during Particle Extraction

6.1 Motivation

The counting statistics of in-beam PET is generally low with consequences to the signal-to-noise ratio of the reconstructed images. The reasons for this are twofold. First, the counting statistics are limited by the dose applied to the patient, delivered mostly in 20 fractions¹ [Sch02b] with usually two beam portals. Typical activity densities induced at the tumor therapy irradiation reach about $200 \text{ Bq cm}^{-3} \text{ Gy}^{-1}$, with the dose per portal ranging between 0.3 and 1 Gy. This contrasts with activity density values of 10^4 to 10^5 Bq cm^{-3} in human PET tracer imaging and even 10^6 Bq cm^{-3} in animal PET studies. In addition, current limitations arise from the fact that in-beam PET data, measured at beams with a sub- μs time structure due to the accelerator radiofrequency (RF), are highly corrupted by random coincidences. These arise from prompt γ -rays following nuclear reactions of the projectiles with the atomic nuclei of the tissue. As outlined in section 6.2, they cannot be suppressed with random-correction techniques from conventional PET [Paw97, Par02b]. Therefore, in-beam PET images are reconstructed taking into account merely events registered in the pauses (~ 2 -4 s) between the beam macropulses (≤ 2 s, Fig. 1.19). For a given detector geometry, the only way for improving image quality is the efficient utilization of the annihilation photons available.

Furthermore, and more important than improving image quality, is the fact that recent accelerator developments implementing optimized beam extraction techniques result in a much reduced timing window for in-beam PET data taking if the presently installed acquisition technique is applied. The synchrotron proposed for the clinic in Heidelberg will use the RF knock-out² extraction method [Hir92] with variable extraction time between 1 and 10 s and multiple beam extraction at the same flat top [Dol00]. This yields great advantages [Eic03] both for respiration-gated treatments as well as for reducing the treatment duration using the rasterscan beam delivery technique [Hab93]. With injection and acceleration times of about 30 μs and 1 s, respectively, this results in a beam delivery duty factor³ D_f between 8 and 93 %,

¹ The less frequent treatment of locally advanced adenoid cystic carcinomas [Sch03d] or spinal chordomas [Sch03a] applies 6 fractions with carbon ion irradiation complemented with photon irradiation by means of intensity modulated radiation therapy (IMRT).

² In summary, the RF knock-out method consists in applying a transverse electric radio-frequency-field (RF) with a frequency synchronous to the betatron frequency of the particles in the ring [Dol00]. Due to this excitation the particles are moved from the inner, stable region of their trajectories to outer, unstable ones. After a few turns in the ring the particles are driven through electrostatic and magnetic septa into a trajectory leading them out of the ring (extraction).

³ Duty factor D_f of an accelerator is the ratio $D_f = \Delta t_M / T_M$, with Δt_M being the macropulse duration (beam extraction, ~ 2 s at the present GSI therapy unit) and T_M being the time of a synchrotron acceleration cycle, comprising beam injection, acceleration and extraction (presently 5 s at GSI).

i.e. extreme cases of accelerator optimization could yield only 7% of the (reduced) irradiation time available for in-beam PET data taking, making in-beam PET unfeasible if a method for random suppression during particle extraction [Eng05c] is not implemented.

One immediate consequence of the implementation of such a method, also mentionable as a motivation, is the applicability of in-beam PET to cyclotron-delivered therapeutic ion beams [Cre05d], not possible without random suppression during particle extraction because of the continuous particle delivery behaviour of cyclotrons (i.e. $D_f \sim 100\%$).

For these reasons, two methods for suppressing the micropulse-induced random coincidences have been proposed [Eng05c] and were tested at the GSI medical beam line [Cre05d] with results described below.

6.2 Methods for Random Correction

It has been shown that the noise introduced by random coincidences is an important limiting factor of count-rate performance for PET cameras operating in 3D mode [Bad96, Spi98]. The number of random coincidences may be reduced by altering the camera geometry to restrict the FOV for single events [Spi98] or by reducing the coincidence resolving time of the system. Once these factors have been minimized, the number of random coincidences on a particular line-of-response (LOR) can be corrected in conventional PET following either the delayed coincidence method or the singles count rates method. The delayed coincidence method is more common in the current generation of cameras. It assumes the measured prompt count rate C_m at a given LOR to be the sum of the true coincidence count rate C_t with the random count rate C_r , provided C_r is stationary in time. C_r is measured at a time significantly greater than the coincidence resolving time of the detectors and subtracted from C_m for each LOR. In the singles count rates method, singles rates from each individual detector element are collected and used to account for the random count rate of each LOR with the relation

$$C_r = 2 \Delta t C_i C_j, \quad (6.1)$$

where C_i and C_j are the singles count rates in detectors i and j forming LOR ij and $2 \Delta t$ is the time resolution of the system. The application of both methods to in-beam PET fails because during particle extraction C_r is not constant in time due to the existence of a microstructured beam delivery [Par02b].

6.2.1 The time microstructure of the beam

During beam extraction, a correlation between the moment of arrival of the carbon ions and a given phase of the RF-signal from the accelerator has been found [Par05b]. This correlation is depicted in Fig. 6.1 for a given beam energy and intensity (10^7 ions/s). During each RF period T_{RF} the ions arrive within a time window Δt_{bunch} . The width of Δt_{bunch} depends on the beam energy and, therefore, on T_{RF} , and is independent from the beam intensity up to the maximum therapy value of 2×10^8 ions/spill, which is orders of magnitude below the incoherent charge space limit of 10^{11} carbon ions/spill of the heavy ion synchrotron SIS¹ at GSI.

At the tumor therapy at GSI, the ^{12}C beam energy ranges from 88.83 to 430.10 AMeV, corresponding to T_{RF} from 480 down to 250 ns, respectively. The correlation between T_{RF} and the beam relativistic kinetic energy K is given by

$$T_{RF} = \frac{P_{SIS} \cdot f(E)}{n_{SIS} \cdot c} \cdot \frac{K + m_o c^2}{\sqrt{K^2 + 2K m_o c^2}}, \quad (6.2)$$

¹ Schwerionensynchrotron.

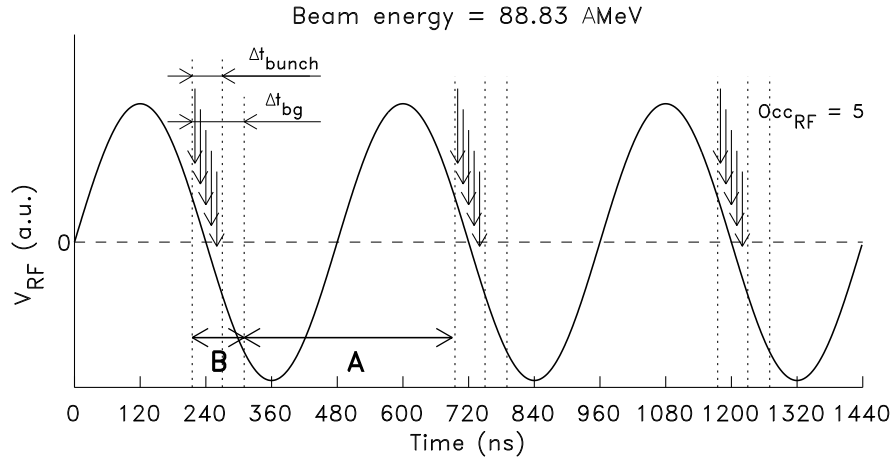


Figure 6.1: Correlation between the time of particle arrival, illustrated schematically with arrows, and RF-phase (arbitrarily set to π), depicted for a given beam energy and intensity (10^7 ions/s). The RF-occupancy occ_{RF} in the example displayed is 5, with $occ_{RF} = I \cdot T_{RF}$ and I the beam intensity. The letters A and B refer to the time windows outside the microbunch (A) and inside the microbunch with the corresponding high photon yield (B, bunch).

with values and units described in Table 6.1. The particle trajectory factor $f(K)$ arises from the different oscillations about the synchrotron perimeter that the particles undergo for a given energy, with $f(K)$ decreasing with increasing energy.

Table 6.1: Parameters correlating beam energy and RF-period.

Name	Symbol	Value
Perimeter of synchrotron	P_{SIS}	216 m
Particle trajectory factor	$f(E)$	1.091 to 1.008
Number of concomitant bunches	n_{SIS}	4
Speed of light in vacuum	c	2.998×10^8 m/s
Energy per nucleon	E	88.8 to 430.1 AMeV
Total kinetic energy	$K = 12 \cdot E$	1.1 to 5.2 GeV
Rest mass of ^{12}C	m_o	11 178 MeV/ c^2

The time window Δt_{bunch} comprises the time slot in which the ions arrive at each RF cycle. During this time, and shortly after it (Δt_{bg} in Fig. 6.1), a high flux of γ -rays arising from nuclear reactions is emitted [Par05b]. This sub- μs periodic flux constitutes the source of the high, in-beam random rate and any in-beam random suppression method must be able to discard it.

6.2.2 The methods for in-beam PET random correction

Two methods have been proposed which allow for identifying coincident events occurring within the time window Δt_{bg} [Eng05c] and are depicted in Fig. 6.2. From timing considerations only, and accounting for the accelerator duty factor presently implemented at GSI ($\sim 40\%$ during patient irradiation), an increase in image statistics of up to 65% is expected if coincidences acquired during the macropulse, but out of the micropulses, can be taken into account. The two methods rely on the synchronization of the $\gamma\gamma$ -coincidences measured by the positron camera with the time microstructure of the beam, either by using the RF-signal from the accelerator

or the signal of a thin, fast particle detector placed in the beam path immediately in front of the target.

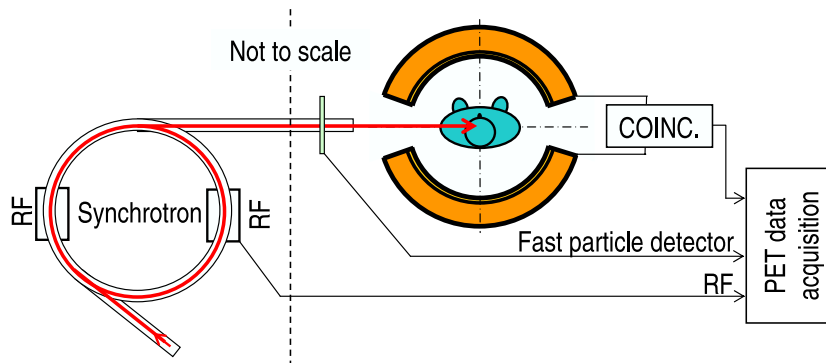


Figure 6.2: Implementation of the methods proposed for in-beam PET random suppression. Each detected $\gamma\gamma$ -coincidence is correlated with the incoming ion by using either a fast particle detector or the RF signal from the accelerator.

Using the RF-signal from the accelerator

If each $\gamma\gamma$ coincidence detected with the positron camera is correlated with the phase of the RF-signal, those events occurring within Δt_{bg} can either be labeled for posterior elimination or immediately discarded by the acquisition electronics (DAQ). In this first proof-of-principle approach, the readout of all events was performed with a multi-channel, zero-suppression free, list mode data acquisition (appendix B) that allowed off-line data processing. This was necessary in order to implement a proper timing selection around Δt_{bg} since coincidence measurements between $\gamma\gamma$ events and the RF-phase had not been performed before. Furthermore, the width of Δt_{bg} depends on the time resolution of the scintillation detectors used.

For the detection of a given RF-phase a fast peak detector NIM module (phase-trigger) was developed at FZR [Hei04]. A peak detector was chosen, instead of the leading edge circuit proposed in [Eng05c], because the RF signal delivered to the medical cave where the experiment was performed has about 30 % amplitude variation [For03] depending on the signal frequency. Although the present experiment was performed at a fixed beam energy, the phase trigger was seen to be a good first solution since the long cabling between the synchrotron and the medical cave introduced low frequency base-line oscillations of $\pm 10\%$ of the RF amplitude. A time measurement between RF-periods randomly separated revealed that the phase-trigger used is nearly insensitive to these oscillations with measured deviations being less than 1 % in all cases. Despite its phase detection ability independent of the pulse amplitude, this capacitor-based peak detector introduces frequency dependent delays resulting in a non-constant phase detection when used as a phase-trigger at consecutively changing beam energies, as is the case during therapeutic irradiation by means of the GSI rasterscan beam delivery [Hab93]. A phase-trigger independent of signal amplitude, frequency and base line oscillations, based on the leading edge circuit mentioned but preceded by a high-pass passive filter and built in zero-crossing mode is proposed in [Eng05c].

Using a fast particle detector

A second method of labeling coincidences arriving during the microbunches makes use of a thin, fast particle detector (FD) placed in the beam path in front of the target. In principle, and for RF-occupancies close to unity, this approach should allow the implementation of narrower

time windows around Δt_{bg} when compared to the RF-method, as depicted in Fig. 6.3. As it can be seen, the FD method does not trigger a gate unless a particle arrives, leading to higher readout available time in the case of low occ_{RF} .

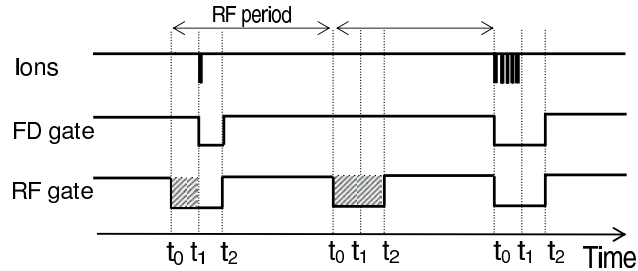


Figure 6.3: Different timing windows, automatically adjusting to the RF occupancy, are implementable with a fast particle detector FD, in contrast to the fixed-length, RF-generated windows.

For ion arrival detection a 300 μm thick, chemical vapor deposition (CVD) diamond detector [Fra04] was used. The detector was developed and optimized at the Forschungs- und Technologietransfer GmbH (FOTEC), Wiener-Neustadt, Austria. Fig. 6.4 shows its in-beam performance when 200.2 AMeV carbon ions trespass it at a beam intensity of 10^8 ions/s, corresponding to an occ_{RF} of about 32 ions/bunch. The analog signal in Fig. 6.4 shows that the CVD detector is capable of identifying single ions but, due to the 3 MHz low cutoff frequency [Fra04] introduced by the 1 nF capacity placed between the fast amplifiers reading the diamond detector (Fig. 6.5), the shaping electronics deliver a signal with undershoot and pulse pileup. Furthermore, saturation of the last amplifying stage also occurred due to the high current induced by the high ion flux in the middle of the microbunch. For these reasons, the measurements obtained with the CVD detector present noisier time spectra and spatial profiles, as described in section 6.6. Besides this fact, the results with the diamond detector are identical in all aspects to those obtained with the phase-trigger.

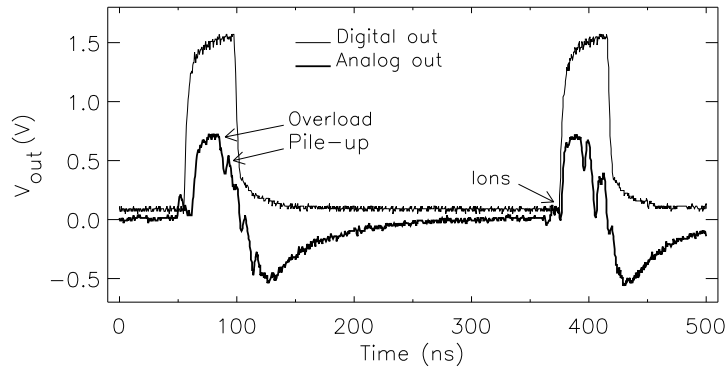


Figure 6.4: Analog and digital outputs of the diamond detector during two microbunches with an RF-occupancy of about 32. The analog signal is shown after three amplification stages with 3 MHz bandwidth each and total amplification gain of 60 dB.

6.3 Implementation and Electronics

The two methods described were simultaneously implemented with the system depicted in Fig. 6.5, partially identical to that described in section 5.2 except for two extra timing channels. Two position sensitive scintillation detectors, each consisting of 32 crystals of cerium-doped

lutetium oxyorthosilicate with $2.1 \times 2.1 \times 15 \text{ mm}^3$, coupled to the 4×8 pixels of an avalanche photodiode array [Kap04], were operated in coincidence. Limited angle in-beam tomographic imaging was performed following the method summarized in [Cre04] and described in more detail in section 5.4.1. This allowed to retrieve 2D images and linear profiles of the positron emitter depth distribution under several regimes, e.g. during the extraction pauses or during the beam extractions, inside and outside the microbunches.

For every detected $\gamma\gamma$ coincidence a readout of the energy signal in all imaging pixels (64) is performed, which allows for applying energy selection during off-line data evaluation. Further, the time differences between the detected $\gamma\gamma$ coincidence and the RF-phase (TAC3: $\gamma\gamma$ -RF) were recorded, as well as the particle crossing the diamond detector (TAC2: $\gamma\gamma$ -ion). The accelerator status was also recorded by sampling the extraction signal. Finally, all detected $\gamma\gamma$ coincidences signaled by the SCA output of TAC1 were fed into a scaler that counted all hits, even if the acquisition was busy processing a previous event. This allowed correcting the measured event rates with the corresponding DAQ dead time.

The timing diagram corresponding to the front-end and processing electronics during beam extraction is depicted in Fig. 6.6. Although the experiment was performed at $occ_{RF} = 32$, the

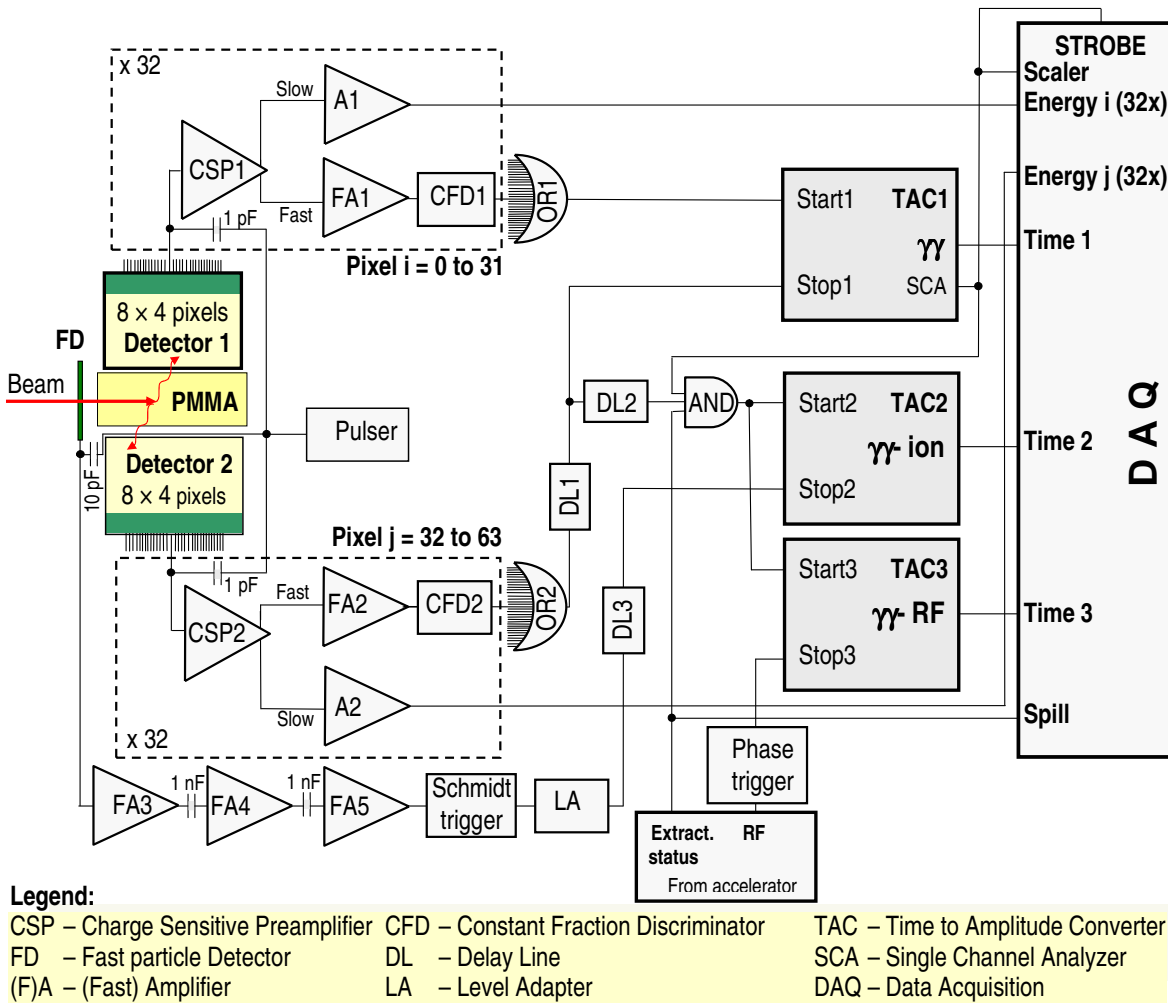


Figure 6.5: Scheme of the experimental setup, the event trigger, front-end and signal processing electronics implemented for the random suppression experiment.

figure displays $occ_{RF} = 4$ for simplicity. The output of the fast particle detector FD is depicted with the desired ultra-fast detector timing, i.e. without undershoot, pileup-free and able to perform single particle detection.

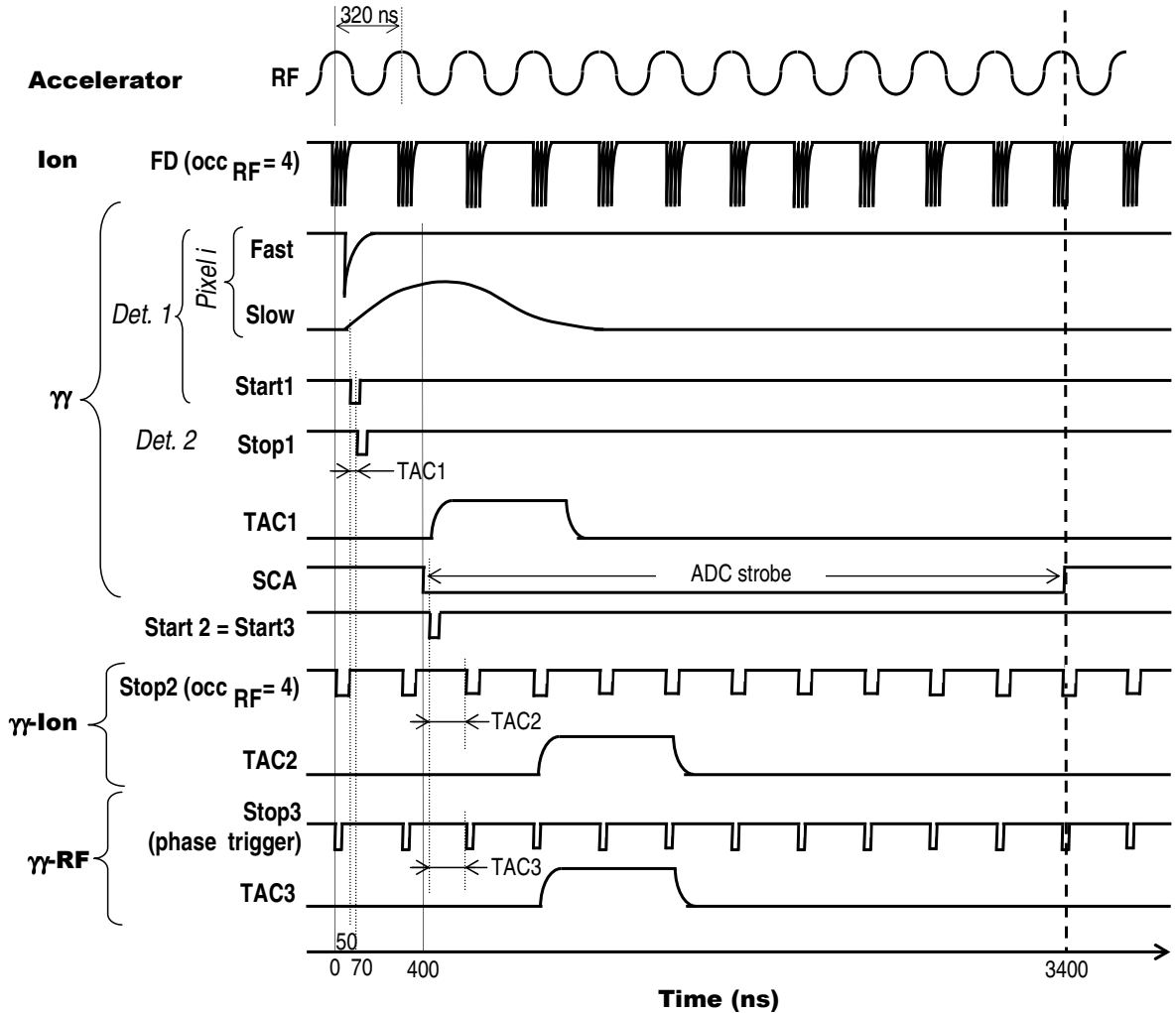


Figure 6.6: Timing diagram of the electronics in Fig. 6.5 during beam extraction depicted with $occ_{RF} = 4$ for simplicity.

6.4 Data Acquisition Dead-Time

In order to quantify the real event count rate hitting the detectors, together with the gain in image statistics, the dead time η of the DAQ must be known. For that, every event triggered increased a scaler that counted all hits, even if the DAQ was busy processing a given event. Fig. 6.7 shows the histograms of unread events obtained during the whole scan for all beam delivery regimes: extraction pauses and extractions. A detailed explanation of the plots and their meaning was presented in section 5.4.2. The extraction regime was further divided into the timing windows A and B of Fig. 6.1, i.e. outside and during the microbunches, respectively, as detailed in section 6.5.1. The ratio of total unread events during the extraction pauses and beam extractions, with the total number of events generated during the scan, yields a system total dead time η_{tot} of 57.4%. This value includes the dead times of two different measuring regimes that can be clearly separated (Fig. 1.19): the extraction pauses with low count rate

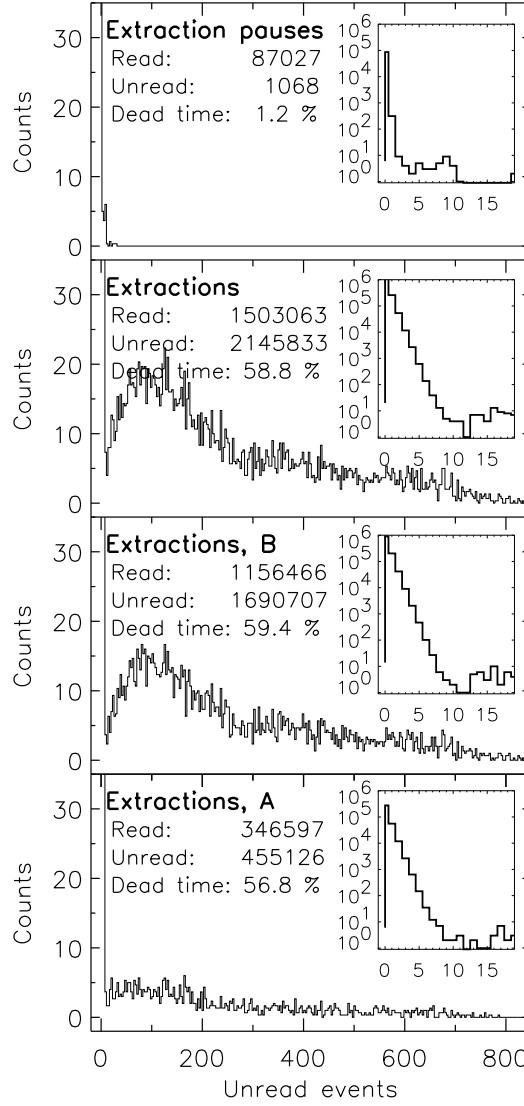


Figure 6.7: Histograms of unread events during all beam delivery regimes, with corresponding system dead times. The letters A and B refer to the time windows outside and inside the microbunches, respectively (Fig. 6.1).

and, consequently, low DAQ dead time, with $\eta_{pause} = 1.2\%$, and events acquired during beam extraction with higher DAQ dead time $\eta_{ext} = 58.8\%$. The relation between η_{tot} , η_{ext} and η_{pause} must follow

$$\frac{M_{tot}}{1 - \eta_{tot}} = \frac{M_{ext}}{1 - \eta_{ext}} + \frac{M_{pause}}{1 - \eta_{pause}}, \quad (6.3)$$

with M_{tot} , M_{ext} and M_{pause} the number of measured events in total, during beam extractions and pauses, respectively. These values are given in Fig. 6.7, namely $M_{tot} = 3\,736\,991$, $M_{ext} = 3\,648\,896$ and $M_{pause} = 88\,095$. The correlation between η_{ext} and η_{pause} is plotted with the solid curve in Fig. 6.8, obtained by fixing η_{tot} in Eq. 6.3. The diamond symbol shows the readout dead times achieved during particle extraction and in the pauses. The same relation given by Eq. 6.3 is valid during beam extraction with its two sub-regimes: timing windows A and B. This relation is plotted with the dashed curve in Fig. 6.8, with η_A and η_B related to the top and right axes, respectively, and $\eta_{ext} = 58.8\%$. As expected, the values obtained for

η_A and η_B are very similar to that of η_{ext} , i.e. a separation of the two sub-regimes could not be achieved. This happens because during beam extraction the signals and the readout of each event overlay several RF periods (Fig. 6.6) and count rate regimes. For this reason, even the low rate events taking place outside Δt_{bg} (A) present a high dead time close to 58.8%.

In summary, the dead times taken into account to correct image intensities in the next sections, $\eta_{pause} = 1.2\%$ and $\eta_{ext} = 58.8\%$, are understood and justified.

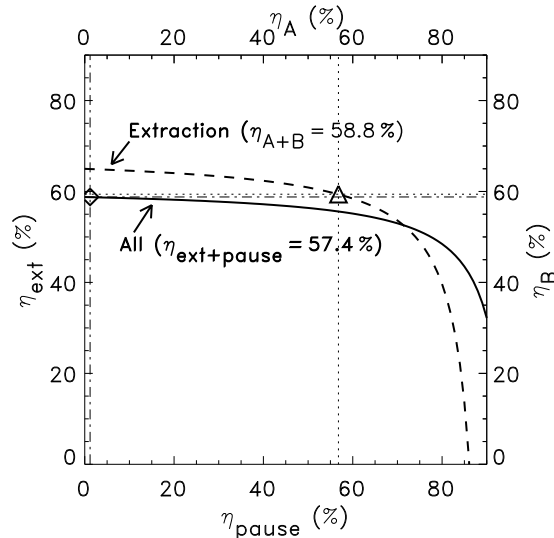


Figure 6.8: Relation between the dead times of several beam delivery regimes following Eq. 6.3. The bottom and left axes correspond to the solid curve, whereas the dashed curve is plotted against the right and top axes.

6.5 Results with the $\gamma\gamma$ -RF Method

For off-line data evaluation the routines developed to analyze the first in-beam imaging experiment with LSO/APDA detectors (chapter 5) were extended in order to handle two extra timing channels. An event selection based on the accelerator status signal and detailed in section 5.2 discriminated coincidences occurring within the beam extractions from those sampled during the extraction pauses. In addition, the present analysis further separated events acquired during beam extractions, as described in the next section.

6.5.1 Time and energy correlation between $\gamma\gamma$ and $\gamma\gamma$ -RF

A clear correlation between the $\gamma\gamma$ coincidences and the beam microstructure was observed and is shown in Fig. 6.9 for the RF measurements. This correlation can first be seen in column 1 where all events arriving within a time window of about 20 ns are plotted. The energy threshold was set by hardware individually for each pixel at about 300 keV. The $\gamma\gamma$ time spectrum is deteriorated by randoms in comparison to the same spectrum in the extraction pauses (column 4) and the $\gamma\gamma$ -RF time spectrum shows a peak above a constant plateau, indicating the elevated event rate during the microbunches [Par05b]. After setting an energy window for the photon detectors (column 2), the peak-to-plateau ratio in the $\gamma\gamma$ -RF time spectrum decreases more than one order of magnitude. The $\gamma\gamma$ -RF peak almost vanishes if only photopeak coincident photons within two times the full width at half maximum, i.e. $511 \text{ keV} \pm \text{FWHM}$, are considered (column 3). The energy spectra displayed in column 2 and 3, with software-imposed energy windows, show only events corresponding to the maximum

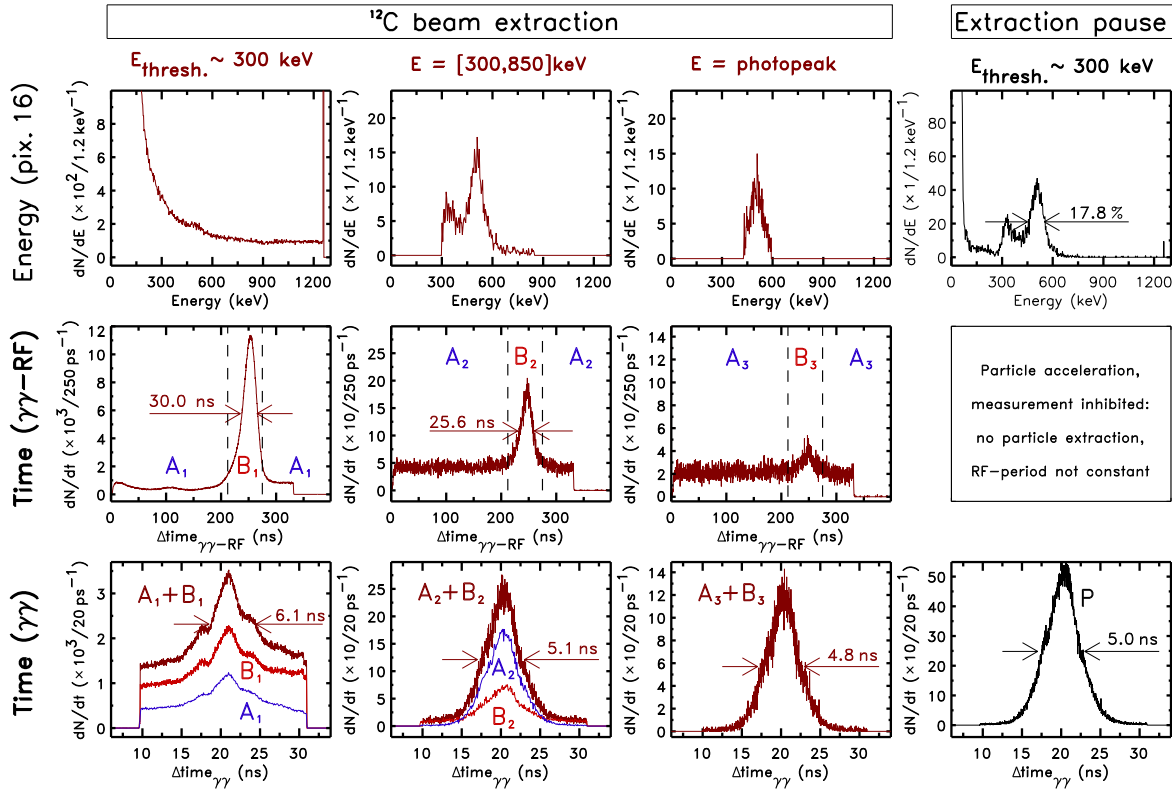


Figure 6.9: Results of $\gamma\gamma$ -RF triple coincidence measurements during ^{12}C beam extraction. The $\gamma\gamma$ coincidence time spectra (lower row) have been constructed by setting different sorting conditions in the γ -ray energy spectra (upper row) and the $\gamma\gamma$ -RF time distributions (middle row). As reference, γ -ray energy and coincidence time spectra acquired in the beam extraction pauses are additionally shown (column 4).

energy in both detectors. In contrary, columns 1 and 4 display spectra with a hardware imposed threshold of about 300 keV, which consequently allows low energy events below the threshold to be seen. These arise due to noise, inter-pixel crosstalk and, more importantly, due to the acceptance of low energy events imposed by higher energy events triggered in pixels elsewhere in the detectors. This behaviour was expected and allowed at this stage in order to be able to analyze low energy events due to the single-pixel threshold implemented. Evaluation of crosstalk is described in section 6.9.3. In conclusion, the $\gamma\gamma$ time spectra in columns 2 (curve A_2) and 3 (curve A_3+B_3) approach the shape seen in the extraction pauses. This indicates that the large peak in the $\gamma\gamma$ -RF time spectra originates indeed from prompt nuclear decay and not from positron annihilation.

6.5.2 Tomographic imaging and quantification of image gain

A broad energy window is normally implemented in commercial PET systems in order to cope with the detector energy resolution, together with detector gain variations with time and temperature between system calibrations. Therefore, the following section presents random suppression results achieved by applying an energy window at each read event of 300 to 850 keV, similar to that of BASTEI (250 to 850 keV) despite the different detector energy resolutions.

Broad energy window: 300 to 850 keV

The activity distributions obtained with a photon energy window between 300 and 850 keV are plotted in Figs. 6.10 and 6.11 for three beam delivery regimes: extraction pauses (P), during extractions but out of Δt_{bg} (A_2), and during extractions but inside Δt_{bg} (B_2). In both figures it can be seen that the events acquired within the microbunch (B_2) exhibit a typical random behavior, presenting a nearly constant spatial distribution (Fig. 6.10, top) corresponding to a plateau (Fig. 6.11, curve B_2) declining beyond the primary particle range, i.e. outside the region where the nuclear reactions predominantly take place. In contrast, events acquired outside Δt_{bg} reproduce well the characteristic β^+ distribution (Fig. 6.10, middle) and depth profile (Fig. 6.11, curve A_2) of the irradiation-induced activity rather well (Fig. 6.10, bottom and Fig. 6.11, curve P).

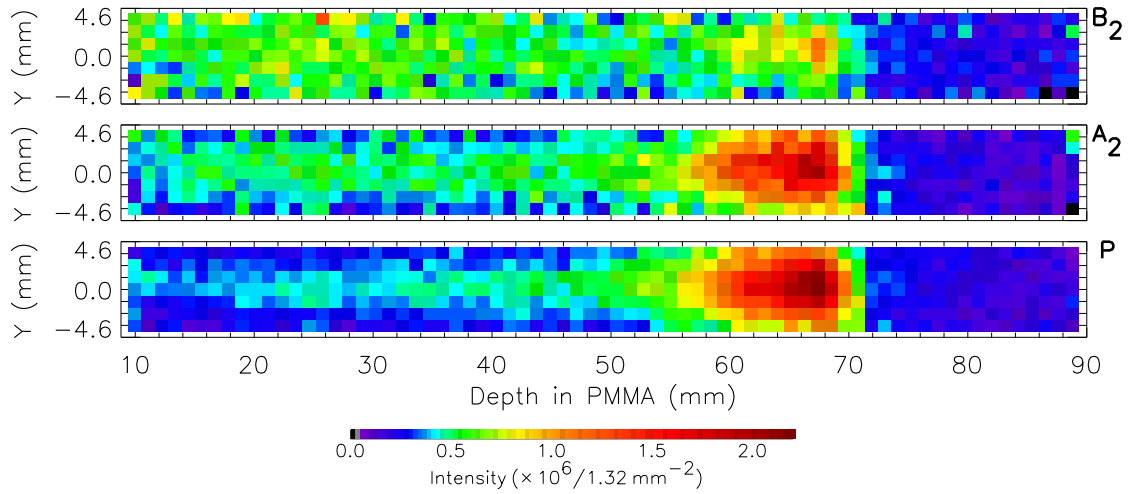


Figure 6.10: Longitudinal tomograms of the activities generated by stopping the beam in a phantom of Lucite and obtained with the $\gamma\gamma$ -RF method (top and middle only). The γ -ray energy window is 300 to 850 keV. The symbols P, A_2 and B_2 , also described in the text, refer to Fig. 6.9.

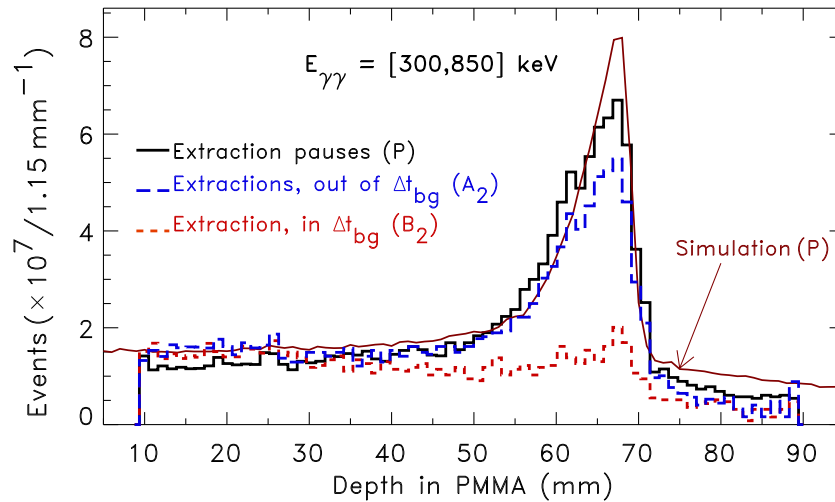


Figure 6.11: Depth profiles obtained with the $\gamma\gamma$ -RF method. The simulation (extraction pauses only) curve was shifted 4 mm to the left in an attempt to compensate for the ion energy loss in the diamond detector ($300\ \mu\text{m}$ thick) and its copper housing.

For image quantification the correction factors mentioned in Table 5.3 were used. These included the solid angle of the two coincident detectors, simulated by starting 10 million events at the isocenter annihilating isotropically and registering the fraction of events detected along one line-of-response (LOR) of two opposing crystals, yielding $\Omega_{LOR} = 2.3 \times 10^{-4}$. Due to the much longer distance between detectors (112 mm) in respect to detector size ($18.4 \times 9.2 \text{ mm}^2$ front face), the central solid angle Ω_{\odot} follows by multiplication with the total number of LOR (32). The total coincidence detection efficiency ε_{tot} of the two opposing detectors is given by

$$\varepsilon_{tot} = \Omega_{\odot} \cdot \varepsilon'_{LOR} \cdot \Pi \cdot (1 - \varepsilon_{PMMA})^2, \quad (6.4)$$

with ε'_{LOR} the efficiency of coincidence photon detection for one LOR. With the photon energy window implemented ε'_{LOR} amounts to 18.1 %. The value of ε'_{LOR} is higher than ε_{LOR} , obtained in section 4.6.3, due to the inclusion of photons from outside the photopeak arising mostly from the lower threshold of 300 keV. The value was calculated by considering the ratio of events measured within the photopeak (FWHM) in both detectors to the events measured within a wide energy window of 300 to 850 keV also in both detectors. This ratio was found to be 3.7, i.e. $\varepsilon'_{LOR} = 3.7 \cdot \varepsilon_{LOR}$. The image fill factor Π was calculated in section 4.6.2 and represents the mean relative solid angle of each image voxel with respect to the central voxel (30.5 %), as determined by flood source measurements. The term $(1 - \varepsilon_{PMMA})^2$ quantifies the probability for double escape of the 511 keV γ -rays from the phantom: 15.2 %.

The simulation of the expected number of counts was achieved with the PosGen Monte-Carlo code [Has96, Pön04], yielding a total of 1.98×10^7 β^+ -decaying nuclei produced per spill (2×10^8 carbon ions with 200.2 AMeV energy). The expected total number of counts $C^{(j)}$ from the decay of isotope j with half-life $T_{1/2}^{(j)}$ follows by integrating the initial activity $A_0^{(j)}$ induced per spill over the 300 spills used (5 s spill period):

$$C^{(j)} = A_0^{(j)} \frac{T_{1/2}^{(j)}}{\ln 2} \sum_{i=0}^{299} \left[1 - \exp\left(\frac{-i \cdot 5 \text{ s}}{T_{1/2}^{(j)} / \ln 2}\right) \right] \quad (6.5)$$

For the calculation of the simulation curve in Fig. 6.11, and because it regards acquisitions in the extraction pauses only (short lived nuclei not imaged), only isotopes with half-lives greater than a few seconds were considered (^{11}C , ^{10}C , ^{15}O and ^{13}N) and the total events detected were multiplied by 3/5 (timing weight of the extraction pauses). Table 6.2 shows the relative production of the most abundant nuclei and its relative decay in a 25 minute measurement due to the effects of the different lifetimes and the fluence delivery throughout 300 spills. In Fig. 6.12 the time evolution of the event rate and the corresponding number of total decaying events is shown for the most abundant isotopes created in PMMA. It was calculated taking into

Table 6.2: Production and decay of positron emitter nuclei after stopping $6 \cdot 10^{10}$ carbon ions with 200.2 AMeV in PMMA. The ions were delivered throughout 300 spills, corresponding to a 25 minute irradiation. Calculated with the PosGen Monte-Carlo code and weighted with Eq. 6.5.

Nucleus	Lifetime	Total generated	Total decaying	Endpoint energy
^{11}C	20.4 min	$4.0 \cdot 10^9$ (68 %)	$2.1 \cdot 10^9$ (55.7 %)	1.98 MeV
^{10}C	19.3 s	$2.8 \cdot 10^8$ (4.7 %)	$2.8 \cdot 10^8$ (7.2 %)	3.65 MeV
^{15}O	2.0 min	$9.2 \cdot 10^8$ (15.6 %)	$8.8 \cdot 10^8$ (22.7 %)	2.75 MeV
^{13}N	10 min	$1.2 \cdot 10^8$ (2 %)	$9.2 \cdot 10^7$ (2.4 %)	2.2 MeV
^{12}N	11 ms	$3.8 \cdot 10^8$ (6.5 %)	$3.8 \cdot 10^8$ (9.9 %)	16.6 MeV
^8B	770 ms	$8.3 \cdot 10^7$ (1.4 %)	$8.3 \cdot 10^7$ (2.1 %)	3.3 MeV

account the formalism described in appendix C. Fig. 6.12 allows to see that the relative weight of short-lived isotopes, measurable only by making use of randoms suppression, increases if the irradiation time is made smaller, which is the current trend due to the accelerator developments mentioned in section 6.1.

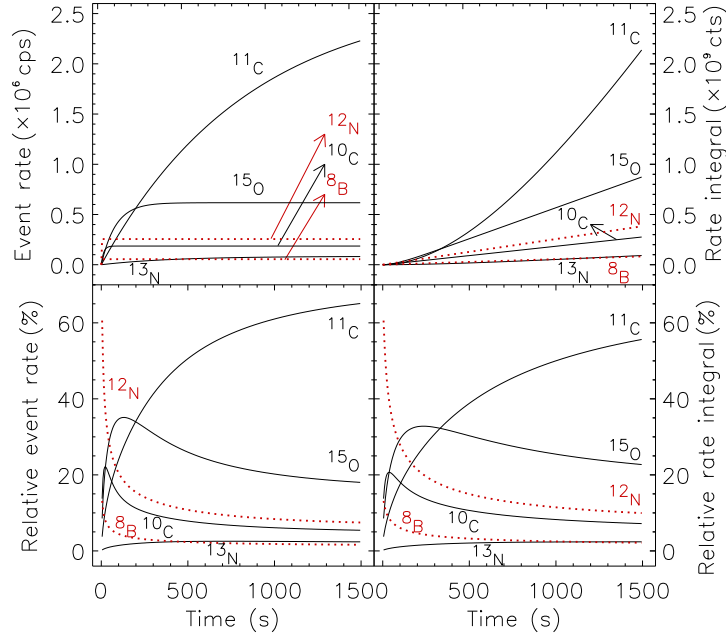


Figure 6.12: Event rate (top left), rate time integral (top right, right y axis), and corresponding relative isotope abundance (bottom) during carbon irradiation of a phantom of Lucite. Only the most abundant products are considered. Beam energy and intensity are 200.2 AMeV and 2×10^8 ions per spill, respectively. The dotted lines plot isotopes with half-lives shorter than a second.

The relative improvement in image counts, ΔC_r , was $\leq 90\%$. It was calculated by dividing the number of coincidences measured during beam extraction, outside the microbunches (image A₂, Fig. 6.10), by the number of events measured during the extraction pauses (image P, Fig. 6.10). This ratio is dependent on the width of the energy window applied, as well as on the beam energy. Table 6.3 summarizes results.

Table 6.3: Increase in image statistics deduced from the β^+ -activity distributions.

Energy window	ΔC_r (peak-to-peak)	ΔC_r (8.8 - 90 mm)	ΔC_r (0 - 90 mm)
300 - 850 keV	78 %	88 %	90 %
Photopeak (2×FWHM)	73 %	75 %	78 %

The values of ΔC_r peak-to-peak, shown in Table 6.3 in the first column with results, correspond to the ratio of the maxima in the two β^+ -activity profiles described in the previous paragraph. For the values of ΔC_r corresponding to a depth in PMMA of 0 to 90 mm, shown in the last column, a constant plateau of activity was assumed to exist between the point at 8.8 mm (beginning of image) down to the point at 0 mm (beginning of phantom, not imaged). The higher relative increase in image statistics obtained with respect to the 65 % estimated in [Eng05c] is suspected to originate from the contribution of short lived, β^+ -decaying isotopes that are detected with high efficiency during the beam extractions for the first time. According to the simulation, and correcting for the measuring time of 25 minutes by using Eq. 6.5, the most

abundant are ^{12}N and ^8B , contributing 9.9% and 2.1% to the total number of annihilation events, respectively (Table 6.2). Note also the higher image blurring at the entrance plateau of activity in Fig. 6.10 (middle, A_2) due to the higher β^+ endpoint energy of these isotopes.

Narrow energy window: photopeak

The random suppression results obtained by selecting events that deposited its energy fully within the photopeak in both detectors are discussed in the present section. The corresponding relative increase in image statistics was already included in Table 6.3.

Figs. 6.13 and 6.14 show the longitudinal tomograms and depth-profiles obtained in the beam extraction regimes under consideration. The measured data in both figures were corrected taking into account Eq. 6.4 but, due to the different energy window, a new value for the efficiency of coincidence photon detection for one LOR (ε_{LOR}'') was used. This value was calculated to be 8.3%, corresponding to $\varepsilon_{LOR}'' = 1.7 \cdot \varepsilon_{LOR}$.

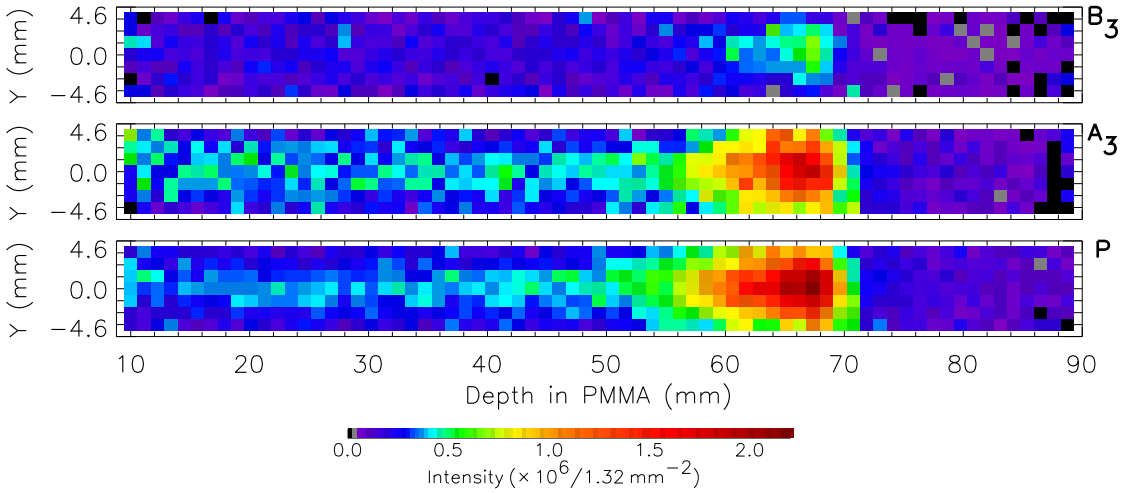


Figure 6.13: Longitudinal tomograms obtained with a narrow energy window (other details as in Fig. 6.10). The symbols P, A_3 and B_3 refer to Fig. 6.9.

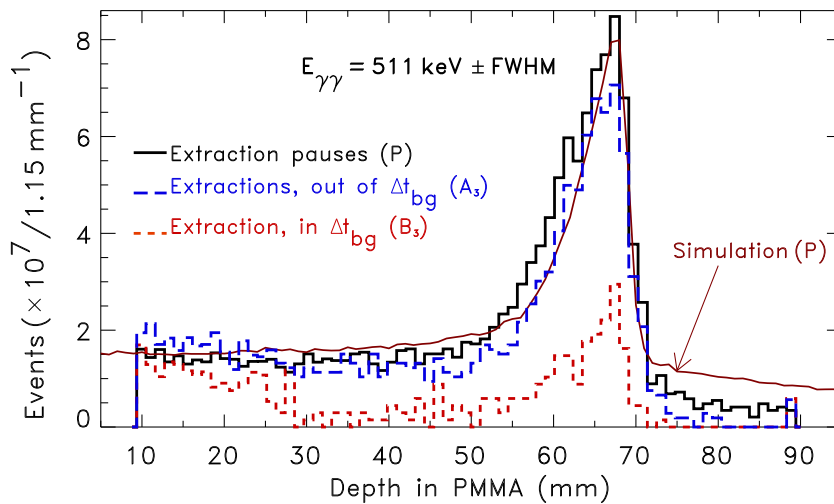


Figure 6.14: Depth profiles obtained with a narrow energy window and the $\gamma\gamma$ -RF method. Simulation and other details as in Fig. 6.11.

From the top image in Fig. 6.13 and curve B₃ in Fig. 6.14 it can be seen that the implementation of a narrow energy window around the photopeak in both detectors filters a great part, but not all, of the events arriving during the macrobunches. This is in agreement with the corresponding $\gamma\gamma$ -RF time spectrum in Fig. 6.9, column 3, where a slight peak above the plateau is still observable. Also observable in the middle image in Fig. 6.13 is the higher image blurring at the entrance plateau of activity due to the higher β^+ endpoint energy of the short-lived isotopes imaged, as pointed out in the last section.

6.6 Results with the $\gamma\gamma$ -Ion Method

The results obtained with the diamond detector are similar to those presented in the previous section ($\gamma\gamma$ -RF) if proper energy selection is applied. Fig. 6.15 compares triple-coincidence time spectra obtained with both methods. In addition to the worse time resolution achieved with the diamond detector, it can be seen that for a relatively high amount of events this measurement was not achieved, which can be quantified by the number of hits in channel zero of the TAC (overload). The amount of unread events with the CVD detector represents 48 % of all events measured during particle extractions. This is thought to originate on the too low threshold implemented on the electronics of the diamond detector, resulting in noise detection and the consequent over-extension of the timing signals. For this reason, the $\gamma\gamma$ -ion analysis has considered only events occurring between 1 and 350 ns in the $\gamma\gamma$ -ion triple-time spectrum, since only these events have physical significance.

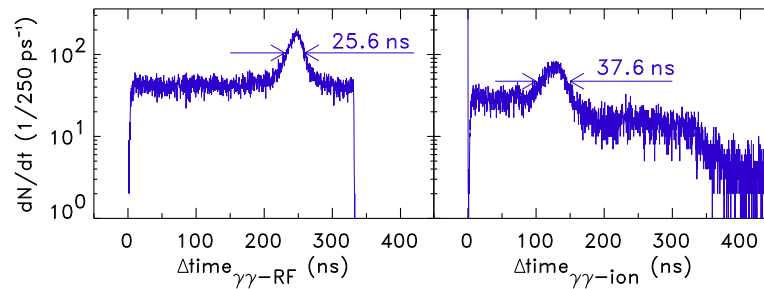


Figure 6.15: Triple-coincidence time spectra: $\gamma\gamma$ -RF (left) and $\gamma\gamma$ -ion (right, measured with the diamond detector). Both spectra correspond to $\gamma\gamma$ events within an energy window of 300 to 850 keV.

6.6.1 Time and energy correlation between $\gamma\gamma$ and $\gamma\gamma$ -ion

A clear correlation between the $\gamma\gamma$ coincidences and the beam microstructure measured with the $\gamma\gamma$ -ion was also observed and is shown in Fig. 6.16. The energy spectra displaying the implemented energy windows, as well as the energy and time measurements performed during extraction pauses, were already shown in Fig. 6.9. Fig. 6.16 shows the time window implemented on the $\gamma\gamma$ -ion spectra in order to separate events collected inside (B') and outside (A') the microbunches. As mentioned, this separation could not be so well achieved as with the $\gamma\gamma$ -RF method due to the too low threshold implemented on the diamond detector that allowed noise measurements to be performed, yielding a low number of events collected in the spectra. Despite this fact, the curves show the same correlations described in section 6.5.1 which allow the suppression of coincident events during beam extraction and the construction of the tomographic images and depth profiles shown in the next section.

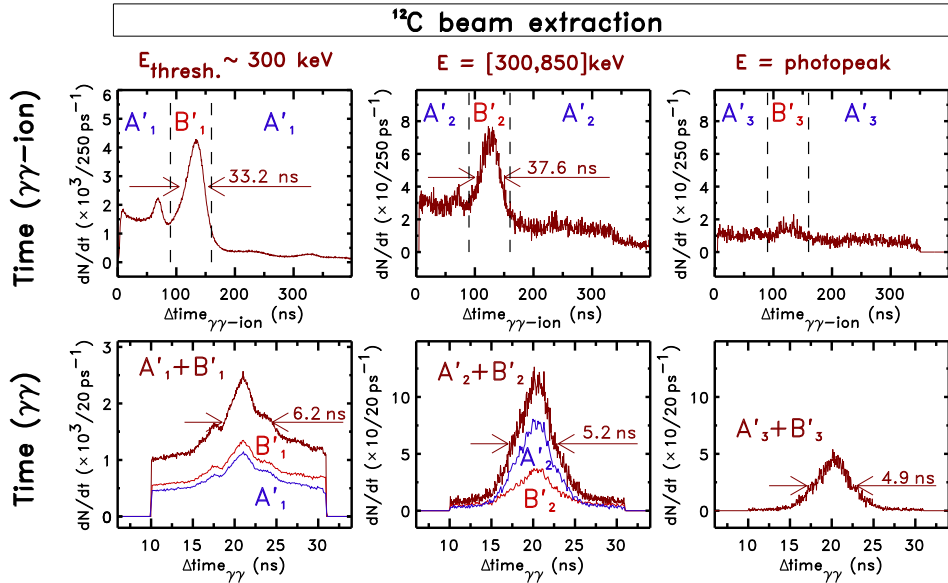


Figure 6.16: Results of $\gamma\gamma$ -ion coincidence measurements during ^{12}C beam extraction with 200.2 AMeV. The time and energy correlations are the same as those described in Fig. 6.9.

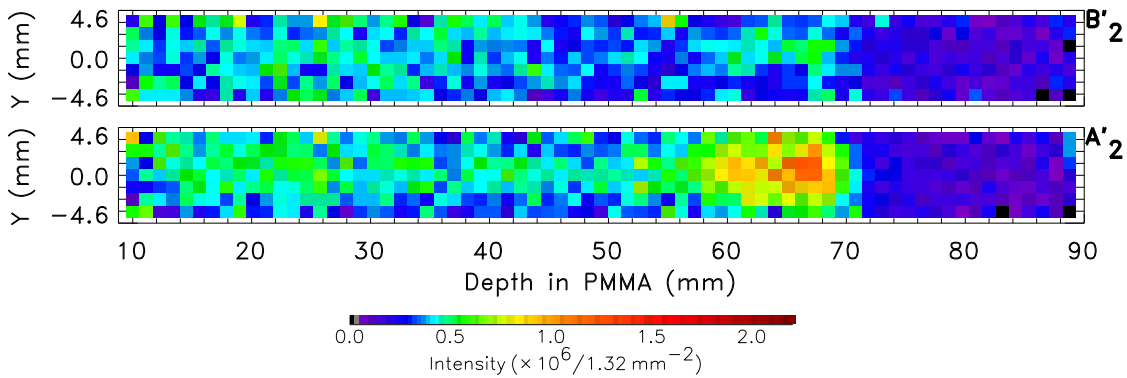


Figure 6.17: Longitudinal tomograms obtained with the $\gamma\gamma$ -ion method. The symbols A'_2 and B'_2 refer to Fig. 6.16.

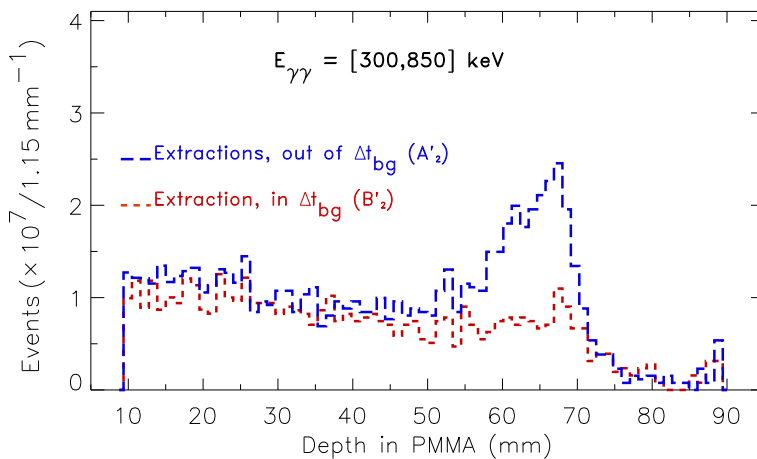


Figure 6.18: Depth profiles obtained with the $\gamma\gamma$ -ion method.

6.6.2 Tomographic imaging

Figs. 6.17 and 6.18 show the activity distributions obtained with a broad energy window from 300 to 850 keV for the two beam delivery regimes collected during beam extractions: inside (B') and outside (A') the microbunches. The activity distributions collected in the extraction pauses were already shown in section 6.5.2 and are not displayed here. In both figures it can be seen that the separation of events collected inside and outside the microbunches is also achieved but with much lower statistics due to the reasons described. The same factors for quantification of image statistics acquired within the energy window of 300 to 850 keV were applied, namely $\Omega_{LOR} = 2.3 \times 10^{-4}$, $\Omega_{\odot} = 7.36 \times 10^{-3}$, $\varepsilon_{LOR} = 18.1\%$, $(1 - \varepsilon_{PMA})^2 = 15.2\%$ and $\Pi = 30.5\%$. Therefore, Figs. 6.17 and 6.10, as well as Figs. 6.18 and 6.11, can be compared directly.

6.7 Time Correlation between RF-Phase and Ion Arrival

As it can be seen in Figs. 6.5 and 6.6, the start signal for both the $\gamma\gamma$ -RF as well as the $\gamma\gamma$ -ion time measurements was exactly the same. Care was taken so that the same cable length was used after the AND gate in Fig. 6.5. This allows to combine, by subtraction on an event-by-event basis, the time information of both measurements to obtain the time correlation between the moment of ion arrival, triggered by the diamond detector, and a given RF-phase, given by the phase-trigger. Eqs. 6.6, 6.7 and 6.8 put in evidence the physical processes inherent to each time distribution acquired, with $*$ denoting the convolution operation in the time domain:

$$\Delta t_{\gamma\gamma-RF} = \Delta t_{RF-det} * \Delta t_{bunch} * \Delta t_{\gamma-emiss} * \Delta t_{\gamma\gamma-det}, \quad (6.6)$$

$$\Delta t_{\gamma\gamma-ion} = \Delta t_{ion-det} * \Delta t_{bunch} * \Delta t_{\gamma-emiss} * \Delta t_{\gamma\gamma-det} \quad (6.7)$$

$$\Delta t_{ion-RF} = \Delta t_{ion-det} * \Delta t_{RF-det}. \quad (6.8)$$

The measured $\Delta t_{\gamma\gamma-RF}$ time distribution in Eq. 6.6 is the result of the convolution of Δt_{RF-det} with Δt_{bunch} , $\Delta t_{\gamma-emiss}$ and $\Delta t_{\gamma\gamma-det}$. The distribution Δt_{RF-det} represents the time resolution achieved by the phase trigger in detecting a fixed RF phase, which was seen in section 6.2.2 to be less than 1 ns; Δt_{bunch} is the time distribution of the ions in the microbunch; $\Delta t_{\gamma-emiss}$ describes the photon or particle emission after the nuclear reaction during the microbunch (section 6.8); and $\Delta t_{\gamma\gamma-det}$ is the time resolution of the the two photon detectors operated in coincidence, shown to be approximately 5 ns in Figs. 6.9 and 6.16. The time distribution $\Delta t_{\gamma-emiss}$ describes all the event emission processes: the events promptly emitted at the nanosecond scale during the microbunch as well as the delayed γ -rays resulting from the several β^+ -decays induced. The $\Delta t_{\gamma\gamma-ion}$ time distribution in Eq. 6.7 results from the same processes except for Δt_{RF-det} , which is substituted with $\Delta t_{ion-det}$ given by the time resolution achieved with the diamond detector in reading the moment of ion arrival. By subtracting (6.6) from (6.7), on an event-by-event basis as mentioned, the dependence on all processes, except those shown in Eq. 6.8, is eliminated¹. This correlation is shown in Fig. 6.19. The double peak structure observed, separated by about one RF-period, was expected due to the different electronics components and cabling implemented on the two stopping channels. Besides the small, slightly peaked continuum observable on the left of each main peak, arising most probably from the noisy conditions at the diamond detector described in section 6.6.1, the packing of

¹ It is important to emphasize that the subtraction of the variables of Eq. 6.6 from those of Eq. 6.7 was done on an event-by-event basis, i.e. from the list mode data and still within the time domain.

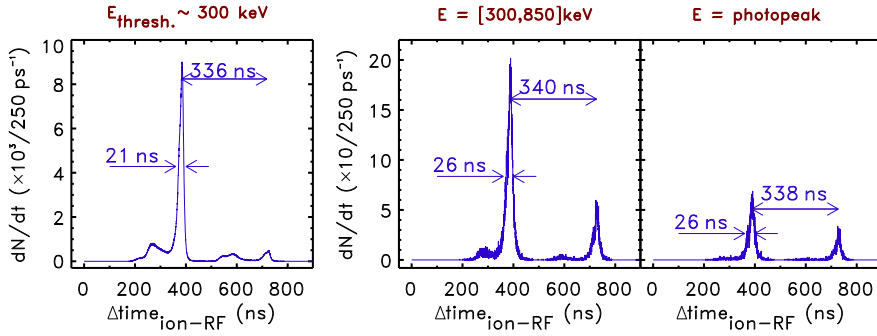


Figure 6.19: Time correlation between RF-phase and ion arrival for different energy windows imposed on the $\gamma\gamma$ events. The spectra were obtained by subtracting (event by event) the diamond detector time value (TAC 3, Fig. 6.5) from the RF time measurement (TAC 2), with a bias of 500 ns to avoid negative values in the spectra.

all events into a single RF-phase is remarkable. Due to the leading edge trigger implemented with the diamond detector (Fig. 6.4) and to the high occ_{RF} of 32 ions per bunch during these measurements, the values obtained for the time resolution between ion arrival and RF phase in Fig. 6.19 (Δt_{ion-RF}) do not correspond to the bunch width Δt_{bunch} (Fig. 6.9), but to the time correlation between the arrival of the first ion in the bunch and a given RF-phase so that $\Delta t_{ion-RF} \leq \Delta t_{bunch}$. If occ_{RF} were of the order of unity or smaller, than $\Delta t_{ion-RF} = \Delta t_{bunch}$ would hold. Table 6.4 summarizes the results obtained for Δt_{ion-RF} and compares them to the measured $\gamma\gamma$ -RF and $\gamma\gamma$ -ion measurements, taken from row 2 in Fig. 6.9 and row 1 in Fig. 6.16, respectively.

Table 6.4: Measured time resolution for ion-RF, $\gamma\gamma$ -RF and $\gamma\gamma$ -ion coincidences.

	ion-RF	$\gamma\gamma$ -RF	$\gamma\gamma$ -ion
Energy window	Time resolution (FWHM, ns)		
≥ 300 keV	21	30	33
300-850 keV	26	26	38

The worse results obtained with the $\gamma\gamma$ -ion method, due to the noise accepted at the diamond detector, were discussed in section 6.6.1. Nevertheless, important information can be drawn by comparing the values of $\Delta t_{ion-RF} = 21$ ns and $\Delta t_{\gamma\gamma-RF} = 30$ ns, measured with an energy threshold of 300 keV, with the value of $\Delta t_{bunch} = 32$ ns FWHM, measured in [Par05b] for the same beam energy. The value of Δt_{bunch} mentioned was measured with a plastic scintillator used as a particle detector and at lower occ_{RF} in order to avoid pulse pileup: the beam intensity was $5 \cdot 10^5$ ions/s which corresponds to $occ_{RF} = 0.16$. Despite the lower value obtained for Δt_{ion-RF} , expected and justified above, the similar time resolutions observed between Δt_{bunch} and $\Delta t_{\gamma\gamma-RF}$ are remarkable and indicate a negligible delay between the moment of particle arrival and single photon emission¹. As a consequence, the application of a time window for random suppression needs to consider only the time distribution of the ions in respect to the RF-phase, i.e. Δt_{bunch} .

¹ This is valid at the nanosecond time scale under discussion, with instrumentation of interest for in-beam PET. Faster timing techniques applied to a narrower beam microbunch, or to the present microbunch time structure but with $occ_{RF} \leq 1$, will of course be able to detect the delay between ion arrival and single photon emission (section 1.2.1).

6.8 Events with Higher Energy

Due to its influence on the system dead time and on the count rates achieved, the depth profiles and detector hit patterns of coincidences with energy values above 300 keV and above 1200 keV (ADC overload) were analyzed. This information is necessary since commercial PET systems, including BASTEI, applying energy discrimination for coincident events do not apply it on the channels processing the singles rates [Lub04]. Consequently, dead time estimations on these systems do include the full energy spectrum of detected events and, therefore, this knowledge for quantitative in-beam PET is of high importance.

6.8.1 Depth profiles and event hit multiplicity

Fig. 6.20 shows the depth profiles obtained with the higher energy events mentioned. It can be seen that the typical random or β^+ -activity profiles of Fig. 6.11 are substituted by profiles with counts increasing with the penetration depth, suggesting the detection of events emitted preferentially in the forward direction, as noted in [Par05b] for a single detector and described in section 5.3 for these multi-pixel detectors. Although it is known that a flux of particles of mainly protons and neutrons, but also other light nuclei, escapes the target volume in the forward direction [Gun04a, Gun04b], it is not clear whether the profiles observed in Fig. 6.20 arise from γ -rays, particles or both. In order to gain some insight into this quest, the event hit multiplicity, i.e. the number of triggered pixels in each detected coincidence, was analyzed.

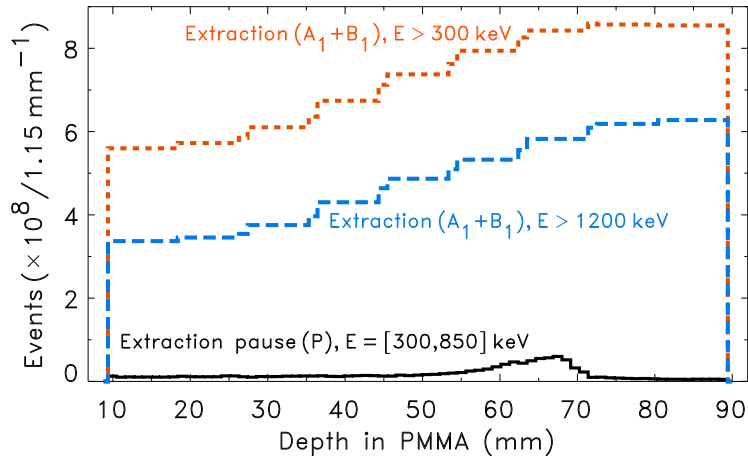


Figure 6.20: Depth profiles of coincident events with higher energy values registered during beam extractions. The profiles show the average of the events seen by the full detector rather than a pixel-based backprojection due to the impossibility of energy discrimination above 1200 keV (ADC overload, Fig. 6.9). The β^+ -activity profile measured during the extraction pauses is also shown for comparison.

Fig. 6.21 shows the hit multiplicities obtained during beam extraction, separated by different event energies and plotted for the full scan of the detectors as depicted in Fig. 5.8 (except detectors positioned at 90 mm), as well as for the first and last positions of the detectors in these random suppression measurements. It can be seen that the hit multiplicities obtained for the low energy events (photopeak and energy window from 300 to 850 keV) decrease monotonically and continuously, presenting low mean multiplicity values close to unity (Table 6.5) as expected from the single hit characteristic of photons in such small detectors. The only phenomenon expected to contribute to higher multiplicity at these energies is multiple Compton scattering in the LSO crystals. Interpixel crosstalk (measured to be about 10 %, section 6.9.3), which higher energy events creating a false low energy trigger in neighbouring pixels, is ruled out since the

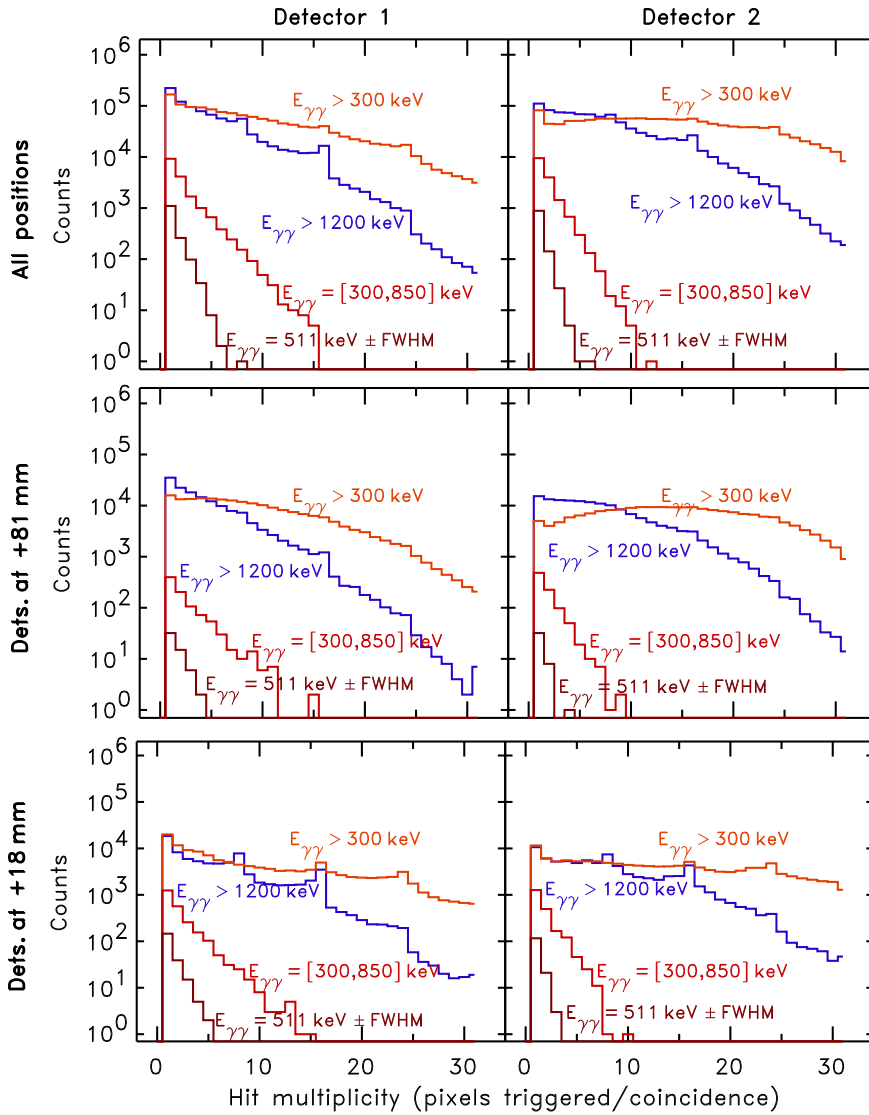


Figure 6.21: Histograms with the event hit multiplicity for different energy windows. The detector positions refer to Fig. 5.8. The analysis of all the events corresponding to the full scan with the detectors is signed as All positions.

Table 6.5: Mean hit multiplicity per coincidence. Detector positions after Fig. 5.8.

Energy window	Extr. pauses		Extractions					
	All positions		All positions		Dets. at +18 mm		Dets. at +81mm	
	Det. 1	Det. 2	Det. 1	Det. 2	Det. 1	Det. 2	Det. 1	Det. 2
511 keV \pm FWHM	1.0	1.0	1.4	1.0	1.4	1.0	1.6	1.0
300-850 keV	1.3	1.2	2.1	1.0	2.2	1.0	2.6	1.0
≥ 300 keV	1.1	2.0	8.9	12.5	9.5	12.0	9.0	13.5
≥ 1200 keV	1.1	1.0	4.9	5.2	6.1	5.3	4.5	5.6

signal with maximum amplitude in each detector was requested to be within the specified energy window. If the number of photons detected per coincidence increases, e.g. by considering wider energy windows in the detected data, the curves showing the hit multiplicity are expected to decrease their slope (absolute value), but conserving the continuous behaviour described. This is observed in the multiplicity curves of Fig. 6.21 corresponding to events detected with energy

above 300 keV, remarkably continuous for the detectors positioned at 81 mm. On the contrary, coincidences with energy values above 1200 keV present discontinuous multiplicity curves, with sharp falls occurring precisely at every eight pixels and, therefore, strongly suggesting the passage of charged particles through the detectors in a longitudinal direction along the beam (each 8×4 pixels detector was positioned with the 8 pixel rows aligned horizontally, parallel to the beam direction). These particles could have their origin both inside the phantom stopping the beam as well as on the diamond detector and its housing, trespassed upstream.

The asymmetry in mean hit multiplicity between detector 1 and 2 (Table 6.5) can be explained based on the slightly higher threshold implemented on detector 2 (therefore smaller hit multiplicity at lower energies) as well as based on the malfunctioning of two pixels (one per detector, section 6.9.1) that were shut off. Since the malfunctioning pixel of detector 1 was positioned closer to its center (maximum solid angle), the hit rejection was higher on this detector and, consequently, its average hit multiplicity lower.

Although these results do not suffice to prove the nature of the particles creating the high energy event profiles of Fig. 6.20, they do indicate the necessity of setting an upper energy threshold close to 511 keV during in-beam PET measurements.

6.8.2 Event rates

The increase in image statistics obtained is valid for the present beam delivery system with a duty factor D_f of 40 %, with $D_f = \Delta t_M / T_M$, Δt_M being the macropulse duration (beam extraction, 2 s) and T_M being the time of a synchrotron acceleration cycle, comprising beam injection, acceleration and extraction (5 s). In order to estimate the gain in collected events for therapeutic beams delivered with other accelerators with different D_f and microstructure timings, the knowledge of the event count rates is necessary. This is shown in Fig. 6.22, where

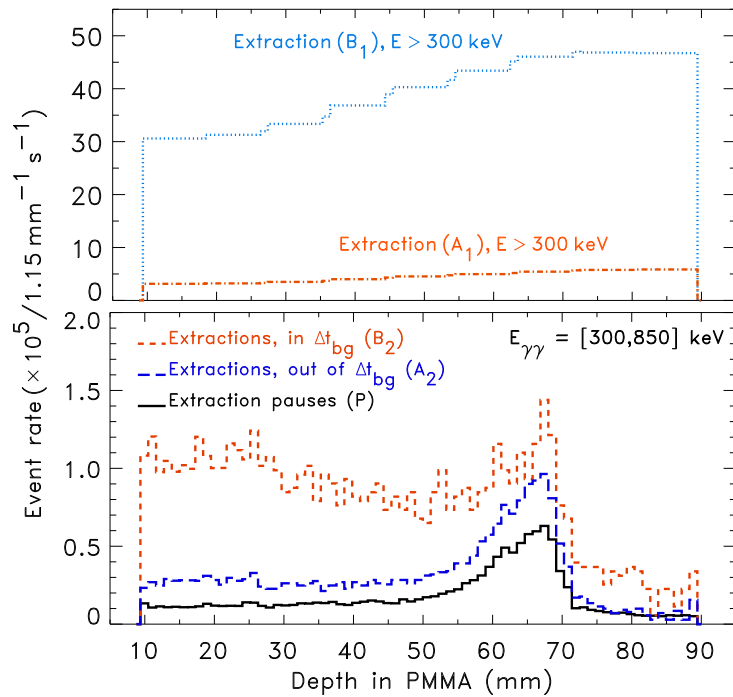


Figure 6.22: Event rate profiles in different beam delivery regimes. Rates were corrected for the solid angle of the detectors assuming isotropic event emission. The high event rate during beam extraction is remarkable.

the number of events collected in each regime was divided by the total length of the time window in which it was collected. It must be noted that an extrapolation of these results to a PET system with larger solid angle is only feasible in the case of the curves showing the isotropic, β^+ -decaying events (P and A₂). The remaining curves regard anisotropic fluxes and will of course yield count rates and image deterioration dependent on the position of the detectors, as described in section 5.3 as well as in [Par05b, Cre04].

6.9 Detector Performance

The results obtained in the present chapter are related to the properties of the imaging detectors used which, in turn, differ slightly from those described in chapter 5, section 5.3, due to different operation parameters implemented, such an increased high voltage in order to achieve better timing performance. Since any in-beam PET to be implemented a posteriori must carefully consider these properties, the main performance parameters of the detectors used are summarized below.

6.9.1 Longterm stability

The present experiment required operating the detectors one year after their last in-beam experiment (chapter 5), and one and a half year after their initial setup. Two pixels were found working inappropriately: correct energy spectra could only be acquired at the expense of extreme amplifier gain and timing with these two pixels was not possible. This is thought to arise from an insufficient coupling of the scintillators to the surface of the APD due to exposure of the detectors to the vibrations during long traveling. Therefore, it can be concluded that silicon glue and teflon tape (chapter 4, section 4.5, and [Kap04]) provide a good, long-lasting solution for manufacturing these detectors.

6.9.2 Energy and time resolution

Because time resolution was an important issue during the present measurements, the APDA were operated with an internal gain of 70 instead of gain 50, section 5.2 and [Cre03]. As expected, the timing performance of the two LSO/APDA detectors improved to 5.0 ns FWHM from 6.2 ns FWHM at the cost of worse energy resolution: $16.5 \pm 0.3\%$ FWHM versus the $15.5 \pm 0.3\%$ FWHM presented in section 5.2 and [Cre03].

6.9.3 Inter-pixel crosstalk

An inter-pixel crosstalk of about 10% was observed, meaning that a 511 keV photon fully depositing its energy in a given pixel leaves a signal of ~ 50 keV in its neighboring pixels due to optical crosstalk only. The reasons for this are the incomplete light isolation of the teflon tape surrounding the LSO crystals and the light sharing at the LSO-diode coupling mostly due to the common, thick epoxy layer covering all diodes (section 4.4.3). Inter-pixel crosstalk plays a role in estimating count rates since high energy events (e.g. a 5 MeV signal from a crossing particle) may leave in its neighbor a false signal (500 keV). In the present data evaluation all pixels were read and analyzed and the pixel with maximum energy was selected in each detector for energy windowing followed by image processing, thus crosstalk events are automatically rejected since their signals have less amplitude than that of the pixel where the real event took place. Future applications must apply either the same principle or a hardware energy selection that is able to reject a full cluster of pixels once a high energy event is detected in one of them. In summary, applying energy windows is sufficient for event selection for tomographic imaging but image quantification requires considering all events impinging the detectors. These findings may be

of importance in conventional nuclear medicine PET [Lub04] and are of utmost importance for random suppression and image quantification during in-beam PET measurements.

6.10 Application to Radiotherapeutic Beams

The applicability and usefulness of the methods presented depend on the timing characteristics of the therapeutic beam where the methods are to be applied. The importance of random suppression during in-beam PET measurements increases as the accelerator duty factor D_f increases. For example, linear accelerators for electron, photon and even ion [Ama04] radiotherapy have extremely small duty factors ($\sim 0.1\%$) and, consequently, the random suppression method summarized in section 1.4.2 and detailed in [Paw97, Eng04b] suffices for in-beam PET at these machines. In contrary, isochronous and superconducting cyclotrons used for ion radiotherapy [Ros00, PSI99, Kim01] deliver continuous wave (CW) beams ($D_f \cong 100\%$), which render in-beam PET implementable only with the present random suppression methods. Synchrotron-delivered radiotherapeutic beams have duty factors between 10 and 90% [Hab93, Eic03, Fur03, Cou04], meaning that such facilities can considerably profit from the application of the random suppression techniques presented here. Table 6.6 emphasizes these conclusions by summarizing the timing characteristics of several radiotherapy facilities worldwide. The values given for Δt_{bg} represent the FWHM of the bunch. All random suppression results presented in this chapter reserved a time window of $2 \times \text{FWHM}$ about the microbunch.

Table 6.6: Time characteristics of some therapeutic beams worldwide. The symbol T_M refers to the period of the macropulses of the accelerator, D_F refers to its duty cycle, T_{RF} is the period of the RF signal, Δt_{bg} is the typical bunch width, and $\overline{\text{ocCRF}}$ the mean RF occupancy.

Facility	Acc. type	Ion(s)	T_M (s)	D_f (%)	T_{RF} (ns)	Δt_{bg} (ns)	$\overline{\text{ocCRF}}$ (ppb)	Ref.
Catania	Cycl.	p	n.a.	CW	30	4-6	300	[Cir04]
GSI	Sync.	C	5	~ 40	480-250	~ 30	13.9	[Hab93]
Heidelberg	Sync.	p-O	2-12	8-92	284-148	n.k.	8.0	[Eic03]
HIMAC	Sync.	C	3.3	61	151	n.k.	n.k.	[Fur03]
Loma Linda	Sync.	p	2.2	82	109-10 ³	n.k.	1471	[Cou04]
NPTC	Cycl.	p	n.a.	CW	9.4	0.8	118	[Ros00]
PSI	Cycl.	p	n.a.	CW	19.75	0.3	n.k.	[PSI99]
TERA	Sync.	p	1	65	80	n.k.	n.k.	[Buc96]
TERA	Linear	p	5 ms	0.06	0.33	0.03	n.k.	[Ama04]

Catania: Laboratori Nazionali del Sud, Catania, Italy.

Heidelberg: Heavy Ion Cancer Therapy Facility, Heidelberg, Germany.

HIMAC: Heavy Ion Medical Accelerator in Chiba, Japan.

Loma Linda: Loma Linda Univ. Proton Treatment Center, Loma Linda, USA.

NPTC: Northeastern Proton Treatment Center, Boston, USA.

PSI: Paul Scherrer Institute, Villigen, Switzerland.

TERA: TERapia con Radiazioni Adroniche, Novara, Italy.

n.a.: not applicable n.k.: not known ppb: particles per bunch CW: continuous wave

6.10.1 Implementation at GSI and at the Heidelberg clinics

A mean RF occupancy of 13.9 carbon ions per bunch was calculated for the GSI facility by considering all combinations of beam energies and intensities used to treat all patients to this date (Fig. 6.23). Extrapolating these values to the synchrotron parameters at the future ion

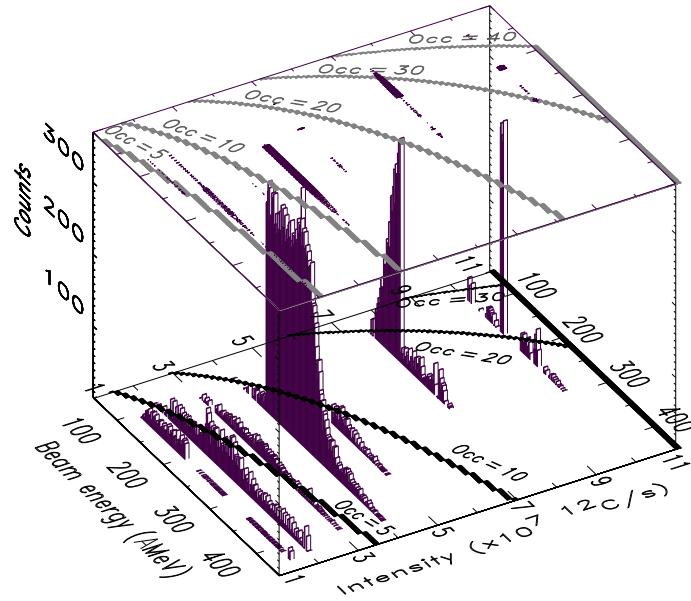


Figure 6.23: Histogram with the combined beam energies and intensities used to treat 240 patients at GSI between January 1998 and August 2004. Overplot are several RF occupancy curves at GSI (top, grey) and at the future synchrotron in Heidelberg (bottom, dark).

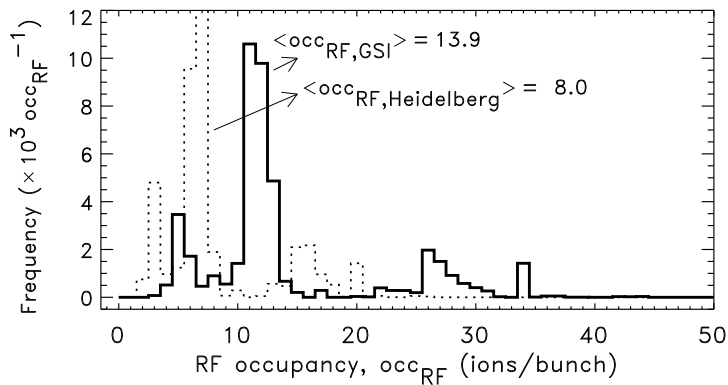


Figure 6.24: Histograms with the RF occupancies at GSI (solid curve) and expected for Heidelberg (dashed curve), corresponding to Fig. 6.23.

therapy facility in Heidelberg, with an even higher duty factor, yields $\overline{occ_{RF}} = 8.0$ ^{12}C ions per bunch. This value indicates that there may be an advantage, from the point of view of timing (Fig. 6.3), in using the $\gamma\gamma$ -ion in respect to the $\gamma\gamma$ -RF method for this facility. Nevertheless, the smaller stopping power of ion species with lower atomic number than carbon, and the lower relative biological effectiveness of these species, require the beam intensity to be magnified if the same dose is to be applied. Consequently, a higher RF occupancy is to be expected for ions lighter than carbon, which renders, apart from carbon and oxygen ions, the $\gamma\gamma$ -RF and $\gamma\gamma$ -ion methods identical in this aspect.

Despite the noise problems presented in section 6.6 for the diamond detector, arising from normal first-attempt experiments, the $\gamma\gamma$ -ion method is easier to implement in real therapeutic situations since it does not require a correction for the transit time of the ions in the beam pipeline (which is dependent on beam energy). Nevertheless, it has the drawback of requiring

additional material in the beam path. This would become an advantage if the fast particle detector could be used also as a beam monitor [Per04, Ber01], which is not a trivial task since a large area, position sensitive detector covering the whole beam delivery portal ($20 \times 20 \text{ cm}^2$ at GSI) would have to be assembled. In addition, the very high mean occ_{RF} for proton treatments, e.g. 1479 particles per bunch at the Loma Linda synchrotron (Table 6.6), requires the eventual beam monitor to be able of performing charge integration in order to detect ions overlapping in time. In summary, an ultra-fast, particle counter detector with a large dynamic range would be required, which is indeed a technological challenge. One possible alternative to the large size of the beam monitor would be to position a small area, fast particle detector at the last beam focus in the accelerator pipeline. Nevertheless, this again would require a correction for the ion transit time in the beam pipe.

6.10.2 Cyclotron-delivered therapeutic ion beams

In-beam PET implementation at cyclotron-based facilities seems to be non-trivial because of the small time differences between Δt_{bg} and T_{RF} , with Δt_{bg} ranging from 0.3 ns [PSI99] to about 6 ns [Cir04] and T_{RF} from about 10 ns [Ros00] to 30 ns [Cir04]. On the accelerator side, two methods to increase T_{RF} are possible [Bra99]. One makes use of single turn extraction, which allows delivering an arbitrary pattern of beam pulses produced with a combination of bunching and chopping at the injection level (more difficult for heavy ions). The second uses multi turn extraction followed by a subharmonic buncher that reduces the beam repetition rate to the orbital frequency [Bra99]. Nevertheless, in order not to disturb the optimal operation of the cyclotron, the best solution should arise from the use of fast scintillators combined with appropriate very fast signal processing electronics, e.g. as proposed [Lec02] and already achieved [San04] with LSO/APDA used for positron emission mammography (PEM).

6.11 Summary and Outlook

Two methods for suppressing the high-yield, micropulse-induced random coincidences during beam extraction have been tested successfully at the medical beam line at GSI. With the accelerator duty cycle of 40 % installed there, the increase in image statistics was measured to be between 70 and 90 %. Both random suppression methods are based on the synchronization of the $\gamma\gamma$ -coincidences measured in-beam by the positron camera with the time microstructure of the beam, either by using the RF-signal from the accelerator or the signal of a thin diamond detector placed in the beam path in front of the target. Energy and triple-coincidence time correlated spectra and tomographic images of the β^+ -activity induced by the beam in a plastic phantom, first-measured during beam extraction, have clearly confirmed the feasibility of the proposed random suppression methods. In addition, tomographic imaging of short-lived β^+ -decaying isotopes that could not be discriminated so far due to the high event flux within the microbunches, could be performed. Both methods indicate that in-beam PET random suppression can be achieved by applying narrow energy windows about the 511 keV photopeak on each pair of detectors. Nevertheless, since such narrow windowing is unfeasible with the current electronics implemented in commercial PET tomographs, a broader energy window was applied at the detectors, providing the same level of random suppression if the moment of coincidence arrival was time correlated with the beam microstructure. The methods provide a solution for implementing in-beam PET in hadrontherapy facilities with synchrotron and cyclotron delivered beams with high duty factors or continuous wave, respectively. Namely, and more importantly, they provide a solution for applying in-beam PET at synchrotron-based, heavy ion radiotherapy facilities [Hea98, Sie04] with an optimized beam delivery duty factor where in-beam PET data taking can be compromised if none of these random suppression

methods is applied.

Despite the positive first results, the random suppression methods presented still require a system that corrects for the transit time of the ions in the beam pipeline (ion transit time is energy dependent) before being applied to a therapeutic system either with the $\gamma\gamma$ -RF method or with the $\gamma\gamma$ -ion method, with the fast particle detector positioned at the last focus of the accelerator. If a fast particle detector capable of performing beam monitoring is developed (detector size, speed and energy proportionality are an issue), then such a position sensitive detector must have an area of $20 \times 20 \text{ cm}^2$ and a disjunctively connected output of all its pixels must be made available to the in-beam PET data acquisition system.

Chapter 7

Conclusions and Outlook

Several objectives pursued within the present work, optimization of in-beam positron emission tomography applied for the monitoring of heavy ion tumor irradiation, have been met. In some issues a first, important step towards an optimization has been given, but future work is still needed, as detailed below.

The most important limitation of in-beam PET firstly addressed in this work was the problem of image artifacts arising from limited angle tomography. The present reconstruction routine applies a penalization factor at image voxels located far from the isocenter, preserving image proportionality at the isocenter, where the tumor is located. In order to understand the source of these artifacts, and in order to be able to propose a detector configuration that minimizes them, two software tools were constructed. The first was a tomograph simulation capable of handling variable detector configurations, simulating the detection of the annihilation radiation and providing a versatile detector encoding scheme. The second consists of a flexible reconstruction routine able of reading and treating mathematically the output of this simulation. This reconstruction routine extends the mathematical data treatment already implemented for the in-beam tomograph at GSI. It presents a novel approach for 3D data histograming and allows, therefore, real 3D tomographic reconstruction. Although this routine provides a reconstruction solution for next-generation, optimized in-beam positron emission tomographs, it presents two limitations. These are the large processing time and large memory size required if very large data sets are handled, as is the case with irradiation in the pelvis region. In order to reduce the processing time the routine must be adapted to the ordered subsets estimation algorithm (OSEM), which reduces the number of iterations from the present fifty to only a few. Concerning the large memory size, modern computers already provide a working solution. This can be seen by the pelvis irradiation images presented throughout this work. They correspond to a large image volume and data size, and were processed with normal, commercial computers. Nevertheless, the development of a 3D system matrix exploiting the symmetries existing in the processes of emission tomography will greatly reduce both time and memory demands in PET reconstruction algorithms.

Using the simulation and reconstruction routines mentioned, the origin of several artifacts was identified to be dependent on the gaps between the two heads in a dual-head detector system. Two detector configurations for next-generation, improved in-beam PET were proposed: a dual-head tomograph with small gaps, allowing the incoming beam to arrive to the tumor, and a closed ring tomograph. The closed ring tomograph must be positioned, during patient irradiation, tilted in respect to the direction of the incoming beam. In order to evaluate the optimum detector configuration with real patient data another simulation code, previously developed by past members of this team, was used. This code, named PosGen, generates β^+ -activity distributions based on the computed tomogram of a patient and on a given irradiation plan. Within this work the PosGen code was slightly modified in order to be coupled with

the routine simulating the several tomographs. The images obtained after reconstruction show a clear advantage for closed ring tomographs if large irradiation fields, like irradiation in the pelvis region, are to be monitored with in-beam PET.

Integrating either proposed detector configuration into future heavy ion treatment facilities was also studied. For horizontal, fixed beam lines it was seen that both configurations can be implemented with slight modifications in respect to the solution presently installed at GSI. For isocentric, rotating beam deliveries several proposals were analyzed. It was seen that implementing in-beam PET in the beam gantry, a solution developed at GSI, offers the most advantages. This GSI solution was further extended, within this work, in order to allow for a closed ring tomograph to be implemented.

The limitations imposed by the low statistics data sets of in-beam PET images were also addressed in this work. Three reasons exist for this. First, the amount of nuclear reactions inducing β^+ -decaying isotopes is, per se, relatively small in comparison to the incoming ion fluence. The statistics of in-beam PET images will improve if the number of treatment fractions is reduced (higher dose per fraction). This item was not addressed in the present work. Second, a high number of annihilating events is lost due to biological mechanisms like washout, or due to the low detection efficiency provided by a dual-head tomograph with large gaps. This loss of events is reduced with the detector configurations proposed for next-generation tomographs: a closed ring, or a dual-head tomograph with small gaps. And third, data taking during particle extraction is presently vetoed due to the presence of a high background that overlaps the annihilation signal.

The problem of high noise during particle extractions was first addressed by other members of the in-beam PET team. A demanding research work, envisaged at understanding the mechanism originating the high background noise existing during particle extractions, was put forward. A correlation existing between the moment of arrival of background events with the arrival of the carbon ions, synchronized with the radiofrequency (RF) signal from the accelerator, was found and exploited. This provided the knowledge for developing a technical solution, within this work, in order to allow in-beam PET data taking during particle extractions. Such solution was required for two reasons. First, in order to increase the statistics of the presently acquired images. Second, and more importantly, in order to allow in-beam PET to be implemented at future facilities using optimized synchrotron or cyclotron accelerators. This is because recent developments in accelerator technology result in beam extraction times occupying close to 100 % of the accelerator duty cycle. Two technological solutions for suppressing the high noise background of in-beam PET were proposed in a patent, and verified experimentally at the GSI medical beam line within this work. This verification, using a triple coincidence technique, allowed for the first time to readout, and image, double- γ -ray events correlated with the moment of ion arrival during particle extraction. Two γ -ray, position sensitive detectors, with 32 pixels each, were assembled and used. A very thin diamond detector, positioned in the beam path as an ion detector, was used to signal the moment of ion arrival. A fast, RF-trigger electronics module, developed in house, was used to time a given phase of the RF-signal from the accelerator. A pencil-like beam was stopped in a phantom and the 2D images and depth profiles, obtained for the first time during particle extraction, clearly show the feasibility of the two technical solutions proposed in the patent. These images and profiles allowed also to gather evidence about the influence of short-lived, β^+ -decaying isotopes with higher endpoint energies. These short lived isotopes could not be discriminated so far due to the high event flux within particle extractions. Nevertheless, a measurement of their lifetimes could not be performed, meaning that a clear proof of their detection is still lacking.

But the positive background suppression results were obtained with a fixed beam energy. Sev-

eral challenges must be addressed before either of the random suppression methods is applied onto a therapeutic site equipped with in-beam PET. One random suppression method correlates the incoming γ -rays with the moment of ion arrival based on a fast particle detector positioned in the beam path. If this method is used, then a fast particle detector capable of performing beam monitoring must be developed. Detector size, speed and energy proportionality are an issue. Furthermore, such a position sensitive detector must have an area of $20 \times 20 \text{ cm}^2$ and a disjunctively connected output of all its pixels must be made available to the in-beam PET DAQ system.

Another random suppression method correlates the incoming γ -rays with a given phase of the RF-signal from the accelerator. Since the transit time of the ion in the beam pipeline depends on its energy, the RF-phase that properly vetoes the high background noise will also depend on the beam energy. Therefore, a system that corrects for the transit time of the ions in the beam pipeline is necessary in this situation. In addition, the RF-phase trigger must provide a digital output with constant delay in respect to any input frequency, i.e. it must not depend on beam energy. One possible solution verified experimentally is described in appendix D.

Concerning detector development, a great effort was put in this work onto assembling and testing state-of-the-art technology specially adapted to the requisites of in-beam PET. Two position sensitive, γ -ray detectors consisting of finger-like crystals of lutetium oxyorthosilicate (LSO) coupled to two avalanche photodiode arrays (APDA) were assembled. The substitution of the conventional photomultiplier tube (PMT) by APDA provides the magnetic field resistance needed for the next-generation, in-beam PET detectors. Such fields, generated by the last beam bending magnet, will be present if in-beam PET is installed onto isocentric, rotating beam deliveries. In addition, the more than ten times smaller dimensions of APDA in respect to PMT will allow a huge volume reduction of positron emission tomographs built with such detectors. Furthermore, the energy and time resolutions measured with the new detectors, better than those obtained with the presently installed detectors, are directly related to the quality of PET images. The in-beam imaging capability of these LSO/APDA detectors were tested under or after harsh irradiation conditions. In one experiment the detectors were positioned up and downbeam from a target irradiated with a fluence equivalent to 1000 typical daily therapeutic fractions. A line source positioned between the detectors was imaged, allowing parameters like time, energy and spatial resolution to be compared before, during and after irradiating the target. A second experiment imaged the β^+ -activity distribution generated by a monoenergetic beam in a target of Lucite. In addition, a third experiment exposed a scintillator block of LSO to the flux of light particles leaving two single-portal patient treatments. Germanium-detector-based, spectroscopic γ -ray measurements showed no scintillator activation. These combined results prove the feasibility of using an LSO/APDA detector for next-generation, improved in-beam PET scanners with high detection efficiency and reduced image artifacts.

But, due to the small amount of ^{176}Lu , a natural radioactive element, in LSO, the influence of the natural background activity density of LSO onto an LSO-based tomograph had to be estimated. It was seen that, in order not to compromise the quality of the low-statistics in-beam PET images, modern, digital data acquisition techniques are necessary in order to reduce the coincidence time resolution of the detectors to a full width at half maximum (FWHM) of 1 ns or below.

Finally, the impact of recent developments in ultra-fast timing detectors, potentially allowing the implementation of the time-of-flight technique onto commercial PET scanners, was extrapolated to in-beam PET. Very promising results can be achieved if future PET detectors with a coincidence time resolution below 200 ps FWHM can be built.

Appendices

Appendix A

A Factorization Scheme for 3D Tomographic Data

In order to be able to optimize the detector geometry for in-beam PET scanners, a set of simulation and reconstruction routines capable of handling a high number of coincidence channels, corresponding to a high resolution, closed ring tomograph, was needed. If the ECAT[®] EXACT[™] HR⁺ tomograph (CTI PET Systems Inc.) is considered, containing 32 complete detector rings, the total number of single detector channels is 18 432. Since in-beam PET is characterized by low statistics data-sets sampled with a limited angle tomograph, rebinning the 3D collected data into 2D sets disturbs the spatial information of the few lines-of-response (LOR) existing, which vetoes the application of already existing rebinning algorithms. Therefore, a fully 3D implementation of the maximum likelihood expectation maximization (MLEM) algorithm was done [Cre02, Cre05b] by making use of the system symmetries and coincidence channel possibilities illustrated in Figs. A.1 and A.2.

Fig. A.1 shows the pixel numbering scheme implemented both in the simulation and in the reconstruction routines. For every detected coincidence the simulation registers, in list mode, two numbers corresponding to the pixels hit. It is up to the reconstruction routine to histogram the incoming list mode data appropriately before proceeding with the iterations of the MLEM algorithm. In order to handle the enormous amount of crystal combinations possibilities, close to 170 million, dynamic memory allocation was necessary together with a factorization scheme that allowed the reconstruction to handle only non-empty coincidence channels. For that, all possible coincidence possibilities were analyzed, as depicted in Fig. A.2. It can be seen that a total of 5 299 200 and 164 275 200 crystal combinations can occur within intra-ring and inter-ring

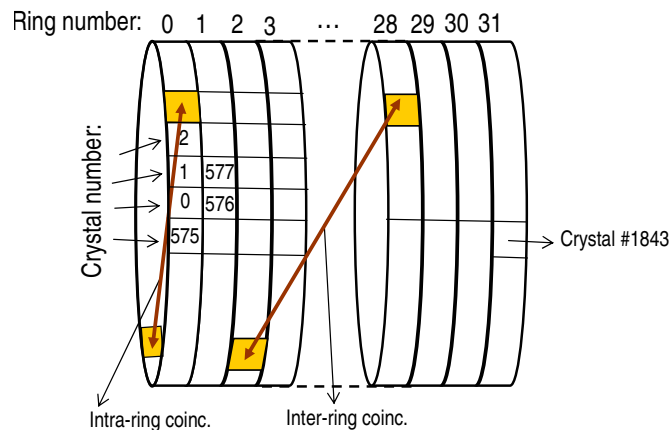


Figure A.1: Intra- and inter-ring coincidences and ring and pixel numbering adopted for the reconstruction routine. The image shows a closed ring detector geometry. If a dual head tomograph is considered pixels that should be absent are simply ignored.

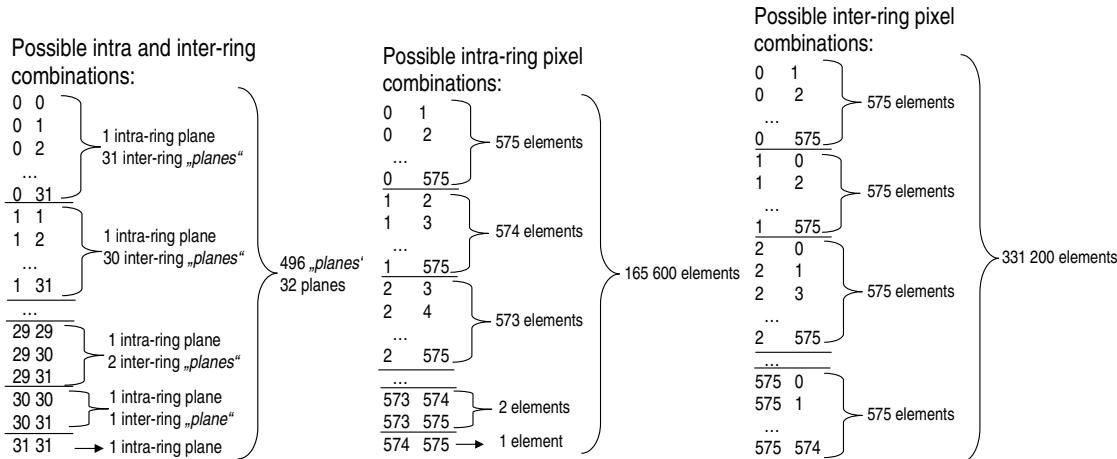


Figure A.2: Scheme showing possible intra-ring, inter-ring and pixel combinations.

coincidences, respectively, yielding a total number of coincidence possibilities of 169 574 400. In order to facilitate the histogramming of any given set of coincidences, measured or simulated, the asymmetry between intra-ring and inter-ring pixel combinations was broken by assuming a factorization scheme that considers inter-ring pixel combinations only. The asymmetry is again restored if during the factorization all pixels triggered in an intra-ring coincidence, and only those, are histogrammed taking into account the pixel with inferior number in first place. For example, if pixels 100 and 200 are hit in the same ring, than the histogram combination with pixels 200 and 100 must not exist since it regards the same coincidence channel, which is not true if two different rings are hit. The next paragraph exemplifies the C code that, respecting the constraints mentioned, generates a triangle-shaped histogram (Fig. A.2, left column) with a unique channel existing for every coincidence occurring in any given `rowA`, `ringA` and `rowB`, `ringB` of the tomograph, with `rowA` and `rowB` denoting the number of the pixel triggered within the ring (0 to 575, cf. Fig. A.1).

```
if (rowA > rowB && ringA == ringB) { // smaller pixel goes first
    aux = rowB, rowB = rowA, rowA = aux; }
```

```
// smaller ring goes first except for detections in same ring
if (ringA > ringB) { aux = rowB, rowB = rowA, rowA = aux;
    aux = ringB, ringB = ringA, ringA = aux; }
```

```
hitPlane= ringA * axialCH + ringB; // hit plane (axialCH=32 for exact-hr+)
chINpl = rowA * crPERri + rowB; // channel within plane (crPERri=576)
channel = hitPlane * chPERpl + chINpl;// unique channel number (chPERpl=331200)
```

In addition to the factorization algorithm described, dynamical allocation for new histogram channels appearing during the building of the histogram was implemented by means of a linked list scheme, where each histogram channel points to its immediately inferior, non-empty, non-adjacent channel and, at the same time, to its immediately superior, non-empty, non-adjacent channel. This allows the histogram to contain only non-empty channels and to grow only when a new, nonexisting channel is triggered. In order to save computer memory and increase the processing speed the histograms used during later iterations loose the linked list character since new histogram channels cannot appear during the iterations of the MLEM reconstruction algorithm. Finally, both the simulation and the reconstruction routines are versatile concerning the number of pixels considered, i.e. they are able to handle a larger number of pixels in the tomograph, e.g. by increasing the radius of the tomograph as studied in section 2.6.2.

Appendix B

CAGE - A Multi-Parameter Data Acquisition at CAMAC Speed

A data acquisition system performing multi parameter readout of electronic modules operating under the CAMAC¹ standard was developed in order to readout the two position sensitive γ -ray detectors studied in chapters 4, 5 and 6. Each detector provides 32 energy outputs resulting in 65 and 67 analog channels to be read if the additional coincidence time spectra are taken into account (chapters 4 and 5, and chapter 6, respectively). These numbers increase further if the extraction status from the accelerator is also sampled, as well as a scaler allowing to read the number of events lost by the system during data readout. Four CAMAC peak sensing ADC from Phillips Scientific, model PS7164, were used, each providing 16 channels input. A CAMAC/GPIB² crate controller from Kinetic Systems, model 3988, reads the ADC and sends the data through the GPIB protocol to a GPIB/Ethernet converter from National Instruments, model GPIB-ENET/100. The GPIB/Ethernet converter can be accessed by any linux-running machine logged to the local network. For that, a C/C++ based application named CAGE (Camac Acquisition through GPIB and Ethernet) was developed [Cre03]. It allows the user to control the CAMAC acquisition and to see, on-line, the spectra being collected. The GPIB/ENET driver software for linux is publicly available [Nat05] and the control routines for the display are based on the Qt open-source package [Tro05].

CAGE is prepared to automatically perform and display single spectrum acquisitions with rates above 40 kcps³ (Table B.1), two simultaneous spectra (Fig. B.1) reaching rates of approximately 30 kcps, 16 spectra, 64, 66 and 69 spectra. When acquiring 16 spectra or less, the 65 kiloword buffer of the crate controller, with 24-bit long words, is used to maximize speed throughput by reading one ADC in the so-called Q-repeat mode. In this mode, a CAMAC read function can be repeatedly executed at CAMAC-bus speed (~ 1 MHz, 24 bit, parallel) and the result is stored in the buffer only when the ADC delivers a CAMAC Q-signal, i.e. a valid read cycle. CAGE starts the connection protocol only when the buffer is full and, once the hand-shake between the host computer and the crate controller is performed, the full buffer is transferred in direct memory access (DMA) mode at the maximum speed of the intervening buses (8 Mbit, parallel, for the GPIB bus and 10 to 100 Mbit, serial, for the TCP/IP⁴).

If the number of spectra exceeds 16, than more than one ADC is needed and one repeated read function does not suffice. In this case, an auxiliary crate controller from Kinetic Systems, model 3982, is used which has two internal buffers: one for function storage and one for data, with 8 kiloword each. CAGE first stores in the 3982 function buffer the CAMAC operations to be performed every time an event arrives. An ADC from Ortec, model 811, with the slowest

¹ Computer Automated Measurement And Control.

² General Purpose Interface Bus.

³ Kilo counts per second.

⁴ Transmission Control Protocol / Internet Protocol.

conversion time, asserts its look-at-me (LAM) signal when it has finished conversion and with this starts the 3982 acquisition cycle. The 3982 runs in standalone mode, handling the arriving events and storing them in the data buffer at CAMAC speed. CAGE checks the data buffer and only reads it, in DMA mode as mentioned, after it is more than half-full, again optimizing the buses transfer capabilities.

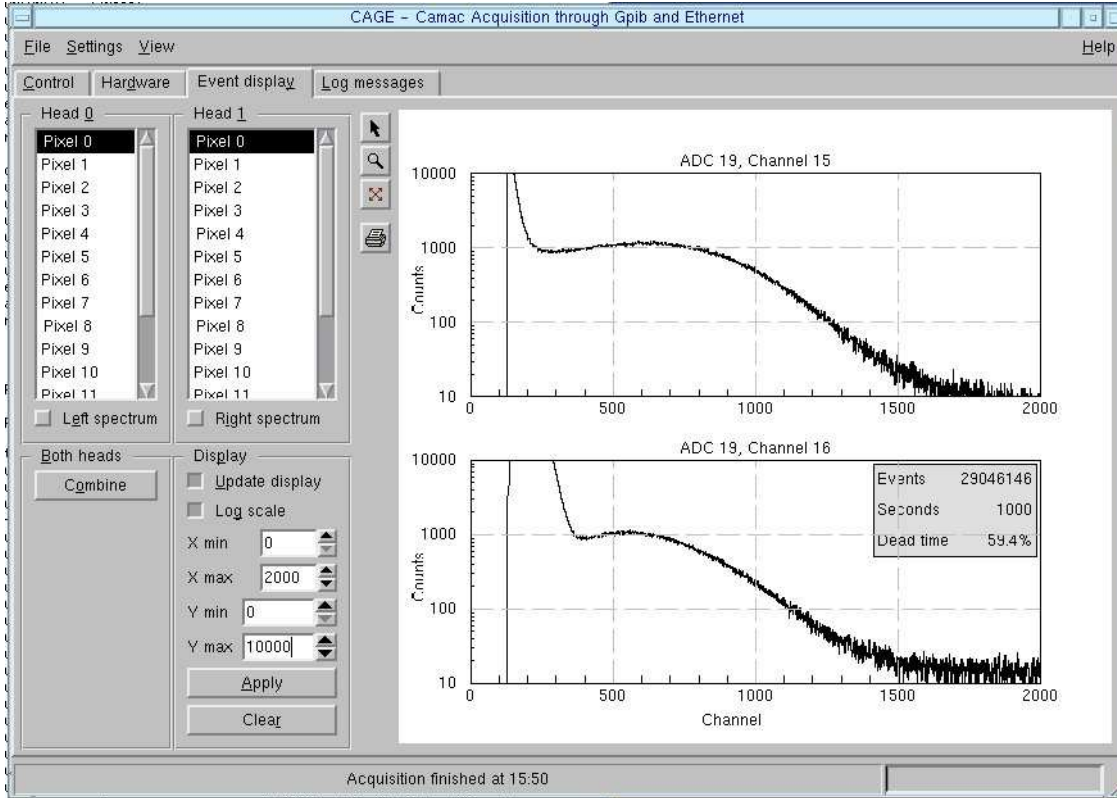


Figure B.1: CAGE user interface displaying two single photoelectron spectra. The spectra were simultaneously acquired with two Phillips PMT: an XP2020Q at -2650 V (top) and an XP3312B at -1300 V (bottom).

Table B.1: CAGE performance for several input rates and readout channels. All values obtained with a comb-shape spectrum generator.

In	Out											
	1 ch.		2 ch.		16 ch.		32 ch.		64 ch.		66 ch.	
Input rate (cps)	RR (cps)	DT (%)										
100	98.7	1.3	98.4	1.6	96	4	92	8	87	13	86	14
1 k	977	2.3	974	2.6	900	10	624	37	446	55	398	60
10 k	9 k	9.8	9.1 k	9.5	4.4 k	56	1.4 k	86	745	93	611	94
100 k	43 k	57	29 k	71	6 k	94	1.6 k	98.4	794	99.2	650	99.4

RR = Readout rate (counts per second), DT = Dead time (%).

Appendix C

Generated and Detected Positron Activity during Irradiation

The present appendix summarizes the method used to estimate the number of positron emitting nuclei detected within a given irradiation, e.g. as plotted in the simulation curve in Figs. 6.11 and 6.14, and detailed in Table 6.2 and Fig. 6.12. The number $N_0^{(j)}$ of each isotope species j produced by an incoming beam with fluence F and target range R was extrapolated from the output of the Monte-Carlo code PosGen [Has96, Pön04] shown in Fig. 1.17. The simulated value of $N_0^{(j)}$ must agree with that expected for thick targets

$$N_0^{(j)} = F \cdot \rho \cdot \frac{N_A}{A} \cdot R \cdot \sigma^{(j)}, \quad (\text{C.1})$$

with $\rho \cdot \frac{N_A}{A}$ being the target molecular density and $\sigma^{(j)}$ the partial cross section containing all the reactions yielding isotope j . The term $\sigma^{(j)}$ is given by

$$\sigma^{(j)} = \sum_i^M f_i \cdot \sigma_{PT_i}^{(j)}, \quad (\text{C.2})$$

with M the number of chemical elements composing the target, f_i the stoichiometric coefficient for element i in the target molecule and $\sigma_{PT_i}^{(j)}$ the partial cross section for the reactions $T_i(P, j)T_i'$ and $T_i(P, P')j$, i.e. the cross section for the reactions creating the projectile or target fragment j by impinging projectile P on target element T_i , respectively.

Eq. C.1 holds for a beam kinetic energy E between 500 down to 100 AMeV, where $\sigma^{(j)}$ is approximately constant [Sih93]. For smaller beam energies $\sigma^{(j)}$ depends on E and must be substituted with $\sigma^{(j)}(E)$, with $\sigma^{(j)}(E)$ presenting a first steep rise with decreasing E , followed by a sharp drop to zero for $E \leq 30$ AMeV [Has96, Sih93].

If the irradiation conditions used to build Table 6.2 are considered, i.e. a total of 6×10^{10} carbon ions are delivered onto a PMMA target with a kinetic energy of 200.2 AMeV, corresponding to $R = 74$ mm, together with e.g. $\sigma_{12\text{C}^{16}\text{O}}^{(15\text{O})} = 84$ mb taken from [Sih93], then the total number of ^{15}O target fragments produced following Eq. C.1 is 8.06×10^8 , which lies 12 % below the number simulated with the PosGen code (9.2×10^8 , Table 6.2) most probably because the Monte Carlo code takes into account the steep increase in the cross section for producing ^{15}O at low beam kinetic energy. The same is verified for the production of ^{11}C , both target and projectile, by considering $\sigma_{12\text{C}^{12}\text{C}}^{(11\text{C})} = 53$ mb [Sih93], $\sigma_{12\text{C}^{16}\text{O}}^{(11\text{C})} = 26.5$ mb [Sih93], and $\sigma_{12\text{C}^{1}\text{H}}^{(11\text{C})} = 57$ mb [Bee03]. In this case Eq. C.1 yields 3.7×10^9 ^{11}C ions versus a total of 4.0×10^9 generated with the PosGen code. This again is a good agreement due to the same argument: the Monte Carlo code must consider the higher cross sections verified when the beam energy decreases, therefore yielding 7.2 % more ^{11}C isotopes than the simpler approach given by Eq. C.1.

Once the number $N_0^{(j)}$ of isotopes j produced per spill is known, and assuming it is created at time instant $t_0 = 0$, the activity value at a later time instant t_1 , $A_{t_1}^{(j)}$, is given by

$$A_{t_1}^{(j)} = \frac{N_0^{(j)}}{T_{1/2}^{(j)} / \ln 2} \cdot \sum_{i=0}^{N_s-1} \exp\left(\frac{-i \cdot T_M}{T_{1/2}^{(j)} / \ln 2}\right), \quad (\text{C.3})$$

with N_s the number of spills delivered between t_0 and t_1 , T_M the macropulse (spill) period and $T_{1/2}^{(j)}$ the half-life of isotope j . The number of isotopes j decaying within the time window $(t_0 = 0, t_1)$ of a PET measurement, $C^{(j)} = N^{(j)}(t_0 = 0, t_1)$, is given by the time integral of Eq. C.3:

$$C^{(j)} = N^{(j)}(t_0 = 0, t_1) = \int_{t_0}^{t_1} A^{(j)}(t) dt = N_0^{(j)} \cdot \sum_{i=0}^{N_s-1} \left[1 - \exp\left(\frac{-i \cdot T_M}{T_{1/2}^{(j)} / \ln 2}\right) \right]. \quad (\text{C.4})$$

Eq. C.4 shows that isotopes with half-lives $T_{1/2}^{(j)}$ much shorter than T_M yield

$$C_{short-lived}^{(j)'} = A_0^{(j)} \cdot \frac{T_{1/2}^{(j)}}{\ln 2} \cdot N_s, \quad (\text{C.5})$$

i.e. the induced activity nearly completely decays within any PET measurement. This mechanism explains the increasing relative weight of short-lived, β^+ -decaying isotopes, e.g. ^{12}N and ^8B , with decreasing measuring time. Due to their fast decay, this fact can only be observed when data taking during particle extraction is implemented (Table 6.2 and Fig. 6.12). By weighting Eq. C.5 with the proper time window for data taking during particle extraction, the number of short-lived isotopes detected slightly reduces to

$$C_{short-lived}^{(j)} = A_0^{(j)} \cdot \frac{T_{1/2}^{(j)}}{\ln 2} \cdot N_s \cdot \left[\frac{\Delta t_{bg}}{T_{RF}} - 1 \right], \quad (\text{C.6})$$

with Δt_{bg} and T_{RF} defined in Fig. 6.1 and Eq. 6.2, respectively.

If the same time window is applied for isotopes with $T_{1/2}^{(j)} > T_M$, and adding the proper weight resulting from the duty factor D_f of the accelerator, defined in section 6.1, the number of long-lived isotopes detected is given by

$$C_{long-lived}^{(j)} = C^{(j)} \cdot \left[1 - D_f \right] + C^{(j)} \cdot D_f \cdot \left[\frac{\Delta t_{bg}}{T_{RF}} - 1 \right] = C^{(j)} \cdot \left[1 + D_f \cdot \left(\frac{\Delta t_{bg}}{T_{RF}} - 2 \right) \right]. \quad (\text{C.7})$$

Finally, both $C_{long-lived}^{(j)}$ and $C_{short-lived}^{(j)}$ must be multiplied by the geometrical acceptance and coincidence detection efficiency of the detectors measuring the decaying β^+ -activity.

Appendix D

A Random Suppression Solution for BASTEI

The results obtained with the phase trigger described in section 6.2.2 allowed to perform random suppression during particle extraction with the two LSO/APDA detectors (section 6.5). The phase trigger utilized [Hei04] showed excellent performance for a fixed beam energy, being independent from the amplitude of the RF signal, as necessary for all results presented in sections 6.5, 6.7 and 6.8.2. Nevertheless, its digital output presents frequency dependent delays, described in section 6.2.2, which veto its application during the consecutive changing beam energies utilized during therapeutic irradiation by means of the GSI rasterscan beam delivery [Hab93]. For this reason, the experimental results obtained with a phase trigger independent of the amplitude, frequency and baseline oscillations of its input signal are presented here. The proposed phase trigger [Eng05c] is based on a leading edge circuit, preceded by a high-pass passive filter and built in zero-crossing mode (Fig D.1). Its performance is shown in Fig. D.2, obtained by feeding into an assembled phase-trigger several signals from a waveform generator. The timings of the input signals covered the range of frequencies used at the GSI rasterscan delivery system, as well as the timings to be used at the synchrotron in the Heidelberg clinics (Table 6.6). It can be seen that a negligible oscillation (inferior to 2 %) exists between the output of the phase trigger in respect to the moment of zero-crossing of all input signals. The input frequencies covered the accelerator RF timings from the GSI facility as well as from the hospital facility planned in Heidelberg. Input frequencies ranged between 2.08 MHz (Fig. D.2, top) up to 7.1 MHz (Fig. D.2, bottom), with the signal amplitudes varying between 0.5 and 2 V in all cases, which is well above the 30 % maximum amplitude variation of the RF signal at GSI [For03]. In addition to the tests described, a low frequency signal (not shown), simulating an oscillating baseline, was added to the input of the phase-trigger and it

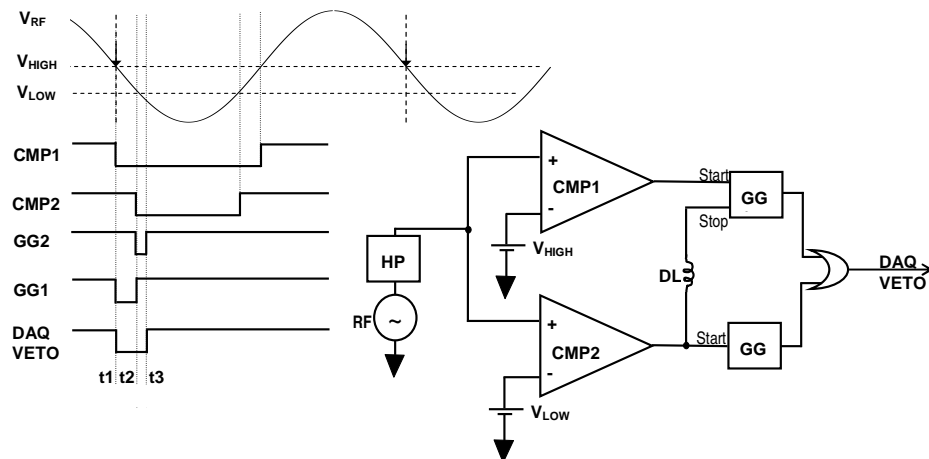


Figure D.1: Timing diagram (left) of a zero-crossing, phase trigger concept (right). The high-pass filter HP brings the DC component of the RF signal to zero, i.e. it eliminates slow moving baseline oscillations. By setting V_{HIGH} to ground the remaining electronics acts like a zero-crossing detector insensitive to amplitude and frequency variations of the input signal (cf. Fig. D.2).

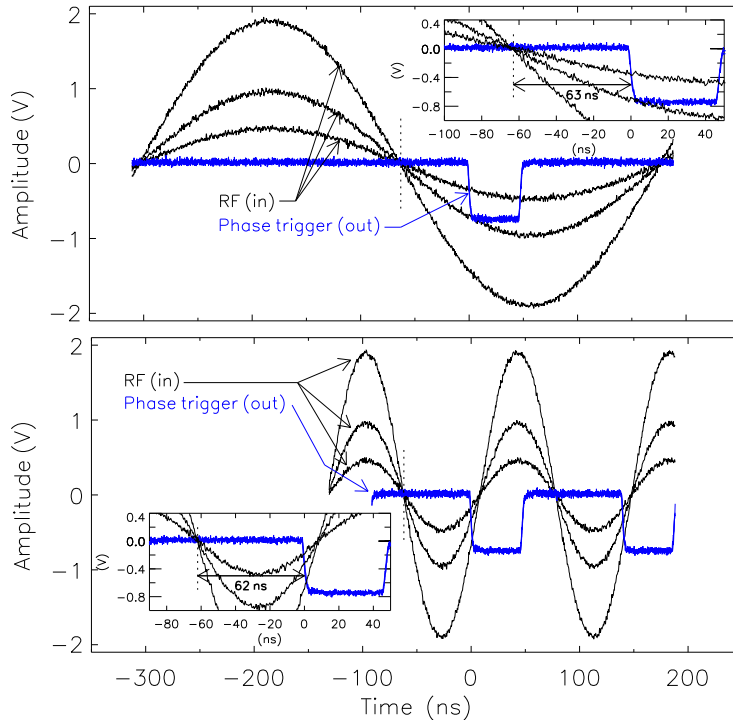


Figure D.2: Results measured with the phase trigger proposed. The three output signals in each image overlap perfectly (text has details).

was seen that a simple passive, double stage, high-pass filter (HP in Fig. D.1) provided enough attenuation of the slow oscillations, enabling the phase-trigger to perform without restrictions.

The output of the phase trigger, DAQ VETO, can be implemented onto the electronics of BASTEI following the scheme in Fig. D.3. An analog multiplexer sets the connection from the anode signal of each PMT to ground (through a $50\ \Omega$ resistor) only when the DAQ VETO signal is asserted. This disables the data acquisition from BASTEI to read the high yield event background during the microbunches (Δt_{bg} , Fig. 6.1). This setup still lacks a time correction for the ion transit time in the beam pipeline, which is a parameter dependent on the beam energy that can be calibrated once and written on an electronic look-up table. Together with this look-up table, the whole assembly would provide a low-cost random suppression solution for BASTEI based on one phase-trigger circuit, already assembled at FZR, together with 256 (or 64 Quad) fast analog multiplexers installed between the anode outputs of the 256 PMT and the electronics boards from BASTEI, as shown in Fig. D.3.

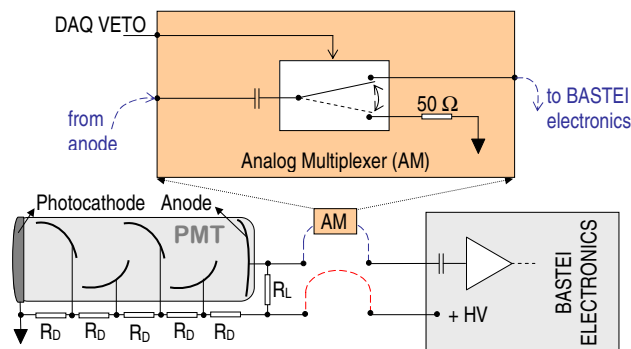


Figure D.3: Implementation of the phase trigger output onto BASTEI. The dashed, curved lines denote the two cables connecting the data acquisition electronics from BASTEI to each PMT.

Bibliography

- [Ada01] L.E. Adam, J.S. Karp, M.E. Daube-Witherspoon, R.J. Smith. Performance of a whole-body PET scanner using curve-plate NaI(Tl) detectors. *J. Nucl. Med.*, 42:1821–1830, 2001.
- [Ahl80] S.P. Ahlen. Theoretical and experimental aspects of the energy loss of relativistic heavily ionizing particles. *Rev. Mod. Phys.*, 52:121–173, 1980.
- [Alk56] D.G. Alkhazov, D.S. Andreyev, A.P. Greenberg, I.N. Lemberg. Investigation of Coulomb excitation of nuclei by nitrogen ions. *Nucl. Phys.*, 2(1):65–80, 1956.
- [Ama04] U. Amaldi, P. Berra, K. Crandall, D. Toet, M. Weiss, R. Zennaro, E. Rosso, B. Szless, M. Vretenar, C. Cicardi, C. De Martinis, D. Giove, D. Davino, M. R. Masullo, V. Vaccaro. LIBO - a linac-booster for proton therapy: construction and tests of a prototype. *Nucl. Instrum. Meth. A*, 521:512–529, 2004.
- [Ang58] H.O. Anger. Scintillation camera. *Rev. Sci. Instrum.*, 29:27–33, 1958.
- [Bad96] R.D. Badawi, P.K. Marsden, B.F. Cronin, J.L. Sutcliffe, M.N. Maisey. Optimization of noise-equivalent count-rates in 3D PET. *Phys. Med. Biol.*, 41:1755–1776, 1996.
- [Bad97] E. Badura, H. Eickhoff, H. Essel, Th. Haberer, J. Hoffmann, U. Krause, W. Ott, K. Poppensieker, M. Richter, D. Schardt, R. Steiner, B. Voss. Safety and control system for the GSI therapy project. In *ICALEPCS97*, pages 555–558, Beijing, November 1997.
- [Bar56] W.H. Barkas, W. Birnbaum, F.M. Smith. Mass-ratio method applied to the measurement of L-meson masses and the energy balance in pion decay. *Phys. Rev.*, 101(2):778–795, 1956.
- [Bee03] J. Beebe-Wang, P. Vaska, F.A. Dilmanian, S.G. Peggs, D.J. Schlyer. Simulation of proton therapy treatment verification via PET imaging of induced positron-emitters. In *Proc. IEEE 2003 Med. Ima. Conf.*, Portland, OR, USA, Oct. 2003. M8-6.
- [Ber01] E. Berdermann, K. Blasche, P. Moritz, H. Stelzer, B. Voss. The use of CVD-diamond for heavy-ion detection. *Diam. Relat. Mater.*, 10:1770–1777, 2001.
- [Bir64] J.B. Birks. *The Theory and Practice of Scintillation Counting*. Pergamon Press, London, 1964.
- [Bob84] G.J. Bobbink, A. Engler, R.W. Kraemer, J. Nash, R.B. Sutton. Study of radiation damage to long BGO crystals. *Nucl. Instrum. Meth. A*, 227:470–477, 1984.
- [Boe03] R. Boellaard, F. Buijs, H.W.A.M. de Jong, M. Lenox, T. Gremillion, A.A. Lammermsma. Characterization of a single LSO crystal layer High Resolution Research Tomograph. *Phys. Med. Biol.*, 48:429–448, 2003.
- [Boh15] N. Bohr. The penetration of atomic particles through matter. *Philos. Mag.*, 30:581, 1915.

- [Bou00] P. Bourgeois, M. Karolak, G. Vasseur. Performance of the photomultiplier tubes used in the DIRC of BABAR: effect of a magnetic field and of helium. *Nucl. Instrum. Meth. A*, 442:105–112, 2000.
- [Bra99] S. Brandenburg, L. de Vries. A subharmonic buncher for the AGOR-cyclotron. In E. Baron and M. Lieuvin, editors, *Cyclotrons and Their Applications 1998: XV International Conference*, pages 193–195, Caen, France, 1999. IoP Publishing, Bristol.
- [Bra03] A. Brahme. Biologically optimized 3-dimensional in vivo predictive assay-based radiation therapy using positron emission tomography-computerized tomography imaging. *Acta Oncol.*, 42(2):123–136, April 2003.
- [Bre56] G. Breit, M.E. Ebel. Nucleon transfer and virtual coulomb excitation. *Phys. Rev.*, 104(4):1030–1046, 1956.
- [Bro76] R.A. Brooks and G. DiChiro. Principles of computer assisted tomography (CAT) in radiographic and radioisotopic imaging. *Phys. Med. Biol.*, 21(5):689–732, 1976.
- [Buc96] D. Bucin, M. Conte, O. Ferrando, A. Ratti, V. Tamburini. Conventional proton synchrotron. In U. Amaldi, M. Grandolfo, and L. Picardi, editors, *The RITA Network and the Design of Compact Proton Accelerators*. INFN-LNF Divisione Ricerca, Frascati, 1996.
- [Buh03] P. Buhzan, B. Dolgoshein, L. Filatov, A. Ilyin, V. Kantzerov, V. Kaplin, A. Karakash, F. Kayumov, S. Klemin, E. Popova, S. Smirnov. Silicon photomultiplier and its possible applications. *Nucl. Instrum. Meth. A*, 504:48–52, 2003.
- [Cas86] M.E. Casey, R. Nutt. A multicrystal two dimensional BGO detector for positron emission tomography. *IEEE T. Nucl. Sci.*, 33:460–463, 1986.
- [Cha98] Y. Charon, P. Lanière, H. Tricoire. Radio-imaging for quantitative autoradiography in biology. *Nucl. Med. Biol.*, 25:699–704, 1998.
- [Che83] V.Yu. Chepel. A new liquid xenon scintillation detector for positron emission tomography. *Nucl. Tracks Radiat. Meas.*, 21(1):47–51, 1983.
- [Che04a] V. Chepel, F. Neves, V. Solovov, A. Pereira, M.I. Lopes, J. Pinto da Cunha, P. Mendes, A. Lindote, C.P. Silva, R. Ferreira Marques, A.J.P.L. Policarpo. Performance of a chamber for studying the liquid xenon response to nuclear recoils. In *Proc. IEEE 2004 Nucl. Sci. Symp.*, Rome, Italy, Oct. 2004. N16-28.
- [Che04b] S.R. Cherry. *In vivo* molecular genomic imaging: new challenges for imaging physics. *Phys. Med. Biol.*, 49:13–48, 2004.
- [Chu99] W.T. Chu. Hadron therapy. In W.R. Hendee, editor, *Biomedical Uses of Radiation*, pages 1055–1131. Wiley-VCH Publishers, New York, April 1999.
- [Cir04] G.A.P. Cirrone, Laboratori Nazionali del Sud - INFN, Catania, November 2004. Personal communication.
- [Col00] J. Collot, S. Jan, E. Tournefier. A liquid xenon PET camera for neuro-science. In B. Aubert and J. Colas, editors, *CALOR2000 Proc. 9th Int. Conf. on Calorimetry in High Energy Physics*, pages 305–313. Frascati Phys. Ser., 2000.

- [Con03] M. Conti, B. Bendriem, M. Casey, M. Chen, F. Kehren, C. Michel, V. Panin. Implementation of time-of-flight on CPS HiRez PET scanner. In *Proc. IEEE 2003 Med. Ima. Conf.*, Portland, OR, USA, Oct. 2003. M3-1.
- [Coo99] D.W. Cooke, B.L. Benneth, R.E. Muenchausen, K.J. McClellan, J.M. Roper, M.T. Whittaker. Intrinsic trapping sites in rare-earth and yttrium oxyorthosilicates. *J. Appl. Phys.*, 86(9):5308–5310, 1999.
- [Coo00] D.W. Cooke, K.J. McClellan, B.L. Bennett, J.M. Roper, M.T. Whittaker, R.E. Muenchausen, R.C Sze. Crystal growth and optical characterization of cerium-doped $\text{Lu}_{1.8}\text{Y}_{0.2}\text{SiO}_5$. *J. Appl. Phys.*, 88(12):7360–7362, 2000.
- [Cou04] G. Coutrakon, J. Hubbard, J. Johanning, G. Maudsley, T. Slaton, P. Morton. A performance study of the Loma Linda proton medical accelerator. *Med. Phys.*, 21(11):1691–1701, 2004.
- [Cre98] P. Crespo, V. Chepel, M.I. Lopes, L. Janeiro, R. Ferreira Marques, A.J.P.L. Policarpo. Pulse shape analysis in the liquid xenon multiwire ionisation chamber for PET. *IEEE T. Nucl. Sci.*, 45(3):561–567, 1998.
- [Cre00] P. Crespo, J. van der Marel, V. Chepel, M.I. Lopes, D. Santos, L. Janeiro, V. Solovov, R.F. Marques, A.J.P.L. Policarpo. Pulse processing for the PET multiwire liquid xenon ionisation chamber. *IEEE T. Nucl. Sci.*, 47(6):2119–2126, 2000.
- [Cre02] P. Crespo, K. Lauckner, W. Enghardt. A new fully 3D maximum likelihood PET reconstruction applicable to different detector arrangements. *GSI Rep. 2002-1 (Ann. Rep. 2001)*, pages 173–174, 2002.
- [Cre03] P. Crespo, J. Pawelke, W. Enghardt. A CAMAC data acquisition system for multi parameter measurements. *Wiss.-Tech. Ber. FZR-372 (Ann. Rep. 2002)*, page 82, 2003.
- [Cre04] P. Crespo, M. Kapusta, J. Pawelke, M. Moszyński, W. Enghardt. First in-beam PET imaging with LSO/APD-array detectors. *IEEE T. Nucl. Sci.*, 51(5):2654–2661, 2004.
- [Cre05a] P. Crespo, G. Shakirin, W. Enghardt. Direct time-of-flight for online, in-beam PET: concept and feasibility study. *Phys. Med. Biol.*, 2005. To be submitted.
- [Cre05b] P. Crespo, G. Shakirin, W. Enghardt. On the detector arrangement for in-beam PET for hadron therapy monitoring. *Phys. Med. Biol.*, 2005. Submitted.
- [Cre05c] P. Crespo, N. Abolmaali, R. Bergmann, E. Will, W. Enghardt. Low-activity PET measurements with LSO- and BGO-based positron tomographs. *Phys. Med. Biol.*, 2005. To be submitted.
- [Cre05d] P. Crespo, T. Barthel, H. Frais-Kölbl, E. Griesmayer, K. Heidel, K. Parodi, J. Pawelke, W. Enghardt. Suppression of random coincidences during in-beam PET measurements at ion beam radiotherapy facilities. *IEEE T. Nucl. Sci.*, 52(5):980–987, 2005.
- [Cry00] The Crystal Clear Collaboration. Crystal data. <http://crystalclear.web.cern.ch/>, available Jun. 2005. Last update: Dec. 2000.
- [Dat97] C.P. Datema, I.P. Pleasents, D. Ramsden. Hybrid photodiodes in scintillation counter applications. *Nucl. Instrum. Meth. A*, 387:100–103, 1997.

- [Deb00] J. Debus, Th. Haberer, D. Schulz-Ertner, O. Jäkel, F. Wenz, W. Enghardt, W. Schlegel, G. Kraft, M. Wannemacher. Bestrahlung von Schädelbasistumoren mit Kohlenstoffionen bei der GSI. *Strahlenther. Onkol.*, 176(5):211–216, 2000.
- [Dei00] K. Deiters, Y. Musienko, S. Nicol, B. Patel, D. Renker, S. Reucroft, R. Rusack, T. Sakhelashvili, J. Swain, P. Vikas. Properties of the most recent avalanche photodiodes for the CMS electromagnetic calorimeter. *Nucl. Instrum. Meth. A*, 442:193–197, 2000.
- [Der82] S.E. Derenzo, T.F. Budinger, R.H. Huesman, J.L. Cahoon. Dynamic positron emission tomography in man using small bismuth germanate crystals. In *Proc. of the Sixth Int. Conf. on Positron Annihilation*, pages 1–11, Fort Worth, TA, April 1982.
- [dG94] T.R. de Grado, T.G. Turkington, J.J. Williams, C.W. Stearns, J.M. Hoffman, R.E. Coleman. Performance characteristics of a whole-body PET scanner. *J. Nucl. Med.*, 35:1398–1406, 1994.
- [Dol00] A. Dolinskii, H. Eickhoff, B. Franczak. The synchrotron of the dedicated ion beam facility for cancer therapy, proposed for the clinic in Heidelberg. In *Proceedings of the 2000 Particle Accelerator Conf.*, pages 2509–2511, Vienna, Austria, 2000.
- [Eic03] H. Eickhoff, R. Bär, A. Dolinskii, Th. Haberer, B. Schlitt, P. Spiller, U. Weinrich. HICAT - the German hospital-based light ion cancer therapy project. In *Proceedings of the 2003 Particle Accelerator Conf.*, pages 694–698, Portland, OR, USA, 2003.
- [Eng92] W. Enghardt, W.D. Fromm, H. Geissel, H. Keller, G. Kraft, A. Magel, P. Manfraß, G. Münzenberg, F. Nickel, J. Pawelke, D. Schardt, C. Scheidenberger, M. Sobiella. The spatial distribution of positron-emitting nuclei generated by relativistic light-ion beams in organic matter. *Phys. Med. Biol.*, (11):2127–2131, 1992.
- [Eng00] W. Enghardt, R. Hinz, K. Lauckner, J. Pawelke, F. Pönisch, B.G. Hasch. In-situ positron emission tomography for dose localisation at the tumour therapy with ^{12}C . *GSI Rep. 2000-1 (Ann. Rep. 1999)*, pages 164–165, 2000.
- [Eng03] W. Enghardt, P. Crespo, W. Bourgeois, A. Winter. A technical feasibility study for a PET therapy monitor combined with a rotating ion beam delivery. *Wiss.-Tech. Ber. FZR-372 (Ann. Rep. 2002)*, pages 83–84, 2003.
- [Eng04a] W. Enghardt, K. Parodi, P. Crespo, F. Fiedler, J. Pawelke, F. Pönisch. Dose quantification from in-beam positron emission tomography. *Radiother. Oncol.*, 73(2):96–98, 2004.
- [Eng04b] W. Enghardt, P. Crespo, F. Fiedler, R. Hinz, K. Parodi, J. Pawelke, F. Pönisch. Charged hadron tumour therapy monitoring by means of PET. *Nucl. Instrum. Meth. A*, 525:284–288, 2004.
- [Eng05a] W. Enghardt. Positronen-Emissions-Tomographie für die Qualitätssicherung der Ionenstrahl-Therapie von Tumoren, Habilitationsschrift, Dresden University of Technology, Dresden, 2005.
- [Eng05b] W. Enghardt, H. Müller. In-beam PET at high-energy photon beams: a feasibility study. *Phys. Med. Biol.*, 2005. Submitted.

- [Eng05c] W. Enghardt, P. Crespo, K. Parodi, J. Pawelke. Verfahren zur Korrektur der beim Monitoring der strahlentherapeutischen Behandlung mittels in-beam PET erhaltenen Messwerte. *Deutsches Patent- und Markenamt München*, (DE 10 2004 009 784 A1), Sept. 2005.
- [Fie03] C. Field, T. Hadig, M. Jain, D.W.G.S. Leith, G. Mazaheri, B.N. Ratcliff, J. Schwiening, J. Va'vra. Timing and detection efficiency properties of multi-anode PMTs for a focusing DIRC. In *Proc. IEEE 2003 Nucl. Sci. Symp.*, Portland, OR, USA, Oct. 2003. N38-8.
- [Fie05] F. Fiedler, P. Crespo, K. Parodi, M. Sellesk, W. Enghardt. The feasibility of in-beam PET for therapeutic beams of ^3He . In *IEEE 2005 Nucl. Sci. Symp.*, Puerto Rico, Oct. 2005. Accepted.
- [Fir96] R.B. Firestone and V.S. Shirley, editor. *Table of Isotopes*. John Wiley & Sons, Inc., New York, 8th edition, 1996.
- [For03] P. Forck, GSI Darmstadt, December 2003. Personal communication.
- [Fra04] H. Fraiss-Kölbl, E. Griesmayer, H. Kagan, H. Pernegger. A fast low-noise charged-particle CVD diamond detector. *IEEE T. Nucl. Sci.*, 51(6):3833–3837, 2004.
- [Fur03] T. Furukawa, K. Noda, E. Urakabe, M. Muramatsu, M. Kanazawa, K. Maeda. Characteristics of fast beam switching for spot scanning. *Nucl. Instrum. Meth. A*, 503:485–495, 2003.
- [Gar00] N. Garnier, C. Dujardin, A.N.C. Belsky, J.P. Moy, H. Wieckzorek, P. Chevallier, A. Firsov. Spectroscopy of CsI(Tl). In *SCINT99 Proc. of the 5th Int. Conf. on Inorganic Scintillators and their Applications*, pages 379–384, M. V. Lomonosov State University, Moscow, 2000.
- [Glo04] J. Glodo, W.W. Moses, W.M. Higgins, E.V.D. van Loef, P. Wong, S.E. Derenzo, M.J. Weber, K.S. Shah. Effects of Ce concentration on scintillation properties of $\text{LaBr}_3:\text{Ce}$. In *Proc. IEEE 2004 Nucl. Sci. Symp.*, Rome, Italy, Oct. 2004. N19-5.
- [Got93] B. Gottschalk, A.M. Koehler, R.J. Schneider, J.M. Sisterson, M.S. Wagner. Multiple Coulomb scattering of 160 MeV protons. *Nucl. Instrum. Meth. B*, 74:467–490, 1993.
- [Gro98a] D.E. Groom. Particle detectors. *The European Physical Journal C*, 3(1-4):154–162, 1998.
- [Gro98b] D.E. Groom. Photon and electron interactions with matter. *The European Physical Journal C*, 3(1-4):152–153, 1998.
- [GSI99a] Proposal for a dedicated ion beam facility for cancer therapy. *GSI Nachrichten*, 1:14–16, 1999.
- [GSI99b] Tumour therapy, first results from the clinical study. *GSI-Nachrichten*, 3:8, 1999.
- [Gun04a] K. Gunzert-Marx. *Nachweis leichter Fragmente aus Schwerionenreaktionen mit einem BaF_2 -Teleskop-Detektor*. PhD thesis, Darmstadt University of Technology, Darmstadt, Feb. 2004.
- [Gun04b] K. Gunzert-Marx, D. Schardt, R.S. Simon. Fast neutrons produced by nuclear fragmentation in treatment irradiations with ^{12}C beam. *Radiat. Prot. Dosim.*, 110(1-4):595–600, 2004.

- [Hab93] Th. Haberer, W. Becher, D. Schardt, G. Kraft. Magnetic scanning system for heavy ion therapy. *Nucl. Instrum. Meth. A*, 330:296–305, 1993.
- [Hab01] Th. Haberer, H. Eickhoff, P. Spiller, GSI Darmstadt, 2001. Personal communication.
- [Hag02] K. Hagiwara et al. Review of Particle Physics. *Phys. Rev. D*, 66:010001+, 2002. <http://pdg.lbl.gov>, available Jun. 2005.
- [Hal94] E.J. Hall. *Radiobiology for the radiobiologist*. J.B. Lippincott Company, Philadelphia, 4th edition, 1994.
- [Has96] B.G. Hasch. *Die physikalischen Grundlagen einer Verifikation des Bestrahlungsplanes in der Schwerionen-Tumorthherapie mit der Positronen-Emissions-Tomographie*. PhD thesis, Dresden University of Technology, Dresden, Dec. 1996.
- [Hea98] The Heavy Ion Collaboration. *Proposal for a dedicated ion beam facility for cancer therapy*. K.D. Groß, M. Pavlovic, editors, GSI Darmstadt, 1998.
- [Hei04] K. Heidel. Ableitung eines VETO-Signals aus der Beschleuniger HF an der GSI, FZ-Rossendorf, March 2004. Internal communication.
- [Hel00] E. Hell, W. Knüpfer, D. Mattern. The evolution of scintillating medical detectors. *Nucl. Instrum. Meth. A*, 454:40–48, 2000.
- [Hig75] V.L. Highland. Some practical remarks on multiple scattering. *Nucl. Instrum. Meth.*, 129:497, 1975.
- [Hig79] V.L. Highland. Some practical remarks on multiple scattering. *Nucl. Instrum. Meth.*, 161:171, 1979.
- [Hir92] K. Hiramoto, M. Nishi. Resonant beam extraction scheme with constant separatrix. *Nucl. Instrum. Meth. A*, 322:154–160, 1992.
- [Hof48] R. Hofstadter. Alkali halide scintillator counters. *Phys. Rev.*, 74:100–101, 1948.
- [Hof00] S. Hofmann, G. Münzenberg. The discovery of the heaviest elements. *Rev. Mod. Phys.*, 72(3):733–767, July 2000.
- [Hub02] J.S. Huber, W.W. Moses, W.F. Jones, C.C. Watson. Effect of ^{176}Lu on singles transmission for LSO-based PET cameras. *Phys. Med. Biol.*, 47:3535–3541, 2002.
- [Hug79] W.L. Hughes, G.H. Nussbaum, R. Connolly, B. Emami, P. Reilly. Tissue perfusion rate determined from the decay of oxygen-15 after photon activation in situ. *Science*, 204:1215–1217, 1979.
- [Huh93] M. Huhtinen, P.A. Aarnio. Pion induced displacement damage in silicon devices. *Nucl. Instrum. Meth. A*, 335:580–582, 1993.
- [Hum03] J.L. Humm, A. Rosenfeld, A. Del Guerra. From PET detectors to PET scanners. *Eur. J. Nucl. Med. Mol. I.*, 30:1574–1597, 2003.
- [ICR70] *Linear energy transfer*. ICRU Report No. 16, Washington, 1970.
- [ICR84] *Stopping powers for electrons and positrons*. ICRU Report No. 37, Washington, 1984.
- [ICR93] *Stopping powers and ranges for protons and alpha particles*. ICRU Report No. 49, Washington, 1993.

- [Iva98] D.Yu. Ivanov, E.A. Kuraev, A. Schiller, V.G. Serbo. Production of e^+e^- pairs to all orders in $Z\alpha$ for collisions of high-energy muons with heavy nuclei. *Phys. Lett. B*, 442:453–458, 1998.
- [Jäk00] O. Jäkel, J. Debus. Selection of beam angles for radiotherapy of skull base tumours using charged particles. *Phys. Med. Biol.*, 45:1229–1241, 2000.
- [Jäk01] O. Jäkel, M. Krämer, C.P. Karger, J. Debus. Treatment planning for heavy ion radiotherapy: clinical implementation and application. *Phys. Med. Biol.*, 46:1101–1116, 2001.
- [Jäk02] O. Jäkel. Bestrahlungsplanung für die Schwerionentherapie. In *Berichte aus der Medizinischen Physik*. Shaker Verlag GmbH, Aachen, 2002. ISBN 3-8322-0350-8.
- [Jan02] S. Janek. 3-dimensional patient dose delivery verification based on PET-CT imaging of photonuclear reactions in 50 MV scanned photon beams, Master thesis, Karolinska Institute and Royal Institute of Technology, Stockholm, 2002.
- [Joy74] A.R. Joy. A standard system of coordinates for radiotherapy apparatus. *Phys. Med. Biol.*, 19:213–219, 1974.
- [Kap00] M. Kapusta, M. Moszyński, M. Balcerzyk, J. Pawelke. Comparison of the scintillation properties of LSO:Ce and YSO:Ce as the detectors for high resolution PET. *Acta Phys. Pol. B*, 31(1):101–106, 2000.
- [Kap02] M. Kapusta, P. Crespo, M. Moszyński, W. Enghardt, M. Szawlowski, B.L. Zhou, D. Wolski. Evaluation of LAAPD arrays for high-resolution scintillator matrices readout. *IEEE T. Nucl. Sci.*, 44(4):1693–1698, 2002.
- [Kap03] M. Kapusta, P. Crespo, D. Wolski, M. Moszyński, W. Enghardt. Hamamatsu S8550 APD arrays for high-resolution scintillator matrices readout. *Nucl. Instrum. Meth. A*, 504:139–142, 2003.
- [Kap04] M. Kapusta, P. Crespo, D. Wolski, K. Heidel, L. Heinrich, J. Hutsch, J. Pawelke, M. Sobiella, A. Trzcińska, M. Moszyński, W. Enghardt. The LSO/APD array as a possible detector for in-beam PET in hadron therapy. *IEEE T. Nucl. Sci.*, 51(4):1389–1394, 2004.
- [Kar03] C.P. Karger, D. Schulz-Ertner, B.H. Diding, J. Debus, O. Jäkel. Influence of setup errors on spinal cord dose and treatment plan quality for cervical spine tumors: a phantom study for photon IMRT and heavy charged particle radiotherapy. *Phys. Med. Biol.*, 48:3171–3189, 2003.
- [Kau61] R. Kaufmann, R. Wolfgang. Nucleon transfer reactions in grazing collisions of heavy ions. *Phys. Rev.*, 121(1):192–205, 1961.
- [Kau02] C. Kausch, W. Enghardt. The evaluation of carbon ion therapy PET data within the time domain. *Wiss.-Tech. Ber. FZR-341 (Ann. Rep. 2001)*, page 102, 2002.
- [Kim01] J. Kim, F. Marti, H. Blosser. Design study of a superconducting cyclotron for heavy ion therapy. In F. Marti, editor, *Cyclotrons and Their Applications 2001: XVI International Conference*, pages 324–326, East Lansing, MI, USA, 2001. AIP Conference Proceedings, New York.

- [Kim02] T. Kimble, M. Chou, B.H.T. Chai. Scintillation properties of LYSO crystals. In *Proc. IEEE 2002 Med. Ima. Conf.*, Norfolk, VI, USA, Nov. 2002. M10-34.
- [Kno89] G.F. Knoll. *Radiation Detection and Measurement*. John Wiley & Sons, New York, 2nd edition, 1989.
- [Kob83] M. Kobayashi, K. Kondo, H. Hirabayashi, S.-I. Kurokawa, M. Taino, A. Yamamoto. Radiation damage of BGO crystals due to low energy γ rays, high energy protons and fast neutrons. *Nucl. Instrum. Meth.*, 206:107–117, 1983.
- [Kop04] U. Kopf, P. Heeg, P. Emde. The gantry irradiation room at the Heidelberg irradiation facility. *GSI Rep. 2004-1 (Ann. Rep. 2003)*, page 183, 2004.
- [Kra90] G. Kraft. Radiobiological and physical basis for radiotherapy with protons and heavier ions. *Strahlenther. Onkol.*, 166:10, 1990.
- [Kra99] G. Kraft, M. Scholz, U. Bechthold. Tumor therapy and track structure. *Radiat. Environ. Biophys.*, 38(4):229–237, 1999.
- [Kra00] G. Kraft. Tumor therapy with heavy charged particles. *Prog. Part. Nucl. Phys.*, 45:473–544, 2000.
- [Krä94] M. Krämer, G. Kraft. Calculations of heavy ion track structure. *Radiat. Environ. Bioph.*, 33(2):91–109, 1994.
- [Krä00] M. Krämer, O. Jäkel, T. Haberer, G. Kraft, D. Schardt, U. Weber. Treatment planning for heavy ion radiotherapy: physical beam model and dose optimization. *Phys. Med. Biol.*, 45:3299–3317, 2000.
- [Kuh04a] A. Kuhn, J.S. Karp, G. Muehlechner, F.W. Newcomer, R. VanBerg. Performance assessment of pixelated LaBr₃ detector modules for TOF PET. In *Proc. IEEE 2004 Med. Ima. Conf.*, Rome, Italy, Oct. 2004. M9-059.
- [Kuh04b] A. Kuhn, S. Surti, J.S. Karp, P.S. Raby, K.S. Shah, A.E. Perkins, G. Muehlechner. Design of a lanthanum bromide detector for time-of-flight PET. *IEEE T. Nucl. Sci.*, 51:2550–2557, 2004.
- [Kyu94] H. Kyushima, Y. Hasegawa, A. Atsumi, K. Nagura, H. Yokota, M. Ito, J. Takeuchi, K. Oba, H. Matsuura, S. Suzuki. Photomultiplier tube of new dynode configuration. *IEEE T. Nucl. Sci.*, 41(4):725–729, 1994.
- [Lar63] B. Larsson, L. Leksell, B. Rexed. The use of high energy protons for cerebral surgery in man. *Acta. Chir. Scand.*, 125:1–7, 1963.
- [Lau99] K. Lauckner. *Entwicklung eines iterativen 3D Rekonstruktionsverfahrens für die Kontrolle der Tumorbehandlung mit Schwerionen mittels der Positronen-Emissions-Tomographie*. PhD thesis, Dresden University of Technology, Dresden, 1999.
- [Lau00] K. Lauckner, P. Crespo, J. Pawelke, W. Enghardt, G. Kraft. An LSO-based scanner for in-beam PET: a feasibility study. In *Proc. IEEE 2000 Med. Ima. Conf.*, Lyon, France, Oct. 2000. M14-289.
- [Lav83] M. Laval, M. Moszyński, R. Allemand, E. Cormoreche, P. Guinet, R. Odru, J. Vacher. Barium fluoride - inorganic scintillator for subnanosecond timing. *Nucl. Instrum. Meth.*, 206:169–176, 1983.

- [Lec02] P. Lecoq, J. Varela. A dedicated PET camera for mammography. *Nucl. Instrum. Meth. A*, 486:1–6, 2002.
- [Leo94] W.R. Leo. *Techniques for nuclear and particle physics experiments*. Springer-Verlag, 1994.
- [Lin05] <http://learntech.uwe.ac.uk/radiography/RScience/linac/beamshapingcomponents.htm>, available in Jun. 2005.
- [Lit68] J. Litton, J.T. Lyman, C.A. Tobias. Penetration of high-energy heavy ions with the inclusion of Coulomb, nuclear and other stochastic processes, Lawrence Berkeley Laboratory, UCLA 17392 rev., UC-34 Physics, TID 4500 (2nd. edition), 1968.
- [Lla88] J. Llacer. Positron emission medical measurements with accelerated radioactive ion beams. *Nucl. Sci. Appl.*, 3:111–131, 1988.
- [Lom99] A.J. Lomax, T. Bortfeld, G. Goitein, J. Debus, C. Dykstra, P.A. Tercier, P.A. Coucke, R.O. Mirimanoff. A treatment planning inter-comparison of proton and intensity modulated photon radiotherapy. *Radiother. Oncol.*, 51(3):257–271, 1999.
- [Lub04] M. Lubberink, H. Schneider, H. Lundqvist. Modified dead time correction for prompt gamma radiation emitting PET isotopes. In *Proc. IEEE 2004 Med. Ima. Conf.*, Rome, Italy, Oct. 2004. M5-322.
- [Lyn91a] G.R. Lynch, O.I. Dahl. Approximations to multiple Coulomb scattering. *Nucl. Instrum. Meth. B*, 58(1):6–10, 1991.
- [Lyn91b] D.E. Lyndstadt, J.R. Castro, T.L. Phillips. Neon ion radiotherapy: results of the phase I-II clinical trial. *Int. J. Radiat. Oncol.*, 20:761–769, 1991.
- [Maj85] S. Majewski, D. Anderson. Radiation damage test of barium fluoride scintillator. *Nucl. Instrum. Meth. A*, 241:76–79, 1985.
- [Mar66] P. Marmier, E. Sheldon. *Physics of Nuclei and Particles*, volume 1. Academic Press, New York, 1966.
- [McI60] M.C. McIntyre, T.L. Watts, F.C. Jobes. Neutron transfer and the tunneling mechanism in the bombardment of gold by nitrogen. *Phys. Rev.*, 19(3):1331–1339, 1960.
- [Mel91] C.L. Melcher. Lutetium orthosilicate single crystal scintillation detector. *U.S. Patent*, (4 958 080 /5 025 151), 1990/1991.
- [Mel92] C.L. Melcher, J.S. Schweitzer. Cerium-doped lutetium oxyorthosilicate: a fast, efficient new scintillator. *IEEE T. Nucl. Sci.*, 39(4):502–505, 1992.
- [Min94] B.I. Minkov. Promising new lutetium based single crystals for fast scintillation. *Functional Materials*, 1:103–105, 1994.
- [Mol48] G. Molière. Theorie der Streuung schneller geladener Teilchen II, Mehrfach- und Vielfachstreuung. *Z. Naturforschung A*, 3:78–97, 1948.
- [Mos83] M. Moszyński, R. Allemand, M. Laval, R. Odru, J. Vacher. Recent progress in fast timing with CsF scintillators in application to time-of-flight positron tomography in medicine. *Nucl. Instrum. Meth.*, 205:239–240, 1983.

- [Mos93] W.W. Moses, S.E. Derenzo. Empirical observation of resolution degradation in positron emission tomographs utilizing block detectors. *J. Nucl. Med.*, 34:101–102, 1993.
- [Mos94] W.W. Moses, S.E. Derenzo, T.F. Budinger. PET detector modules based on novel detector technologies. *Nucl. Instrum. Meth. A*, 353:189–194, 1994.
- [Mos95] W.W. Moses, S.E. Derenzo, A. Fyodorov, M. Korzhik, A. Gektin, B. Minkov, V. Aslanov. LuAlO₃:Ce - a high density, high speed scintillator for gamma detection. *IEEE T. Nucl. Sci.*, 42:275–279, 1995.
- [Mos96] W.W. Moses, S.E. Derenzo. Scintillators for positron emission tomography. In *SCINT95 Proc. of the Int. Conf. on Inorganic Scintillators and their Applications*, pages 9–16, Delft, The Netherlands, 1996. Delft University Press.
- [Mos99a] W.W. Moses, S.E. Derenzo. Prospects for time-of-flight PET using LSO scintillator. *IEEE T. Nucl. Sci.*, 46:474–478, 1999.
- [Mos99b] M. Moszyński, M. Balcerzyk, M. Kapusta, D. Wolski, C.L. Melcher. Large size LSO:Ce and YSO:Ce scintillators for 50 MeV range γ -ray detector. In *Proc. IEEE 1999 Nucl. Sci. Symp.*, Seattle, WA, USA, Oct. 1999. N20-18.
- [Mos00] W.W. Moses. Scintillator requirements for medical imaging. In *SCINT99 Proc. of the 5th Int. Conf. on Inorganic Scintillators and their Applications*, pages 11–21, M. V. Lomonosov State University, Moscow, 2000.
- [Mos01] M. Moszyński, M. Kapusta, M. Szawlowski, D. Wolski, I. Wegrzecka, M. Wegrzecki. Comparative study of avalanche photodiodes with different structures in scintillation detection. *IEEE T. Nucl. Sci.*, 48:1205–1210, 2001.
- [Mos02] W.W. Moses. Synergies between electromagnetic calorimetry and PET. *Lawrence Berkeley National Laboratory*, July 2002. Paper LBNL-51197, <http://repositories.cdlib.org/lbnl/LBNL-51197>, available in Jun. 2005.
- [Mos03] J.-B. Mosset, S. Saladino, J.-F. Loude, C. Morel. Characterisation of arrays of avalanche photodiodes for small animal positron emission tomography. *Nucl. Instrum. Meth. A*, 504:325–330, 2003.
- [Mos04] W.W. Moses. Factors influencing timing resolution in a commercial LSO PET camera. In *Proc. IEEE 2004 Nucl. Sci. Symp. and Med. Ima. Conf.*, Rome, Italy, Oct. 2004. JNM2-1.
- [Mue02] G. Muehllehner, J.S. Karp, S. Surti. Design considerations for PET scanners. *Q. J. Nucl. Med.*, 46(1):16–23, 2002.
- [Nat05] <http://www.ni.com/linux/ni488d1.htm>, available in Jun. 2005.
- [Nik04] A. Nikoghosyan, D. Schulz-Ertner, B. Diding, O. Jäkel, I. Zuna, A. Höss, M. Wannenmacher, J. Debus. Evaluation of therapeutic potential of heavy ion therapy for patients with locally advanced prostate cancer. *Int. J. Radiat. Oncol.*, 58(1):89–97, 2004.
- [Nör80] W. Nörenberg. Basic concepts in the description of collisions between heavy nuclei. In R. Bock, editor, *Heavy Ion Collisions*, pages 1–43. North-Holland, 1980.

- [Oel96] U. Oelfke, G.K.Y. Lam, M.S. Atkins. Proton dose monitoring with PET: quantitative studies in Lucite. *Phys. Med. Biol.*, 41:177–196, 1996.
- [Oli79] L.F. Oliveira, R. Donangelo, J.O. Rasmussen. Abrasion-ablation calculations of large fragment yields from relativistic heavy ion reactions. *Phys. Rev. C*, 19(3):826–833, 1979.
- [Org02] G. Organtini. The CMS electromagnetic calorimeter. In *Proc. IEEE 2002 Nucl. Sci. Symp.*, Norfolk, VI, USA, Nov. 2002. N19-1.
- [Ort05] Ortec 142AH preamplifier. Users manual. <http://www.ortec-online.com/electronics/preamp/142ah.htm>, available in Jun. 2005.
- [Pac00] E. Pace, R. Di Benedetto, S. Scuderi. Fast stable visible-blind and highly sensitive CVD diamond UV photodetectors for a laboratory and space applications. *Diam. Relat. Mater.*, 9:987–993, 2000.
- [Par77] K.S. Parthasarathy. Concentrations of the decay products of ^{222}Rn in a basement laboratory. *Phys. Med. Biol.*, 22(2):341–347, 1977.
- [Par02a] K. Parodi, W. Enghardt. An interactive approach for local dose quantification from in-beam PET data. *Wiss.-Tech. Ber. FZR-341 (Ann. Rep. 2001)*, page 98, 2002.
- [Par02b] K. Parodi, W. Enghardt, T. Haberer. In-beam PET measurements of β^+ radioactivity induced by proton beams. *Phys. Med. Biol.*, 47:21–36, 2002.
- [Par04] K. Parodi. *On the feasibility of dose quantification with in-beam PET data in radiotherapy with ^{12}C and proton beams*. PhD thesis, Dresden University of Technology, Dresden, Nov. 2004.
- [Par05a] K. Parodi, F. Pönisch, W. Enghardt. Experimental study on the feasibility of in-beam PET for accurate monitoring of proton therapy. *IEEE T. Nucl. Sci.*, 52(3):778–786, 2005.
- [Par05b] K. Parodi, P. Crespo, H. Eickhoff, T. Haberer, J. Pawelke, D. Schardt, W. Enghardt. Random coincidences during in-beam PET measurements at microbunched therapeutic ion beams. *Nucl. Instrum. Meth. A*, 545:446–458, 2005.
- [Pau00] D. Pauwels, N. Le Masson, B. Viana, A. Kahn-Harari, E.V.D. van Loef, P. Dorenbos, C.W.E. van Eijk. A novel inorganic scintillator: $\text{Lu}_2\text{Si}_2\text{O}_7:\text{Ce}^{3+}$ (LPS). *IEEE T. Nucl. Sci.*, 47:1787–1790, 2000.
- [Paw95] J. Pawelke. *Methodische Untersuchungen zum Einsatz der Positronen-Emissions-Tomographie in der Leichtionen-Tumorthherapie*. PhD thesis, Dresden University of Technology, Dresden, June 1995.
- [Paw96] J. Pawelke, L. Byars, W. Enghardt, W.D. Fromm, H. Geissel, B.G. Hasch, K. Lauckner, P. Manfraß, D. Schardt, M. Sobiella. The investigation of different cameras for in-beam PET imaging. *Phys. Med. Biol.*, 41:279–296, 1996.
- [Paw97] J. Pawelke, W. Enghardt, Th. Haberer, B.G. Hasch, R. Hinz, M. Krämer, K. Lauckner, M. Sobiella. In-beam PET imaging for the control of heavy-ion tumour therapy. *IEEE T. Nucl. Sci.*, 44(4):1492–1498, 1997.

- [Ped95] E. Pedroni, R. Bacher, H. Blattmann, T. Böhringer, A. Coray, A. Lomax, S. Lin, G. Munkel, S. Scheib, U. Schneider, A. Tourovsky. The 200 MeV proton therapy project at the Paul Scherrer Institute: conceptual design and practical realisation. *Med. Phys.*, 22(1):37–53, 1995.
- [Per04] H. Pernegger, H. Frais-Kölbl, E. Griesmayer, H. Kagan. Design and test of a high-speed single-particle beam monitor. *Nucl. Instrum. Meth. A*, 535:108–114, 2004.
- [Pet89] M.D. Petroff, M.G. Stapelbroek. Photon-counting solid-state photomultiplier. *IEEE T. Nucl. Sci.*, 36(1):158–162, 1989.
- [Pet94] P. Petti, A.J. Lennox. Hadronic radiotherapy. *Ann. Rev. Nucl. Part. S.*, 44:155–197, 1994.
- [Phe75] M.E. Phelps, E.J. Hoffman, N.A. Mullani, M.M. Ter-Pogossian. Application of annihilation coincidence detection to transaxial reconstruction tomography. *J. Nucl. Med.*, 16:210–224, 1975.
- [Pic01] B.J. Pichler, F. Bernecker, G. Boning, M. Rafecas, W. Pimpl, M. Schwaiger, E. Lorenz, S.I. Ziegler. A 4×8 APD array, consisting of 2 monolithic silicon wafers, coupled to a 32-channel LSO matrix for high-resolution PET. *IEEE T. Nucl. Sci.*, 48(2):1391–1396, 2001.
- [Pic04] B.J. Pichler, B.K. Swann, J. Rochelle, R.E. Nutt, S.R. Cherry, S.B. Siegel. Lutetium oxyorthosilicate block detector readout by avalanche photodiode arrays for high resolution animal PET. *Phys. Med. Biol.*, 49:4305–4319, 2004.
- [Pid03] L. Pidol, A. Kahn-Harari, B. Viana, E. Virey, B. Ferrand, P. Dorenbos, J.T.M de Haas, C.W.E. van Eijk. High efficiency of lutetium silicate scintillators, Ce-doped LPS and LYSO crystals. In *Proc. IEEE 2003 Nucl. Sci. Symp.*, Portland, OR, USA, Oct. 2003. N27-4.
- [Pit05] <http://www.pituitary.com>, available in Jun. 2005. Last update: May. 2005.
- [Pön03a] F. Pönisch. *Optimierung der Positronen-Emissions-Tomographie bei der Schwerionentherapie auf der Basis von Röntgentomogrammen*. PhD thesis, Dresden University of Technology, Dresden, 2003.
- [Pön03b] F. Pönisch, W. Enghardt, K. Lauckner. Attenuation and scatter correction for in-beam positron emission tomography monitoring of tumour irradiations with heavy ions. *Phys. Med. Biol.*, 48:2419–2436, 2003.
- [Pön04] F. Pönisch, K. Parodi, B.G. Hasch, W. Enghardt. The modelling of positron emitter production and PET imaging during carbon ion therapy. *Phys. Med. Biol.*, 49:5217–5232, 2004.
- [Pre97] K. Prelec. Ions and accelerators for cancer treatment. *Fizika B*, 6:177–206, 1997.
- [PSI99] <http://abe.web.psi.ch/accelerators/ringcyc.html>, available in Jun. 2005., Last update: Jan. 1999.
- [Reg02] M. Regler, M. Benedikt, K. Poljanc. Medical accelerators for hadron therapy with protons and carbon ions. In *CERN Accelerator School*, Seville, Oct. 2002. Hephypub-757/02.

- [Rei98] C.O. Reinold, D.R. Schultz, U. Bechthold, G. Kraft, S. Hagman H. Schmidt-Böcking. Ternary ridge of ejected electrons from fast ion-atom collisions. *Phys. Rev. A.*, 58(3):2611–2614, 1998.
- [Rey56] H.L. Reynolds, A. Zucker. Nuclear reactions produced by nitrogen on nitrogen. *Phys. Rev.*, 101(1):166–171, 1956.
- [Ros00] A.B. Rosenfeld, P.D. Bradley, I. Cornelius, G. I. Kaplan, B.J. Allen, J.B. Flanz, M. Goitein, A. van Meerbeeck, J. Schubert, J. Bailey, Y. Tabkada, A. Maruhashi, Y. Hayakawa. New silicon detector for microdosimetry applications in proton therapy. *IEEE T. Nucl. Sci.*, 47(4):1386–1394, 2000.
- [San04] A.I. Santos, A. Trindade et al. Design and evaluation of the clear-PEM detector for positron emission mammography. In *Proc. IEEE 2004 Med. Ima. Conf.*, Rome, Italy, Oct. 2004. M10-28.
- [Sch89] W. Schimmerling, J. Miller, M. Wong, M. Rapkin, J. Horward, H. Spieker, B.V. Jarret. The fragmentation of 670 AMeV neon as a function of depth in water. *Radiat. Res.*, 120:36–71, 1989.
- [Sch91] T. Schwab. *Transport von Schwerionen durch Materie innerhalb ionenoptischer Systeme*. PhD thesis, University of Gießen, Gießen, 1991. GSI report 91-10.
- [Sch92] P. Schotanus, P. Dorenbos, V.D Ryzhikov. Detection of CdS(Te) and ZnSe(Te) scintillation light with silicon photodiodes. *IEEE T. Nucl. Sci.*, 39(4):546–550, 1992.
- [Sch96a] I. Schall, D. Schardt, H. Geissel, H. Irnich, E. Kankleit, G. Kraft, A. Magel, M.F. Mohar, G. Münzenberg, F. Nickel, C. Scheidenberger, W. Schwab. Charge changing nuclear reactions of relativistic light ion beams ($5 \leq Z \leq 10$) passing through thick absorbers. *Nucl. Instrum. Meth. B*, 117:221–234, 1996.
- [Sch96b] D. Schardt, I. Schall, H. Geissel, H. Irnich, G. Kraft, A. Magel, M.F. Mohar, G. Münzenberg, F. Nickel, C. Scheidenberger, W. Schwab, L. Sihver. Nuclear fragmentation of high-energy heavy-ion beams in water. *Adv. Space Res.*, 17(2):287–294, 1996.
- [Sch96c] W.H. Scharf, O.A. Chomicki. Medical accelerators in radiotherapy: past, present and future. *Phys. Medica*, XII(4):199–226, 1996.
- [Sch96d] M. Scholz, G. Kraft. Track structure and the calculation of biological effects of heavy charged particles. *Adv. Space Res.*, (1-2):5–14, 1996.
- [Sch02a] D. Schulz-Ertner, T. Haberer, M. Scholz, C. Thilmann, F. Wenz, O. Jäkel, G. Kraft, M. Wannemacher, J. Debus. Acute radiation-induced toxicity of heavy ion radiotherapy delivered with intensity modulated pencil beam scanning in patients with base of skull tumors. *Radiother. Oncol.*, 64:189–195, 2002.
- [Sch02b] D. Schulz-Ertner, T. Haberer, O. Jäkel, C. Thilmann, M. Krämer, W. Enghardt, G. Kraft, M. Wannemacher, J. Debus. Radiotherapy for chordomas and low-grade chondrosarcomas of the skull base with carbon ions. *Int. J. Radiat. Oncol.*, 53(1):36–42, 2002.
- [Sch03a] D. Schulz-Ertner, A. Nikoghosyan, B. Didinger, C.P. Karger, O. Jäkel, M. Wannemacher, J. Debus. Treatment planning intercomparison for spinal chordomas using intensity-modulated photon radiation therapy (IMRT) and carbon ions. *Phys. Med. Biol.*, 48:2617–2631, 2003.

- [Sch03b] D. Schulz-Ertner, A. Nikoghosyan, C. Thilmann, T. Haberer, O. Jäkel, C. Karger, M. Scholz, G. Kraft, M. Wannemacher, J. Debus. Carbon ion radiotherapy for chordomas and low grade chondrosarcomas of the skull base. *Strahlenther. Onkol.*, 179:598–605, 2003.
- [Sch03c] D. Schulz-Ertner, A. Nikoghosyan, O. Jäkel, T. Haberer, G. Kraft, M. Scholz, M. Wannemacher, J. Debus. Feasibility and toxicity of combined photon and carbon ion radiotherapy for locally advanced adenoid cystic carcinomas. *Int. J. Radiat. Oncol.*, 62(2):391–398, 2003.
- [Sch03d] D. Schulz-Ertner, B. Didingler, A. Nikoghosyan, O. Jäkel, I. Zuna, M. Wannemacher, J. Debus. Optimization of radiation therapy for locally advanced adenoid cystic carcinomas with infiltration of the skull base using photon intensity-modulated radiation therapy (IMRT) and a carbon ion boost. *Strahlenther. Onkol.*, 179(5):345–51, 2003.
- [Sch04] D. Schulz-Ertner, J. Debus, A. Nikoghosyan, C. Thilmann, M. Wannemacher, O. Jäkel, C. Karger, P. Heeg, T. Haberer, D. Schardt, M. Scholz, M. Krämer, E. Rietzel, G. Kraft. Heavy ion therapy at GSI. *GSI Rep. 2004-1 (Ann. Rep. 2003)*, page 172, 2004.
- [Sha04] K.S. Shah, J. Glodo, W. Higgins, E.V.D. van Loef, W.W. Moses, S.E. Derenzo, M.J. Weber. CeBr₃ scintillators for gamma-ray spectroscopy. In *Proc. IEEE 2004 Room Temp. Sem. Det.*, Rome, Italy, Oct. 2004. R04-1.
- [She82] L.A. Shepp and Y. Vardi. Maximum likelihood reconstruction for emission tomography. *IEEE T. Med. Imaging*, 1(2):113–122, 1982.
- [Shi04] S. Shimizu, K. Kurashige, T. Usui, N. Shimura, K. Sumiya, N. Senguttuvan, A. Gunji, M. Kamada, H. Ishibashi. Scintillation properties of LGSO crystal. In *Proc. IEEE 2004 Med. Ima. Conf.*, Rome, Italy, Oct. 2004. M5-414.
- [Sho84] M.D. Short. Gamma camera systems. *Nucl. Instrum. Meth.*, 221:142–149, 1984.
- [Sie04] Siemens Medical Solutions. Particle therapy, getting to the point, Siemens AG, Medical Solutions, Erlangen, Germany, 2004. Order No. A91100-M2600-C689-2-7600.
- [Sih93] L. Sihver, C.H. Tsao, R. Silberberg, T. Kanai, R.F. Barghouty. Total reaction and partial cross section calculations in proton-nucleus ($Z_t \leq 26$) and nucleus-nucleus reactions (Z_p and $Z_t \leq 26$). *Phys. Rev. C*, 47(3):1225–1236, 1993.
- [Smi96] K.M. Smith. GaAs detector status. *Nucl. Instrum. Meth. A*, 383:75–80, 1996.
- [Spi98] T.J. Spinks, M.P. Miller, D.L. Bailey, P.M. Bloomfield, L. Livieratos, T. Jones. The effect of activity outside the direct field of view in a 3D-only whole-body positron tomograph. *Phys. Med. Biol.*, 43:895–904, 1998.
- [Suz93] S. Suzuki, T. Nakaya, A. Suzuki, H. Suzuki, K. Yoshioka, Y. Yoshizawa. PMTs of superior time resolution, wide dynamic range, and low cross-talk multi-anode PMTs. *IEEE T. Nucl. Sci.*, 40(4):431–433, 1993.
- [Sve98] R. Svensson, M. Åsell, P. Näfstadius, A. Brahme. Target, purging magnet and electron collector design for scanned high-energy photon beams. *Phys. Med. Biol.*, 43:1091–1112, 1998.

- [Tak83] K. Takagi, T. Fukazawa. Cerium-activated Gd_2SiO_5 single crystal scintillator. *Appl. Phys. Lett.*, 42:43–45, 1983.
- [Tan98] M. Tanaka, K. Hara, S. Kim, K. Kondo, H. Takano, M. Kobayashi, H. Ishibashi, K. Kurashige, K. Susa, M. Ishii. Applications of cerium-doped gadolinium silicate $\text{Gd}_2\text{SiO}_5:\text{Ce}$ scintillator to calorimeters in high-radiation environment. *Nucl. Instrum. Meth. A*, 404:283–294, 1998.
- [Tob52] C.A. Tobias, H.O. Anger, J.H. Lawrence. Radiological use of high energy deuterons and alpha particles. *Am. J. Roentgenol. Radiat. Ther. Nucl. Med.*, 67:1–27, 1952.
- [Tob71] C.A. Tobias, A. Chatterjee, A.R. Smith. Radioactive fragmentation of N^{7+} ion beam observed in a beryllium target. *Phys. Lett. A*, 37:119–120, 1971.
- [Tob77] C.A. Tobias, E.V. Benton, M.P. Capp, A. Chatterjee, M.R. Cruty, R.P. Henke. Particle radiography and autoactivation. *Int. J. Radiat. Oncol.*, 3:35–44, 1977.
- [TOI04] Table of Radioactive Isotopes online. <http://ie.lbl.gov/toi>, available Jun. 2005. Last update: Jan. 2004.
- [Tom03] T. Tomitani, J. Pawelke, M. Kanazawa, K. Yoshikawa, K. Yoshida, M. Sato, A. Takami, M. Koga, Y. Futami, A. Kitagawa, E. Urakabe, M. Suda, H. Mizuno, T. Kanai, H. Matsuura, I. Shinoda, S. Takizawa. Washout studies of ^{11}C in rabbit thigh muscle implanted by secondary beams of HIMAC. *Phys. Med. Biol.*, 48:875–889, 2003.
- [Tro05] <http://www.trolltech.com>, available in Jun. 2005.
- [Ura01] E. Urakabe, T. Kanai, M. Kanazawa, A. Kitagawa, K. Noda, T. Tomitani, M. Suda, Y. Iseki, K. Hanawa, K. Satoh, M. Shimbo, H. Mizuno, Y. Hirata, Y. Futami, Y. Iwashita, A. Noda. Spot scanning using radioactive ^{11}C beams for heavy-ion radiotherapy. *Jpn. J. Appl. Phys. A*, 40:2540–2548, 2001.
- [Var05] J. Varela. Clear PEM, a dedicated PET camera for mammography, LIP Lisbon, Portugal and CERN, Geneva, Switzerland, March 2005. Personal communication.
- [vE02] C.W.E. van Eijk. Inorganic scintillators in medical imaging. *Phys. Med. Biol.*, 47:85–106, 2002.
- [Ver05] P.E. Vert, G. Bohner, M. Boutemour, J. Lecoq, P. Le Du, G. Mathez, P. Mangeot, G. Montarou. Contribution of HEP electronics technics to the medical imaging field. In *Proc. IEEE-NPSS Real Time Conf. 2005*, Stockholm, Sweden, Jun. 2005. S9-3.
- [vL00] E.V.D. van Loef, P. Dorenbos, C.W.E. van Eijk, K. Krämer, H.U. Güdel. High-energy-resolution scintillator: Ce^{3+} activated LaCl_3 . *Appl. Phys. Lett.*, 77:1467–1468, 2000.
- [vL01] E.V.D. van Loef, P. Dorenbos, C.W.E. van Eijk, K. Krämer, H.U. Güdel. High-energy-resolution scintillator: Ce^{3+} activated LaBr_3 . *Appl. Phys. Lett.*, 79:1573–1575, 2001.
- [Vyn89] S. Vynckier, F. Vanneste, F. Richard, A. Bol, C. Michel, A. Wambersie. Control of patient positioning for fast neutron therapy using positron emission tomography. *Brit. J. Radiol.*, 62:1031–1032, 1989.

- [Wat04] C.C. Watson, M.E. Casey, L. Eriksson, T. Mulnix, D. Adams, B. Bendriem. NEMA NU 2 performance tests for scanners with intrinsic radioactivity. *J. Nucl. Med.*, 45:822–826, 2004.
- [Web73] M.J. Weber, R.R. Monchamp. Luminescence of $\text{Bi}_4\text{Ge}_3\text{O}_{12}$: spectral and decay properties. *J. Appl. Phys.*, 44:5495–5499, 1973.
- [Web90] S. Webb, editor. *The Physics of Medical Imaging*. Adam Hilger, Bristol, 1990.
- [Web96] U. Weber. *Volumenkonforme Bestrahlung mit Kohlenstoffionen zur Vorbereitung einer Strahlentherapie*. PhD thesis, University of Kassel, Kassel, 1996.
- [Wey03] W.K. Weyrather, J. Debus. Particle beams for cancer therapy. *Clin. Oncol.*, 15:23–28, 2003.
- [Wie94] K. Wienhard, M. Dahlbom, L. Eriksson, C. Michel, T. Bruckbauer, U. Pietrzyk, W.-D. Heiss. The ECAT EXACT HR: performance of a new high resolution positron camera. *J. Comput. Assist. Tomo.*, 18:110–118, 1994.
- [Wil46] R.R. Wilson. Radiobiological use of fast protons. *Radiology*, 47:487–491, 1946.
- [Wil83] J. Wilson, J.F.B. Hawkes. *Optoelectronics: An Introduction*. Prentice-Hall International, London, 1983.
- [Won90] M. Wong, W. Schimmerling, M.H. Phillips, B.A. Ludewigt, D.A. Landis, J.T. Walton, S.B. Curtis. The multiple Coulomb scattering of very heavy charged particles. *Med. Phys.*, 17(2):163–171, 1990.
- [Won94] C.Y. Wong. *Introduction to high-energy heavy-ion collisions*. World Scientific, Singapore, 1994.
- [Xco99] XCOM: Photon cross sections database. <http://physics.nist.gov/PhysRefData/Xcom/Text/XCOM.html>, available Jun. 2005. Last update: Nov. 1999.
- [Zhu97] R.-Y. Zhu. Precision crystal calorimetry in future high energy colliders. *IEEE T. Nucl. Sci.*, 44(3):468–476, 1997.
- [Zhu98] R.-Y. Zhu. Radiation damage in scintillating crystals. *Nucl. Instrum. Meth. A*, 413:297–311, 1998.
- [Zie85] J.F. Ziegler, J.F. Biersack, U. Littmark. *The stopping and range of ions in solids*. Pergamon Press, 1985.
- [Zie99] J.F. Ziegler. Stopping of energetic light ions in elemental matter. *J. Appl. Phys.*, 85(3):1249–1272, 1999.

Acknowledgements

I would like to thank, chronologically:

- Dr. Reinhard Simon from GSI for introducing me to the Heavy Ion Therapy Project during the lunch breaks and the interfaces to my night shifts in my first visit to GSI back in 1999.
- My academic supervisor Prof. Dr. Gerhard Kraft, from GSI, for the welcome to his biophysics group, for proof-reading this manuscript and for the initial support in my introductory steps into the world of the carbon therapy project. This included several papers and clarifying discussions, as well as several images later used in the first chapter of this thesis.
- My scientific supervisor Dr. habil. Wolfgang Enghardt, for welcoming me to his in-beam PET group at the FZ Rossendorf. I thank Dr. Enghardt also for sharing with me the tasks that composed this thesis: the need to generalize the reconstruction routine and to optimize the geometry of the tomograph; the idea and financial means to envisage new, state-of-the-art detectors; the problematics of the high-yield background during particle extraction, including the first time-correlation results from Dr. Katia Parodi, then my in-beam PET PhD colleague, which lead, together with this work, to our common FZR patent; and last but not least, the time consuming task of proof-reading and correcting this manuscript.
- From GSI, Dr. Thomas Haberer for his constant patience in answering all questions, for his helpful presence during all therapeutic irradiation and in-beam experiments, for providing Fig. 1.12 and for having provided the beam time windows for all the experiments presented in this dissertation. I thank Dr. Michael Krämer for interesting discussions and for sharing the image that lead to Fig. 1.15. I acknowledge Dr. Dieter Schardt, Dr. Peter Heeg, Eng. Wolfgang Becher, Dr. Sven Grözinger, Dr. Bernd Voss and Cristoph Bert for their help at several occasions when a problem had to be solved immediately (or not), either in cave M or in the medical control room. I thank the whole biophysics group for the extremelly nice, productive working atmosphere. Although many of the following are now spread around the world, I'd like to particularly point out Dr. Sven Grözinger and Eng. Wolfgang Becher (again), Dr. Konstanze Gunzert-Marx, Dr. Eike Rietzel, Dr. Corinna Kausch, Petra Sander, Dr. Qiang Li, Dr. Stephanie Berger and Erwin (Kevin) Tenhumberg, Dr. Torsten Grösser, Dr. Claudia Wiese and Frank, Dr. Stephan Brons, Mrs. Kirsten Langbein and Mrs. Angela Phalen-Weiß.
- From FZR, Prof. Dr. Eckart Grosse for allowing me to work in his Institute of Nuclear and Hadron Physics. Dr. Kathrin Lauckner, now on a private company, for providing the initial scientific support during my learning into the field of in-beam PET, including the sharing of the reconstruction routine that she developed for BASTEL. Dr. Jörg Pawelke for his availability to answer all questions and for providing support in any necessary task. I thank Dr. Pawelke particularly for the time demanding task of organizing the cut of the more than 64 LSO crystals used to construct the LSO/APDA detectors, for polishing them after cutting, for providing the IDL code calculating the β -decay spectrum, plotted in Fig. 5.17, and for proof-reading this manuscript. I acknowledge my working colleagues, some of them now placed around the world, for their friendship and the shared discussions or routine codes, Dr. Rainer Hinz, Dr. Falk Pönisch, Dr. Katia Parodi, Dr. Anna Lehnert, Dr. Ulf Lehnert, Fine Fiedler, Uwe Reichelt, Behnam Azadegan, Thomas Barthelt, Thomas Würschig, Georgy Shakirin and Daniela Möckel. I thank Georgy Shakirin also for proof-reading this manuscript, and I thank particularly Thomas Barthelt for the many hours, common efforts and his personal engagement in the preparation and execution of the randoms suppression experiments. From the detector laboratory I would like to greatly acknowledge Jochen Hutsch, Eng. Manfred Sobiella and Liane Heinrich also for the many hours and involvement in manufacturing the LSO/APDA detectors. From the division of nuclear physics I thank Dr. Ronald Schwengner for the fast and efficient help with the analysis of the γ -ray lines from the LSO activation studies, Dr. Andreas Wagner for the shared electronics

modules and knowledge and Mr. Berlin for preparing more than 150 meters of cabling. A special acknowledgment must be made to Eng. Klaus Heidel, from the same division, without whom this thesis would not have been possible. This acknowledgment extends from the preparation of the motherboards for the preamplifiers reading the LSO/APDA detectors, to the testing of the preamplifiers, their optimization with hints to their designers, as well as many other issues: power supply assembling, the simulation of several readout electronic components with PSPICE, and innumeral discussions about power consumption, timing, cabling and other optimizations. Klaus, thank you for the many hours out there on the field. I thank also Eng. Andreas Steinbrecher, then at the Institut für Energetik und Umwelt GmbH, Rossendorf, for his personal involvement in the study with PET on a separate gantry, and for sharing the images that were adapted to Fig. 3.4. I acknowledge Dr. Waldemar Neubert, Dr. Wolfgang Wagner, Dr. Bärbel and Dr. Lothar Naumann, Jenny Philipp, Elisabeth Leßmann, Krassimir Kossev, Martin Erhard, Alexander Sadowski, Kalliopi Kanaki, Manfred Beckers, Christoph Klein, Dr. Schlett, Mrs. Schneiderei and Jens Steiner for the relaxed working atmosphere inside and outside the division of radiation physics. I thank particularly Dr. Enghardt, Fine Fiedler and Martin Erhard for the great help in writing the German summary of this thesis.

- From Heidelberg, the whole medical personnel and the team of medical physicists. Their dedication to the tumor therapy project is a motivation on the professional and personal levels.
- From the ASINS, Poland, Prof. Dr. Marek Moszyński for a fruitful collaboration with his institute and for sharing his time and knowledge on scintillators and solid state detectors, his former PhD student Dr. Maciej Kapusta for the many hours spent together in the laboratory and for useful suggestions, Eng. Dariusz Wolski for the design and production of the preamplifiers that read the LSO/APDA, and Prof. Dr. Zbigniew Guzik for interesting discussions on other levels of physics.
- From MedAustron, Austria, Prof. Dr. Helmut Frais-Kölbl, for the fruitful co-work before and during the randoms suppression experiments, including sharing his expertise and suggestions on the field of nano-second (and below) timing, together with the operation of the CVD detector, and the shared data resulting in Fig. 6.4, and Prof. Dr. Erich Griesmayer for participating in the collaboration, providing the means so that we could use the diamond detector.
- From the LIP-Lisbon, Portugal, Prof. Dr. João Varela, Andreia Trindade and Pedro Rodrigues, for the useful discussions and exchange of information concerning the avalanche photodiode from Hamamatsu, the LSO scintillator and for sharing their knowledge regarding their fast and advanced acquisition technology.

I thank all my teachers at the University of Coimbra, Portugal, for the shared knowledge in the fields of physics and instrumentation during my under-graduate studies. I thank particularly Prof. Dr. Policarpo, Dr. Isabel Lopes, Dr. Vitaly Chepel, Dr. van der Marel and Luís Janeiro for the productive atmosphere within the liquid xenon team at the LIP-Coimbra. I thank also Prof. Dr. Mário Pimenta, Dr. Fernando Barão and Dr. Patrícia Gonçalves, from LIP-Lisbon, for their help and shared knowledge in the field of data evaluation and simulation for astroparticle physics detectors before I joined the German Heavy Ion Therapy Collaboration.

I acknowledge my funding sources, namely the Fundação Portuguesa para a Ciência e a Tecnologia, Lisboa, Portugal, supporting me in Germany from October 1999 to December 2002 through grant PRAXIS XXI / BD / 18011 / 98, and GSI and FZR for providing support from January 2003 onwards.

On the personal level, I thank the true friendship of Miguel, Chiqui, Faouzi, Fairouz, Farouk, Christiane, Andrea, Lutz, Isabel, P. Nuno, Aga, Iwona, family Colvenbach and family West. I thank in a very special way D. Alice Carvalho for the dedication put into teaching and forming human beings.

To my American host family, with whom I studied one year in the United States: Mom, Dad (always present), Kyle and Jenna, the opening of your family to a newcomer, the sharing of your family laces in that year and after, the time and dedication you've put forward have always been present in my memory. Thank you. Together with my real-blood family, your share the dedication of this work.

Finally, most importantly and not chronologically, my family. Para além de vos dedicar todo este trabalho, Mã, Pá, e Lena, agradeço-vos a todos pela família unida que somos: Mã, sempre presente, Pá, Guida, Lena, Artur e cunhada Tai, Ricardo e cunhada Carla, o mano mais velho Fabrizio e os meus queridos sobrinhos Micaela, Sofia, Guido e Gift. Que todos juntos, com os nossos pequenos erros mas sobretudo com os nossos esforços, preparemos e usufruemos de um mundo melhor.

Curriculum Vitæ

Personal data

Name: Paulo Alexandre Vieira Crespo
Date of birth: 9 May 1971
Place of birth: Beira, Mozambique
Nationality: Portuguese

Education

Since Oct. 1999 PhD student with the in-beam PET team of the German Heavy Ion Therapy Collaboration
1997 University of Coimbra; graduation in Physics Engineering, specialization in Instrumentation, average 16/20
1994 – 1995 University of Milan and Politechnic of Milan; ERASMUS scholarship,
- Optoelectronics (Polytechnic of Milan): 28/30
- Applied electronics (Dep. of Physics, University of Milan): 28/30
- Laboratory of instrumentation and electronics (idem): 30/30
1991 Beginning of Physics Engineering studies, Dep. of Physics, University of Coimbra
1989 Beginning of Economy studies, Faculty of Economy, University of Coimbra
1987 – 1988 N.Y. State Attica Junior-Senior High School, NY, USA; exchange student, average 90/100

Post-graduate research

1998 – 1999 LIP-Lisbon; within the Alpha Magnetic Spectrometer experiment at CERN
1997 – 1998 LIP-Coimbra; development of a liquid xenon detector for PET
Aug/Sept 1997 CERN; within the tracker system team of the CMS experiment

Patents

2004 W. Enghardt, **P. Crespo**, K. Parodi, J. Pawelke, *Verfahren zur Korrektur der beim Monitoring der strahlentherapeutischen Behandlung mittels in-beam Positronen-Emissions-Tomographie erhaltenen Messwerte*, no. 10 2004 009 784.4, Deutsches Patent- und Markenamt, Feb. 2004. Patent from FZR

Publications in refereed journals

2005 **P. Crespo**, T. Barthel, H. Fraiss-Kölbl, E. Griesmayer, K. Heidel, K. Parodi, J. Pawelke, W. Enghardt, *Suppression of random coincidences during in-beam PET measurements at ion beam radiotherapy facilities*, IEEE Trans. Nucl. Sci., vol. 52, no. 5, pp. 980–7
P. Crespo, G. Shakirin, W. Enghardt, *On the detector arrangement for in-beam PET for hadron therapy monitoring*, Phys. Med. Biol., submitted
P. Crespo, G. Shakirin, W. Enghardt, *Direct time-of-flight for online, in-beam PET: concept and feasibility study*, Phys. Med. Biol., to be submitted
P. Crespo, N. Abolmaali, R. Bergmann, E. Will, W. Enghardt, *Low-activity PET measurements with LSO- and BGO-based positron tomographs*, Phys. Med. Biol., to be submitted
K. Parodi, **P. Crespo**, H. Eickhoff, T. Haberer, J. Pawelke, D. Schardt, W. Enghardt, *Random coincidences during in-beam PET measurements at microbunched therapeutic ion beams*, Nucl. Instr. Meth. A, vol. 545, pp. 446–58
2004 **P. Crespo**, M. Kapusta, J. Pawelke, M. Moszyński, W. Enghardt, *First in-beam PET imaging with LSO/APD-array detectors*, IEEE Trans. Nucl. Sci., vol. 51, no. 5, pp. 2654–61
M. Kapusta, **P. Crespo**, D. Wolski, K. Heidel, L. Heinrich, J. Hutsch, J. Pawelke, M. Sobiella, A. Trzcińska, M. Moszyński, W. Enghardt, *The LSO/APD array as a possible detector for in-beam PET in hadron therapy*, IEEE Trans. Nucl. Sci., vol. 51, no. 4, pp. 1389–94

Publications in refereed journals, cont'd

- 2004 W. Enghardt, **P. Crespo**, F. Fiedler, R. Hinz, K. Parodi, J. Pawelke, F. Pönisch, *Charged hadron tumour therapy monitoring by means of PET*, Nucl. Instr. Meth. A, vol. 525, pp. 284–8
- 2003 M. Kapusta, **P. Crespo**, D. Wolski, M. Moszyński, W. Enghardt, *Hamamatsu S8550 APD arrays for high resolution scintillation readout*, Nucl. Instr. Meth. A, vol. 504, pp. 139–42
- 2002 M. Kapusta, **P. Crespo**, M. Moszyński, W. Enghardt, M. Szawłowski, B. Zhou, D. Wolski, *Evaluation of LAAPD arrays for high resolution scintillator matrices readout*, IEEE Trans. Nucl. Sci., vol. 49, no. 4, pp. 1693–8
- 2001 **P. Crespo**, J. Debus, W. Enghardt, Th. Haberer, O. Jäkel, M. Krämer, G. Kraft, *Tumour therapy with carbon ion beams*, Phys. Medica, vol. XVII, no. 4, pp. 1–3
- 2000 **P. Crespo**, J. van der Marel, V. Chepel, M.I. Lopes, D. Santos, L. Janeiro, V. Solovov, R.F. Marques, A.J.P.L. Policarpo, *Pulse processing for the PET multiwire liquid xenon ionisation chamber*, IEEE Trans. Nucl. Sci., vol. 47, no. 6, pp. 2119–26
- With the AMS collaboration, *Cosmic protons*, Phys. Lett. B, vol. 490, pp. 27–35
- With the AMS collaboration, *Leptons in near earth orbit*, Phys. Lett. B, vol. 484, pp. 10–22
- With the AMS collaboration, *Protons in near earth orbit*, Phys. Lett. B, vol. 472, pp. 215–26
- 1999 V. Chepel, M.I. Lopes, J. van der Marel, **P. Crespo**, D. Santos, L. Janeiro, V. Solovov, R. Ferreira Marques, A.J.P.L. Policarpo, *The liquid xenon detector for PET: recent results*, IEEE Trans. Nucl. Sci., vol. 46, pp. 1038–44
- With the AMS collaboration, *Search for anti-helium in cosmic rays*, Phys. Lett. B, vol. 461, pp. 387–96
- 1998 **P. Crespo**, V. Chepel, M.I. Lopes, L. Janeiro, R. Ferreira Marques, A.J.P.L. Policarpo, *Pulse shape analysis in the liquid xenon multiwire ionisation chamber for PET*, IEEE Trans. Nucl. Sci., vol. 45, no. 3, pp. 561–7

Conference contributions and proceedings

- 2005 F. Fiedler, **P. Crespo**, K. Parodi, M. Sellesk, W. Enghardt, *The feasibility of in-beam PET for therapeutic beams of ^3He* , IEEE 2005 Nucl. Sci. Symp. and Med. Imag. Conf., Puerto Rico, USA, Oct. 2005. Talk and proceedings (accepted)
- 2004 **P. Crespo**, T. Barthel, H. Frais-Kölbl, E. Griesmayer, K. Heidel, K. Parodi, J. Pawelke, W. Enghardt, *Suppression of random coincidences during in-beam PET measurements*, IEEE 2004 Nucl. Sci. Symp., Rome, Italy, Oct. 2004. Talk and proceedings
- 2003 **P. Crespo**, M. Kapusta, J. Pawelke, M. Moszyński, W. Enghardt, *First in-beam PET imaging with LSO/APD-array detectors*, IEEE 2003 Med. Imag. Conf., Portland, OR, USA, Oct. 2003. Poster and proceedings
- M. Kapusta, **P. Crespo**, D. Wolski, K. Heidel, L. Heinrich, J. Hutsch, J. Pawelke, M. Sobiella, A. Trzcinska, M. Moszyński, W. Enghardt, *The LSO/APDA array as a possible detector for in-beam PET in hadron therapy*, IEEE 2003 Nucl. Sci. Symp., Portland, OR, USA, Oct. 2003. Talk
- 2002 M. Kapusta, **P. Crespo**, D. Wolski, M. Moszyński, W. Enghardt, *Hamamatsu S8550 APD arrays for high resolution scintillator matrices readout*, Third Beaune Conf. on New Developments in Photon Detection, Beaune, France, June 2002. Talk
- 2001 M. Kapusta, **P. Crespo**, M. Moszyński, W. Enghardt, M. Szawłowski, B. Zhou, D. Wolski, *Evaluation of LAAPD arrays for high resolution scintillator matrices readout*, IEEE 2001 Nucl. Sci. Symp., San Diego, CAL, USA, Nov. 2001. Talk

- 2000 **P. Crespo**, J. Debus, W. Enghardt, Th. Haberer, O. Jäkel, M. Krämer, G. Kraft, *Tumour therapy with carbon ion beams*, MeRPE: Meeting on Medical Radiation Physics and Engineering, Lisbon, Portugal, Nov. 2000. Talk
- K. Lauckner, **P. Crespo**, W. Enghardt, J. Pawelke, G. Kraft, An LSO-based scanner for in-beam PET: a feasibility study, IEEE 2000 Nucl. Sci. Symp., Lyon, France, Oct. 2000. Poster and proceedings
- 1998 **P. Crespo**, J. van der Marel, V. Chepel, M.I. Lopes, L. Janeiro, V. Solovov, R. Ferreira Marques, A.J.P.L. Policarpo, *Pulse processing for the PET liquid xenon multiwire ionisation chamber*, IEEE 1998 Nucl. Sci. Symp., Toronto, CAN, Nov. 1998. Poster
- V. Chepel, M.I. Lopes, J. van der Marel, **P. Crespo**, L. Janeiro, V. Solovov, R. Ferreira Marques, A.J.P.L. Policarpo, *The liquid xenon chamber for PET: recent results*, IEEE 1998 Nucl. Sci. Symp., Toronto, CAN, Nov. 1998. Poster
- 1997 **P. Crespo**, V. Chepel, M.I. Lopes, L. Janeiro, R. Ferreira Marques, A.J.P.L. Policarpo, *Pulse shape analysis in the liquid xenon multiwire ionisation chamber for PET*, IEEE 1997 Med. Imag. Conf., Orlando, NM, USA, Nov. 1997. Poster

Other communications

- 2004 **P. Crespo**, *In-beam PET for hadrontherapy using LSO/APD-array detectors*, 41th Crystal Clear General Meeting, CERN, Sept. 2004. Invited talk
- P. Crespo**, *Optimization of an in-beam positron emission tomograph for monitoring carbon ion radiotherapy with a rotating beam line*, PhD students seminars, Inst. of Nuclear and Hadron Physics, FZR, Dresden, July 2004. Talk
- P. Crespo**, W. Enghardt, J. Pawelke, *CAGE - a CAMAC based DAQ for radiation physics*, Data Acquisition Meeting at the Inst. of Nuclear and Hadron Physics, FZR, Dresden, July 2004. Talk
- P. Crespo**, M. Kapusta, J. Pawelke, M. Moszyński, W. Enghardt, *First in-beam PET imaging with LSO/APD-array detectors*, Internal evaluation of the Inst. of Nuclear and Hadron Physics, FZR, Dresden, March 2004. Poster
- 2003 **P. Crespo**, W. Enghardt, A. Winter, Th. Haberer, W. Bourgeois, *The combination of a PET scanner with a rotating ion beam delivery*, ENLIGHT Workpackage 5, Inst. of Nuclear and Hadron Physics, FZR, Dresden, Jan. 2003. Talk
- 2002 **P. Crespo**, *Photon detection with avalanche photodiodes*, Inst. of Radiation Protection Physics, Dresden University of Technology, May 2002. Talk
- 2001 **P. Crespo**, *The search for super heavy nuclei: has the top been reached?*, PhD students seminars, GSI Darmstadt, June 2001. Talk
- P. Crespo**, *Tumour therapy with carbon ion beams*, Heavy Ion Laboratory, Warsaw, Mar. 2001. Invited talk
- P. Crespo**, *Latest results and the motivations for the AMS experiment: search for dark matter, anti-matter and cosmic ray composition*, PhD students seminars, GSI Darmstadt, Jan. 2001. Talk
- 2000 **P. Crespo**, *Tumour therapy with carbon ion beams*, Portuguese Research Reactor, Sacavém, Portugal, Dec. 2000. Invited talk
- 1999 **P. Crespo**, *The astrophysics motivations of the AMS experiment and the motivations for a RICH detector: search for dark matter, anti-matter and cosmic ray composition*, Inst. of Nuclear and Hadron Physics, FZR, Dresden, Oct. 1999. Talk
- P. Crespo**, *A liquid xenon multiwire drift chamber for γ -ray detection with 3D information*, Div. of Radiation Physics, Inst. of Nuclear and Hadron Physics, FZR, Dresden, Aug. 1999. Talk
- P. Crespo**, F. Barão, *Cerenkov angle reconstruction algorithm with an aerogel radiator*, AMS RICH detector collaboration, CERN, June 1999. Talk

Annual reports

- 2004 **P. Crespo**, T. Barthel, H. Frais-Kölbl, E. Griesmayer, K. Heidel, K. Parodi, J. Pawelke, W. Enghardt, *Suppression of random coincidences during in-beam PET measurements*, Wiss.-Tech. Ber., FZR-423, pp. 79
- 2003 **P. Crespo**, M. Kapusta, J. Pawelke, M. Moszyński, W. Enghardt, *In-beam PET imaging with LSO/APD-array detectors: first results*, Wiss.-Tech. Ber., FZR-401, pp. 65
- 2002 **P. Crespo**, J. Pawelke, W. Enghardt, *A CAMAC data acquisition system for multi parameter measurements*, Wiss.-Tech. Ber., FZR-372, pp. 82
- P. Crespo**, M. Kapusta, K. Heidel, L. Heinrich, J. Hutsch, J. Pawelke, M. Sobiella, D. Wolski, W. Enghardt, M. Moszyński, *Position sensitive photon detectors of lutetium oxyorthosilicate crystals coupled to avalanche photodiode arrays*, Wiss.-Tech. Ber., FZR-372, pp. 81
- M. Kapusta, **P. Crespo**, M. Moszyński, W. Enghardt, , D. Wolski *Hamamatsu S8550 APD arrays for high resolution scintillator matrices readout*, Wiss.-Tech. Ber., FZR-372, pp. 80
- W. Enghardt, **P. Crespo**, W. Bourgeois, A. Winter, *A technical feasibility study for a PET therapy monitor combined with a rotating ion beam delivery*, Wiss.-Tech. Ber., FZR-372, pp. 83–4
- 2001 **P. Crespo**, M. Kapusta M. Moszyński, W. Enghardt, J. Pawelke, M. Szawlowski, *Evaluation of avalanche photodiode arrays for the readout of high granularity scintillation matrices*, GSI Rep. 2002-1, pp. 170
- P. Crespo**, W. Enghardt, K. Lauckner, *A new fully 3D maximum likelihood PET reconstruction applicable to different detector arrangements*, GSI Rep. 2002-1, pp. 173–4
- 2000 **P. Crespo**, K. Lauckner, W. Enghardt, *The combination of an in-beam PET scanner with a rotating beam delivery for ion tumour therapy*, Wiss.-Tech. Ber., FZR-319, pp. 100–1
- K. Lauckner, **P. Crespo**, W. Enghardt, J. Pawelke, *Feasibility study for an LSO-based in-beam PET scanner*, Wiss.-Tech. Ber., FZR-319, pp. 99
- W. Enghardt, K. Parodi, J. Pawelke, F. Pönisch, M. Sobiella, **P. Crespo**, T. Haberer, C. Kausch, K. Lauckner, D. Schardt, *Positron emission tomography (PET) for ion therapy quality assurance*, GSI Rep. 2001-1, pp. 161

Attended schools and workshops

- 1999 1999 CERN Summer Student School, CERN, Aug. 1999, as volunteer
- 1998 1998 CERN School of Computing, Funchal, Portugal, Sept. 1998
- 1997 CERN Workshop on Field Buses, CERN, Sept. 1997

Languages

Portuguese, English, Italian, Spanish; fluent conversation, reading and writing

French; medium conversation, reading and writing

German; basic conversation and reading

Computer

- Analysis PAW 2.10/09 (Physics Analysis Workstation, CERN)
IDL (Interactive Data Language, CREASO, Gilching, Germany)
- Simulation Geant 3.21 (detector description and simulation tool, CERN)
Electro (electrostatic modeller, Integrated Engineering Software Inc., Canada)
- Acquisition LabWindows/CVI (National Instruments Corp., Austin, TX, USA)
C/C++ code interfaced with Qt (Trolltech AS, Oslo, Norway) and Qplotter (CERN)
- Programming C, C++, Fortran, Pascal, Assembler (Texas Instruments TMS)